Universidad de Concepción
Dirección de Postgrado
Facultad de Ciencias Físicas y Matemáticas
Programa de Doctorado en Ciencias Aplicadas
con Mención en Ingeniería Matemática

MODELOS SHALLOW WATER PARA LA PROPAGACIÓN DE TSUNAMIS, EL IMPACTO SOBRE LA VEGETACIÓN COSTERA Y TRANSPORTE DE SEDIMENTO

SHALLOW WATER MODELS FOR TSUNAMI PROPAGATION, COASTAL VEGETATION IMPACT AND SEDIMENT TRANSPORT

Tesis para optar al grado de Doctor en Ciencias Aplicadas
con mención en Ingeniería Matemática

Jorge Johnny Moya Abuhadba
CONCEPCIÓN-CHILE
2026

Profesor Guía: Dr. Raimund Bürger
CI^{2}MA y Departamento de Ingeniería Matemática
Universidad de Concepción, Chile

Cotutor: Dr. Enrique Domingo Fernandez Nieto
Matemática Aplicada I
Universidad de Sevilla, España

Shallow water models for tsunami propagation, coastal vegetation impact and sediment transport

Jorge Johnny Moya Abuhadba

Directores de Tesis: Raimund Bürger, Universidad de Concepción, Chile.
Enrique Doming Fernandez Nieto, Universidad de Sevilla, España.

Director de Programa: Raimund Bürger, Universidad de Concepción, Chile.

COMISIÓN EVALUADORA

Prof.

Prof.

Prof.

Prof.

COMISIÓN EXAMINADORA

Firma: ____
Prof.

Firma: ____
Prof.

Firma: ____
Prof.

Firma: ____
Prof.

Calificación: ____

Concepción, Enero de 2025

Abstract

This thesis presents the development of advanced finite volume methods for the simulation of complex free-surface geophysical flows governed by shallow-water-type systems. Although the physical problems studied—tsunami propagation through coastal forests and sediment transport with bed evolution—belong to different environmental contexts, they share a common mathematical structure based on depth-averaged balance laws involving non-conservative products. The central objective of this research is to extend the classical Saint-Venant framework to include additional physical processes while preserving the well-balanced and conservative properties required for accurate and stable numerical simulation.

The first part introduces a one-dimensional multilayer, non-hydrostatic model for tsunami propagation and its interaction with coastal vegetation. The formulation incorporates drag, inertia, and porosity effects of tree canopies in a vertically resolved manner, which enhances the representation of forest-induced attenuation. The governing equations are solved using a projection method for non-hydrostatic pressure coupled with polynomial-viscosity-matrix finite volume schemes. The resulting approach preserves the well-balanced property and remains robust under dry–wet transitions.

The second part focuses on morphodynamic processes through a non-hydrostatic Saint-Venant–Exner-type model that couples hydrodynamics with sediment transport, erosion, and deposition. The formulation includes density variations, gravitational effects, and sediment exchange in non-equilibrium between the fluid and bed layers. Novel well-balanced finite volume schemes, the first is a physically motivated correction of the numerical diffusion term for the Rusanov and Harten-Lax-van Leer (HLL), the second one is a new polynomial-viscosity-matrix-based (PVM) scheme, denoted "PVM-2I", that modifies the numerical approximation of the bed evolution equation according to its related characteristic speed. These schemes are developed to capture steady states accurately and prevent spurious erosion in numerical simulations.

The third part extends the multilayer non-hydrostatic framework to two-dimensional tsunami modeling. The model describes vertical exchanges, inter-layer viscosity, and vegetation drag in a fully coupled system. The numerical implementation combines path-conservative finite volume methods with semi-implicit treatments of the gravitational source terms, which improve computational efficiency while maintaining stability.

Together, these contributions provide a unified computational framework for multilayer, multiphase, non-hydrostatic shallow-water systems. The models developed in this work are physically consistent, numerically stable, and computationally efficient, offering new tools for the study of hydrodynamic and morphodynamic processes in coastal and riverine environments, with applications in environmental engineering and natural hazard mitigation.

Resumen

Esta tesis presenta el desarrollo de métodos de volúmenes finitos avanzados para la simulación de flujos geofísicos de superficie libre gobernados por sistemas del tipo aguas someras. Aunque los problemas físicos estudiados —la propagación de tsunamis a través de bosques costeros y el transporte de sedimentos con evolución del lecho— pertenecen a distintos contextos ambientales, ambos comparten una estructura matemática común basada en leyes de balance promediadas en profundidad que incluyen términos no conservativos. El objetivo central de esta investigación es extender el marco clásico de Saint-Venant para incorporar procesos físicos adicionales, manteniendo las propiedades de equilibrio exacto y conservación necesarias para lograr simulaciones numéricas estables y precisas.

La primera parte introduce un modelo unidimensional multicapa y no hidrostático para describir la propagación del tsunami y su interacción con la vegetación costera. La formulación incorpora de manera explícita los efectos de arrastre, inercia y porosidad del dosel arbóreo, mejorando la representación de la atenuación inducida por el bosque. Las ecuaciones gobernantes se resuelven mediante un método de proyección para la presión no hidrostática acoplado con esquemas de volúmenes finitos basados en matrices de viscosidad polinómica, lo que permite preservar el equilibrio hidrostático y mantener la robustez ante transiciones seco-húmedo.

La segunda parte se centra en los procesos morfodinámicos mediante un modelo no hidrostático de tipo Saint-Venant–Exner que acopla la hidrodinámica con el transporte de sedimentos, la erosión y la deposición. La formulación incluye variaciones de densidad, efectos gravitacionales y el intercambio de sedimentos en no equilibrio entre las capas de fluido y fondo. Se proponen nuevos esquemas de volúmenes finitos bien balanceados: el primero consiste en una corrección físicamente motivada del término de difusión numérica para los esquemas de Rusanov y Harten–Lax–van Leer (HLL), el segundo es un nuevo esquema basado en una matriz de viscosidad polinómica (PVM), denominado “PVM-2I”, que modifica la aproximación numérica de la ecuación de evolución del lecho de acuerdo con su velocidad característica asociada. Estos esquemas se desarrollan para captar con precisión los estados estacionarios y evitar erosión espuria en las simulaciones numéricas.

La tercera parte extiende el marco multicapa no hidrostático al caso bidimensional para la modelación de tsunamis. El modelo describe los intercambios verticales, la viscosidad entre capas y las fuerzas de arrastre de la vegetación dentro de un sistema completamente acoplado. La

implementación numérica combina métodos de volúmenes finitos de tipo camino-conservativo con tratamientos semiimplícitos de los términos gravitacionales, lo que mejora la eficiencia computacional sin comprometer la estabilidad.

En conjunto, estos aportes proporcionan un marco computacional unificado para sistemas multicapa, multifase y no hidrostáticos del tipo aguas someras. Los modelos desarrollados son físicamente consistentes, numéricamente estables y computacionalmente eficientes, ofreciendo nuevas herramientas para el estudio de procesos hidrodinámicos y morfodinámicos en ambientes costeros y fluviales, con aplicaciones en ingeniería ambiental y mitigación de desastres naturales.

Agradecimientos

Proyectos de investigación y apoyo institucional

Esta tesis ha sido desarrollada en el marco y con el apoyo financiero de las siguientes instituciones y proyectos de investigación:

- Agencia Nacional de Investigación y Desarrollo (ANID, Chile) a través de los proyectos **Fondecyt 1210610**, **Fondecyt 1250676** y **Anillo ANID/ACT210030**.
- Centro de Modelamiento Matemático (CMM), proyecto BASAL **FB210005**.
- Centro de Recursos Hídricos para la Agricultura y la Minería (CRHIAM), proyectos **ANID/FONDAP/15130015** y **ANID/FONDAP/1523A0001**.
- Junta de Andalucía, a través del proyecto de I+D+i PAIDI 2021 **ProyExcel 00525**.
- Beca de Doctorado Nacional **ANID-PCHA/Doctorado Nacional/2021-21211457**.

Estoy sinceramente agradecido por el apoyo recibido de todas las instituciones, proyectos y personas que han contribuido a la realización de esta tesis.

Jorge Johnny Moya Abuhadba

Expreso mi profundo agradecimiento a mis supervisores, el **Profesor Raimund Bürger** (Universidad de Concepción) y el **Profesor Enrique D. Fernández-Nieto** (Universidad de Sevilla), por su guía, apoyo y generosidad académica durante el desarrollo de esta tesis. Su rigor científico, entusiasmo y dedicación han sido una fuente constante de inspiración y aprendizaje.

A Raimund, por su claridad, paciencia y capacidad para transmitir el valor del trabajo metódico y preciso. A Enrique, por su visión matemática, su energía y su permanente disposición a impulsar cada avance de este trabajo.

Agradezco también a mis coautores y colegas, en especial a **José Garres-Díaz**, por las fructíferas colaboraciones y el trabajo conjunto que dieron forma a los artículos que constituyen esta tesis. A mis compañeros del **CI^{2}MA** (Centro de Investigación en Ingeniería Matemática de la Universidad de Concepción), **Juan Paulo Ortega** y **Romel Pineda**, y también a mis compañeros del **Departamento de Matemática Aplicada I** de la Universidad de Sevilla, **Gwendal Ewen Benoit Maxime Leger** y **Julie Binard**, por su apoyo, las estimulantes discusiones y el ambiente de colaboración que hicieron más grato este camino.

Finalmente, a mi familia, por su amor, paciencia y apoyo incondicional a lo largo de todo este proceso. Esta tesis es también resultado de su confianza y aliento constante.

Jorge Johnny Moya Abuhadba

Contents

List of Tables

List of Figures

Introduction

Motivation

Water-related natural processes such as floods, tsunamis, and sediment transport play a crucial role in shaping coastal and riverine environments. Understanding and predicting their behavior is essential not only for environmental protection and engineering design but also for disaster prevention and sustainable management of natural resources. Mathematical and numerical modeling of these processes has therefore become an indispensable tool in environmental hydraulics and geophysical fluid dynamics.

Among the most versatile frameworks for representing free-surface flows are the *shallow-water equations*, also known as the *Saint-Venant system*. These equations describe the evolution of vertically averaged quantities such as water depth and discharge, and are applicable to a wide variety of geophysical contexts. However, classical shallow water models are limited in their ability to represent vertical structure, dispersive effects, and morphodynamic coupling with sediment transport.

The motivation of this Ph.D. thesis is to contribute to the development of reliable and physically consistent numerical methods for extended shallow-water-type systems, incorporating additional physical processes such as non-hydrostatic pressure and bed evolution. Although the specific applications studied, tsunami forest interaction and sediment transport address different environmental problems, they share a common mathematical foundation based on depth-averaged balance laws discretized by well-balanced finite volume schemes. Together, these contributions form part of a broader effort to construct unified computational tools for simulating complex hydro-morphodynamic phenomena in natural environments.

Additionally, field observations of rivers such as the Biobío in Chile reveal the presence of small dune-like bedforms, which resemble miniature waves migrating along the riverbed (Figure 1). These features highlight the importance of understanding sediment transport and morphodynamic feedbacks even at relatively small scales, as they can influence local flow patterns, sediment sorting, and the overall evolution of the riverbed. Incorporating such phenomena into numerical models provides a further motivation for developing advanced shallow-water-type frameworks capable of capturing complex interactions between flow and sediment.

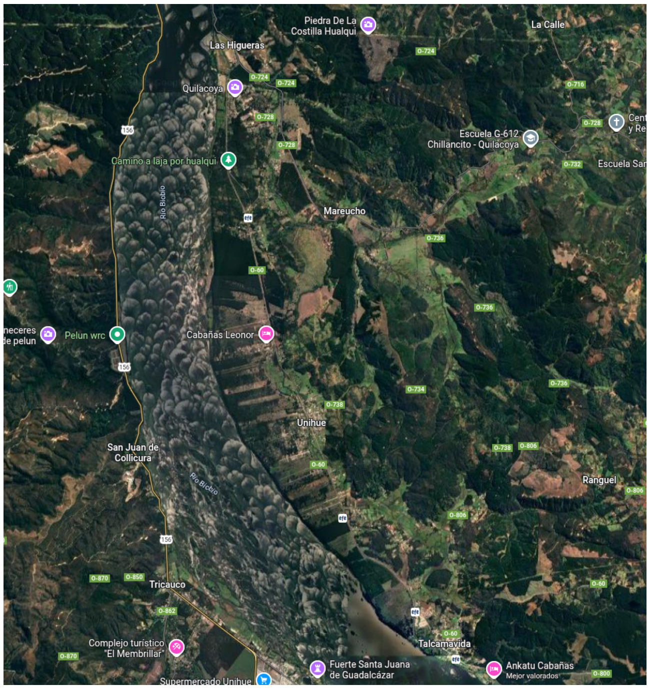

Figure 1: Small bedforms resembling dunes in the Biobío River, Chile, which appear as miniature waves migrating along the riverbed. These structures highlight the importance of morphodynamics and sediment transport even at small scales.

Related Work

The mathematical modeling of free-surface geophysical flows has been extensively studied over the past decades. The *Saint-Venant equations*, first derived in the 19th century, remain a cornerstone of hydraulic modeling, and numerous extensions have been developed to incorporate additional physical processes.

Non-hydrostatic and multilayer models. Classical shallow-water equations rely on the hydrostatic pressure assumption, which restricts their capability to represent dispersive and vertical flow effects. To address these limitations, various non-hydrostatic formulations have been proposed, including depth-averaged and multilayer approaches [4, 5, 8, 9, 34, 67]. These formulations have been successfully applied to tsunami propagation, wave breaking, and interactions between waves, coastal structures, and vegetation [46, 60, 69, 70, 77]. Recently, further advances have been proposed to improve the modeling of vegetation-induced drag under non-hydrostatic and rapidly varying flow conditions. In particular, Ginting et al. (2025) [42] introduced a novel drag force formulation for dam-break flows through emergent vegetation, explicitly accounting for non-uniform pressure distributions, free-surface variations, and non-hydrostatic effects.

Multilayer models reproduce the vertical flow structure while maintaining a moderate computational cost compared to fully three-dimensional Navier–Stokes simulations, thus achieving an effective balance between efficiency and physical accuracy. Beyond these classical multilayer approaches based on piecewise constant vertical profiles, alternative strategies have been proposed to improve the representation of vertical flow structures. In particular, Garres-Díaz et al. (2023) [41] introduced a unified framework that generalizes both multilayer and moment models, allowing layerwise polynomial velocity representations. Their analysis highlights the respective advantages and limitations of multilayer and moment approaches in terms of accuracy and computational efficiency.

Morphodynamic and sediment transport models. Coupled hydro-morphodynamic systems are used to describe sediment erosion, transport, and deposition in riverine and coastal environments. The *Saint-Venant–Exner system* [15, 16, 33] captures the dynamic interaction between flow hydrodynamics and bed evolution. One of the main numerical challenges lies in preserving steady states and global mass conservation, particularly in the presence of non-conservative products and density variations. Recent developments in finite volume and path-conservative frameworks [22, 28, 45, 57, 73] have provided robust strategies that guarantee well-balanced behavior and positivity preservation in morphodynamic simulations.

Finite volume methods and well-balanced schemes. Finite volume methods provide a natural discretization technique for hyperbolic systems of conservation laws because they preserve local conservation at the discrete level. The construction of well-balanced schemes capable of maintaining steady states and treating wet–dry interfaces in a stable manner has become a central topic in modern computational hydraulics [6]. In this thesis, the *polynomial viscosity matrix (PVM)* methodology [28] is adopted and further developed to offer a consistent and flexible numerical framework for shallow-water-type systems with non-conservative products.

Organization of this thesis

This dissertation is organized into three main research contributions, each corresponding to a journal article or conference proceeding, followed by a final chapter that summarizes the main findings and future perspectives. Although the physical applications differ, all chapters share a common methodological foundation based on finite volume methods for shallow-water-type systems with non-conservative products.

- **Chapter 1.** We present a *multilayer non-hydrostatic model* for the simulation of tsunami–forest interaction. The model incorporates vegetation effects through drag, porosity, and inertia terms within a multilayer depth-averaged framework, enabling a vertically resolved description of flow–vegetation interactions. The proposed finite volume scheme employs a projection method for the non-hydrostatic pressure and preserves well-balancedness and robustness under wet–dry conditions. The contents of this chapter are based on the article *“A multilayer non-hydrostatic shallow-water model for tsunami–forest interaction”*, by J. Moya, E. Fernández-Nieto, and R. Bürger, submitted to the *ESAIM: Mathematical Modelling and Numerical Analysis* (2025) [14], and accepted for publication in the proceedings of *The 19th International Conference on "Hyperbolic Problems: Theory, Numerics and Applications" (HYP2024), Shanghai, July 1-5, 2024* under the title of *"Non-hydrostatic multilayer modeling of tsunami–vegetation interaction"*.

- **Chapter 2.** This chapter introduces a *non-hydrostatic Saint-Venant–Exner-type model* for sediment transport and morphodynamic processes. The model couples hydrodynamics, sediment concentration, and bed evolution, incorporating density variations and gravitational effects. Novel well-balanced finite volume schemes based on the *Polynomial Viscosity Matrix* formulation are developed to guarantee numerical stability and the preservation of equilibrium states. The material presented here corresponds to the article *"Well-balanced physics-based finite volume schemes for Saint-Venant–Exner-type models of sediment transport"*, by J. Moya, E. Fernández-Nieto, R. Bürger and José Garres-Diaz, published in *Advances in Water Resources* (2025) [17].

- **Chapter 3.** The third chapter extends the tsunami–forest interaction model to two horizontal dimensions, incorporating full 2D dynamics and improved representations of vertical and lateral flow–vegetation interactions. The model employs a multidimensional path-conservative finite volume discretization combined with non-hydrostatic projection and PVM stabilization. This chapter corresponds to the paper *"A two-dimensional multilayer non-hydrostatic model for tsunami–forest interaction"*, by J. Moya, E. Fernández-Nieto, and R. Bürger, currently *in preparation* (2025).

- **Chapter 4.** The final chapter provides the general conclusions and outlines possible directions for future research, including the development of a unified computational framework for multi-layer, multi-phase, and morphodynamic shallow-water systems.

Introducción

Motivación

Los procesos naturales relacionados con el agua, como inundaciones, tsunamis y transporte de sedimentos, desempeñan un papel crucial en la configuración de los ambientes costeros y fluviales. Comprender y predecir su comportamiento es esencial no solo para la protección ambiental y el diseño de ingeniería, sino también para la prevención de desastres y la gestión sostenible de los recursos naturales. Por ello, la modelización matemática y numérica de estos procesos se ha convertido en una herramienta indispensable en hidráulica ambiental y dinámica de fluidos geofísicos.

Entre los marcos más versátiles para representar flujos de superficie libre se encuentran las *ecuaciones de aguas poco profundas*, también conocidas como el *sistema de Saint-Venant*. Estas ecuaciones describen la evolución de cantidades promediadas verticalmente, como la profundidad del agua y el caudal, y son aplicables a una amplia variedad de contextos geofísicos. Sin embargo, los modelos clásicos de aguas poco profundas están limitados en su capacidad para representar la estructura vertical, los efectos dispersivos y el acoplamiento morfodinámico con el transporte de sedimentos.

La motivación de esta tesis doctoral es contribuir al desarrollo de métodos numéricos fiables y físicamente consistentes para sistemas extendidos tipo aguas poco profundas, incorporando procesos físicos adicionales, como la presión no hidrostática y la evolución del lecho. Aunque las aplicaciones específicas estudiadas interacción tsunami-bosque y transporte de sedimentos abordan diferentes problemas ambientales, comparten una base matemática común basada en leyes de conservación promediadas en profundidad, discretizadas mediante esquemas de volumen finito bien balanceados. En conjunto, estas contribuciones forman parte de un esfuerzo más amplio por construir herramientas computacionales unificadas para simular fenómenos hidro-morfodinámicos complejos en entornos naturales.

Además, observaciones de campo en ríos como el Biobío en Chile muestran la presencia de pequeñas formas de lecho similares a dunas, que se asemejan a ondas en miniatura migrando a lo largo del lecho del río (Figura 1). Estas características destacan la importancia de comprender el transporte de sedimentos y la retroalimentación morfodinámica incluso a escalas relativamente pequeñas, ya que pueden influir en los patrones locales de flujo, la selección de sedimentos y la evolución general del lecho del río. Incorporar estos fenómenos en los modelos numéricos proporciona una motivación adicional para desarrollar marcos avanzados tipo aguas poco profundas capaces de capturar interacciones complejas entre flujo y sedimentos.

Trabajo Relacionado

El modelado matemático de los flujos geofísicos con superficie libre ha sido ampliamente estudiado durante las últimas décadas. Las *ecuaciones de Saint-Venant*, derivadas por primera vez en el siglo XIX, continúan siendo un pilar fundamental en la modelación hidráulica, y numerosas extensiones se han desarrollado para incorporar procesos físicos adicionales.

Modelos no hidrostáticos y multicapa. Las ecuaciones clásicas de aguas someras se basan en la hipótesis de presión hidrostática, lo que limita su capacidad para representar efectos dispersivos y verticales. Para superar estas limitaciones, se han propuesto diversas formulaciones no hidrostáticas, entre ellas aproximaciones promediadas en profundidad y modelos multicapa [4, 5, 8, 9, 34, 67]. Estos modelos se han aplicado con éxito al estudio de la propagación de tsunamis, la rotura de olas y la interacción entre las ondas, las estructuras costeras y la vegetación [46, 60, 69, 70, 77].Recientemente, se han propuesto nuevos avances orientados a mejorar la modelización de la fuerza de arrastre inducida por la vegetación en condiciones no hidrostáticas y de flujos rápidamente variables. En particular, Ginting et al. (2025) [42] introdujeron una formulación novedosa de la fuerza de arrastre para flujos tipo dam-break a través de vegetación emergente, que tiene en cuenta explícitamente distribuciones de presión no uniformes, variaciones de la superficie libre y efectos no hidrostáticos.

Los modelos multicapa permiten reproducir la estructura vertical del flujo manteniendo un coste computacional moderado en comparación con simulaciones completamente tridimensionales de Navier–Stokes, logrando así un equilibrio efectivo entre eficiencia numérica y fidelidad física. Más allá de estos enfoques multicapa clásicos basados en perfiles verticales constantes por capas, se han propuesto estrategias alternativas para mejorar la representación de las estructuras verticales del flujo. En particular, Garres-Díaz et al. (2023) [41] presentaron un marco unificado que generaliza tanto los modelos multicapa como los modelos de momentos, permitiendo representaciones polinómicas de la velocidad a nivel de capa. Su análisis pone de manifiesto las ventajas y limitaciones relativas de los enfoques multicapa y de momentos en términos de precisión y eficiencia computacional.

Modelos morfodinámicos y de transporte de sedimentos. Los sistemas hidrodinámico –morfodinámicos acoplados se utilizan para describir la erosión, el transporte y la deposición de sedimentos en ambientes fluviales y costeros. El sistema *Saint-Venant–Exner* [15, 16, 33] describe la interacción dinámica entre la hidrodinámica del flujo y la evolución del lecho. Uno de los principales desafíos numéricos consiste en preservar los estados de equilibrio y la conservación de masa global, especialmente en presencia de términos no conservativos y variaciones de densidad. Los avances recientes en métodos de volúmenes finitos y formulaciones de tipo camino conservativo [22, 28, 45, 57, 73] han permitido desarrollar estrategias robustas que garantizan un comportamiento bien balanceado y la preservación de la positividad en simulaciones morfodinámicas.

Métodos de volúmenes finitos y esquemas bien balanceados. Los métodos de volúmenes finitos constituyen una técnica natural de discretización para sistemas hiperbólicos de leyes de conservación, ya que preservan localmente la conservación de las magnitudes físicas. El diseño de esquemas bien balanceados capaces de mantener soluciones en equilibrio y tratar interfaces seco–húmedo de manera estable se ha convertido en un tema central en la hidráulica computacional moderna [6]. En esta tesis se adopta y amplía la metodología de la *matriz de viscosidad polinómica (PVM)* [28], con el fin de proporcionar un marco numérico coherente y flexible para sistemas tipo aguas someras con productos no conservativos.

Organización de la tesis

Esta tesis se organiza en tres contribuciones principales de investigación, cada una correspondiente a un artículo científico o contribución en congreso, seguidas de un capítulo final con las conclusiones generales y las perspectivas futuras. Aunque las aplicaciones físicas difieren, todos los capítulos comparten una base metodológica común basada en métodos de volúmenes finitos aplicados a sistemas tipo aguas someras con términos no conservativos.

- **Capítulo 1.** Se presenta un *modelo multilayer no hidrostático* para la simulación de la interacción entre tsunamis y bosques costeros. El modelo incorpora los efectos de la vegetación mediante términos de arrastre, porosidad e inercia dentro de un marco multicapa promediado en profundidad, lo que permite una descripción verticalmente resuelta de las interacciones flujo–vegetación. El esquema numérico propuesto, basado en volúmenes finitos, utiliza un método de proyección para la presión no hidrostática y mantiene las propiedades de equilibrio (well-balanced) y robustez en condiciones de zonas secas y húmedas. El contenido de este capítulo se basa en el artículo *"A multilayer non-hydrostatic shallow-water model for tsunami–forest interaction"*, de J. Moya, E. Fernández-Nieto y R. Bürger, enviado a la revista *ESAIM: Mathematical Modelling and Numerical Analysis* (2025) [14], y aceptado para ser publicado en las actas de la conferencia *19th International Conference on "Hyperbolic Problems: Theory, Numerics and Applications" (HYP2024), Shanghai, July 1-5, 2024*, bajo el título de *"Non-hydrostatic multilayer modeling of tsunami–vegetation interaction"*.
- **Capítulo 2.** Este capítulo introduce un *modelo no hidrostático del tipo Saint-Venant-Exner* para el transporte de sedimentos y los procesos morfodinámicos. El modelo acopla la hidrodinámica, la concentración de sedimentos y la evolución del lecho, incorporando variaciones de densidad y efectos gravitacionales. Se desarrollan nuevos esquemas de

volúmenes finitos balanceados basados en la formulación de la *Matriz de Viscosidad Polinómica (PVM)* para garantizar la estabilidad numérica y la preservación de los estados de equilibrio. El material presentado en este capítulo corresponde al artículo *"Well-balanced physics-based finite volume schemes for Saint-Venant–Exner-type models of sediment transport"*, de J. Moya, E. Fernández-Nieto, R. Bürger y J. Garres-Díaz, publicado en *Advances in Water Resources* (2025) [17].

- **Capítulo 3.** El tercer capítulo extiende el modelo de interacción tsunami–bosque en dos dimensiones horizontales, incorporando la dinámica completamente bidimensional y una representación mejorada de las interacciones verticales y laterales entre el flujo y la vegetación. El modelo utiliza una discretización multidimensional de volúmenes finitos conservativa por trayectorias (*path-conservative*) combinada con un método de proyección no hidrostático y estabilización mediante la PVM. El contenido de este capítulo corresponde al artículo *"A two-dimensional multilayer non-hydrostatic model for tsunami–forest interaction"*, de J. Moya, E. Fernández-Nieto y R. Bürger, actualmente *en preparación* (2025).

- **Capítulo 4.** El capítulo final presenta las conclusiones generales y plantea posibles líneas de trabajo futuro, incluyendo el desarrollo de un marco computacional unificado para modelos de tipo aguas someras multilayer, multifásicos y morfodinámicos.

CHAPTER 1

A multilayer non-hydrostatic model for tsunami-forest interaction

1.1 Introduction

1.1.1 Scope

A number of geophysical applications such as shallow water flows, free surface flows, gravity currents, sediment transport and avalanches give rise to a system of first-order partial differential equations (PDEs) in the vectorial form

$$\partial_t \boldsymbol{W} + \partial_x \boldsymbol{F}(\boldsymbol{W}) + \boldsymbol{B}(\boldsymbol{W})\partial_x \boldsymbol{W} = \boldsymbol{S}(\boldsymbol{W})\sigma'(x), \tag{1.1}$$

where t is time, x is the spatial coordinate, and the sought quantity is a vector $\boldsymbol{W} = \boldsymbol{W}(x,t)$ of state variables, where $\boldsymbol{W}$ belongs to an open convex subset $D \subseteq \mathbb{R}^{\mathcal{N}}$. The vector functions $\boldsymbol{F} : D \to \mathbb{R}^{\mathcal{N}}$ and $\boldsymbol{S} : D \to \mathbb{R}^{\mathcal{N}}$ as well as the matrix function $\boldsymbol{B} : D \to \mathbb{R}^{\mathcal{N}\times\mathcal{N}}$ and the real scalar function $\sigma = \sigma(x)$ are given. Solutions of equations of this type are in general discontinuous, and the well-known salient property of the system (1.1) that complicates its analytical and numerical treatment is the presence of nonconservative products such as $\boldsymbol{B}(\boldsymbol{W})\partial_x \boldsymbol{W}$ [20, 52].

It is the purpose of this contribution to study a specific model of the form (1.1) that arises as a multilayer shallow water system based on a free-surface formulation of the Euler equations for an ideal fluid. The novelty consists in the formulation of this model and its application to forest hydrodynamics as well as its numerical solution by a projection method.

Specifically, the Euler equations are approximated by a layer-averaged non-hydrostatic approach (LDNH) involving linear pressures, piecewise constant horizontal velocities and piecewise linear vertical velocities. Furthermore, specific ingredients such as drag forces, inertia forces, and porosity are adopted from the literature of ocean engineering, landscape ecology and related fields [46, 60, 69, 70, 77] and are incorporated to form a new model of the interaction of a tsunami wave with a coastal forest. In fact, such models and numerical methods are of vital importance for exploring the potential of coastal vegetation as a means of mitigation. A particular feature of the present approach is the description of tree-specific ingredients in a layer-wise manner. Thus, the vertical features of the forest are described with higher accuracy than within a single-layer approach. The second novel contribution, besides the formulation of the multilayer model, is the formulation of a method for its numerical solution inspired by Chorin's classical algorithm for the compressible two-dimensional (2D) Navier-Stokes equations [24, 25, 26]. In the latter context that algorithm is based on a Helmholtz decomposition of the sought velocity field and proceeds, in each time step, by first updating the velocity field (by using the momentum equation without the pressure term) to give an intermediate velocity, and then by computing the finally updated velocity field by a projection onto the space of divergence-free vector fields. The second step involves the solution of an elliptic problem for the sought pressure. This well-known procedure is followed for the present model, although the formulation of the governing equations is more involved due to the Saint-Venant single-layer or multilayer approach and the presence of forces.

Projection methods for the non-hydrostatic pressure in conjunction with polynomial viscosity matrix finite volume methods [28] are employed for the numerical solution of the multilayer model, that is for the propagation of tsunamis and coastal flooding. Experimental observations and field data are used to validate the model.

1.1.2 Related work

Finite volume (FV) schemes are a standard method for solving hyperbolic systems of partial differential equations (PDEs). However, hyperbolic systems arising from balance equations in geophysical applications usually involve nonconservative products that complicate the application of traditional FV schemes. The standard example are shallow water equations with variable bottom topography. A well-known class of FV schemes that can handle nonconservative products are the so-called path-conservative schemes [22, 57, 73]. These schemes are designed specifically for nonconservative systems and are based on the concept of path integration. Path-conservative schemes have been applied to a variety of hyperbolic systems with nonconservative products, including two-layer and layer-averaged shallow water equations, compressible gas dynamics and magnetohydrodynamics. In [55] a generalization of the Roe method [61] was proposed (see also [73]). Nevertheless, its implementation requires explicit knowledge of the eigenstructure of the intermediate matrices. In [28] a specific family of path-conservative schemes is proposed, named polynomial viscosity matrix methods (PVM methods) that generalized several incomplete Riemann solvers such as Rusanov, Lax-Friedrichs or HLL, among others.

Multilayer models are designed to avoid solving a fully three-dimensional model (such as the Navier-Stokes equations for an incompressible fluid). They are based on the so-called shallow water or Saint-Venant approach, that is, a vertically integrated version of the underlying model [4, 5, 7, 8, 9, 15, 16, 33, 34, 62], in our case the Euler equations for an ideal fluid. The multilayer approach consists in subdividing the computational domain into N layers in the vertical direction, which leads to a system of Saint-Venant equations. The unknowns in the present case are horizontal velocities by layer, the total height of the fluid column, and pressure.

The present approach is based on the LDNH_0 model with non-hydrostatic pressure. this approach as an improvement compared with standard shallow-water-based models since the latter usually only cover hydrostatic pressures and neglect vertical acceleration (and therefore dispersive) effects. On the other hand, dispersive models like Boussinesq introduce high-order derivatives for the unknowns, while the LDNH_0 model incorporates these dispersive effects into the non-hydrostatic pressure terms [36, 67].

From the applicative point of view, the general significance of tsumami disaster mitigation by the natural method of coastal forest plantation is discussed in the overview article by Tanaka [69] (for instance). The present work is based on detailed technical information provided in [46, 60, 63, 70, 77].

1.1.3 Outline of the chapter

The remainder of the chapter is organized as follows. In Section 1.2.1 we introduce preliminaries, starting with the basic method for the discretization of (1.1). In Sections 1.2.2 and 1.2.3 we study properties the numerical methods need to have in order to be well balanced and behave correctly in dry front situations. To put the LDNH_0 approach into the proper perspective we first formulate, in Section 1.2.4, a hydrostatic reconstruction of a two-equation shallow water model with a source term, and then, based on these results, we proceed in Section 1.2.5 to formulate the linearized discontinuous non-hydrostatic model (LDNH_0 model) whose unknowns are the height of the water level, the horizontal and the vertical velocity, and pressure as functions of position x and time t. The first three of these quantities are specified by a first-order system of balance laws that in each time step can be handled by the same discretization as the shallow water equations along with hydrostatic reconstruction. The non-hydrostatic pressure, in turn, is updated via a projection step that will eventually lead to the final update of all sought variables. (This procedure is reminiscent of Chorin's method for the 2D incompressible Navier-Stokes equations, as mentioned in Section 1.1.1.) Finally, we specify in Section 1.2.6 the inertia and drag forces related to the coastal forest along with the corresponding concept of porosity. The result is the non-hydrostatic LDNH_0 model, specified for forest forces, in final form. Section 1.3 is devoted to the development of the discretization of the LDNH_0 model. To this end we formulate first, in Section 1.3.1, a preliminary discretization of the first step of Section 1.2.5 that excludes the non-hydrostatic pressure terms which are handled by the projection method. This preliminary discretization is based on plausible arguments but turned out to be unstable due to the nature of the inertia force. An alternative, slightly different but stable discretization is advanced in Section 1.3.2. The numerical method relies on knowledge of the eigenvalues of a matrix related to the Jacobian matrix of the system. These eigenvalues are obtained in Section 1.3.3. Finally, in Section 1.3.4 the scheme that discretizes the elliptic problem for the pressure update is formulated. The treatment of Section 1.3 corresponds to the fully discrete version of the projection method akin to Chorin's method and refers to the single-layer LDNH_0 model. The multilayer version of that model and its discretization are described in in Section 1.4, starting with the definition of multiple layers (Section 1.4.1). We then present (in Section 1.4.2) the LDNH_0 multilayer model (without forces and porosity) arising from layer-wise vertical integration. After discussing layer-wise porosity (in Section 1.4.3) we derive in Section 1.4.4 explicit expressions of the interlayer transfer terms. We then formulate ingredients of the multilayer model that are specific to the application to a forest, namely drag and inertia forces, friction, and viscosity (Sections 1.4.5 and 1.4.6). The resulting multilayer model is summarized in Section 1.4.7. Next, we outline the discretization of the multilayer model. Roughly speaking, the discretization of the first-order system, described in Section 1.4.8, is a multilayer version of the discretization of Section 1.3.2 for the single-layer case (in both cases, non-hydrostatic pressure is disregarded). The remaining ingredients of the multilayer scheme, namely the projection matrix describing the solution of the elliptic problem for the pressure update and finally, the interlayer viscosity effect, are described in Sections 1.4.9 and 1.4.10, respectively. Section 1.5 is devoted to the presentation of numerical examples. To test the accuracy of the scheme we consider in Example 1.1 (Section 1.5.1) the exact soliton solution of the LDNH_0 soliton (described in Appendix A). Examples 1.2 to 1.6 are motivated by selected experiments conducted by Iimura and Tanaka [46]. They are solved in Section 1.5.2 by the single-layer LDNH_0 test model. Examples 1.7 and 1.8 are related test cases but with limited tree height, and Examples 1.9 to 1.13 consider trees with properties that gradually vary with height. These cases are solved by the multilayer LDNH_0 model in Sections 1.5.3 and 1.5.4.

1.2 Preliminaries

1.2.1 Basic method

Let us consider a uniform mesh of cells $I_i = [x_{i-1/2}, x_{i+1/2}]$, where $x_i = i\Delta x$, $i \in \mathbb{Z}$, and time steps $t_\nu = \nu \Delta t$, $\nu \in \mathbb{N}_0$. Then a first-order finite volume discretization of (1.1) can be written as

$$\boldsymbol{W}_i^{\nu+1} = \boldsymbol{W}_i^{\nu} - \frac{\Delta t}{\Delta x}\bigl(\boldsymbol{D}_{i-1/2}^{\nu,+} + \boldsymbol{D}_{i+1/2}^{\nu,-}\bigr), \quad i \in \mathbb{Z}, \quad \nu \in \mathbb{N}_0 \tag{2.1}$$

(see [28] for details), where we define the numerical flux vectors

$$\begin{aligned}\boldsymbol{D}_{i+1/2}^{\nu,\pm} \coloneqq \frac{1}{2}\Bigl(&\boldsymbol{F}(\boldsymbol{W}_{i+1}^{\nu}) - \boldsymbol{F}(\boldsymbol{W}_i^{\nu}) + \boldsymbol{\mathcal{B}}_{i+1/2}^{\nu}(\boldsymbol{W}_{i+1}^{\nu} - \boldsymbol{W}_i^{\nu}) - (\sigma_{i+1} - \sigma_i)\boldsymbol{\mathcal{S}}_{i+1/2}^{\nu} \\ &\pm \boldsymbol{Q}_{i+1/2}^{\nu}\bigl(\boldsymbol{W}_{i+1}^{\nu} - \boldsymbol{W}_i^{\nu} - (\sigma_{i+1} - \sigma_i)(\boldsymbol{\mathcal{A}}_{i+1/2}^{\nu})^{-1}\boldsymbol{\mathcal{S}}_{i+1/2}^{\nu}\bigr)\Bigr),\end{aligned} \tag{2.2}$$

where $\boldsymbol{Q}_{i+1/2}^{\nu}$ is a numerical viscosity matrix, $\boldsymbol{\mathcal{B}}_{i+1/2}^{\nu}$ and $\boldsymbol{\mathcal{A}}_{i+1/2}^{\nu}$ are intermediate matrices, and $\boldsymbol{\mathcal{S}}_{i+1/2}^{\nu}$ is the intermediate vector, corresponding to the states $\boldsymbol{W}_{i+1/2}^{\nu,-}$ and $\boldsymbol{W}_{i+1/2}^{\nu,+}$ of $\boldsymbol{B}$, $\boldsymbol{A}$, and $\boldsymbol{S}$, respectively. The Jacobian matrix of the system (1.1),

$$\boldsymbol{A} := \frac{\partial \boldsymbol{F}(\boldsymbol{W})}{\partial \boldsymbol{W}} + \boldsymbol{B}(\boldsymbol{W}),$$

encodes the linear relationship between the derivative terms and the unknowns in the system. Notice that the scheme (2.1) is not conservative. A standard choice of the viscosity matrix is the one that corresponds to the HLL flux [28] given by

$$\boldsymbol{Q}(\boldsymbol{A}) = \alpha_0 \boldsymbol{I} + \alpha_1 \boldsymbol{A} \quad \text{with} \quad \alpha_0 := \frac{S_{\mathrm{R}}|S_{\mathrm{L}}| - S_{\mathrm{L}}|S_{\mathrm{R}}|}{S_{\mathrm{R}} - S_{\mathrm{L}}}, \quad \alpha_1 := \frac{|S_{\mathrm{R}}| - |S_{\mathrm{L}}|}{S_{\mathrm{R}} - S_{\mathrm{L}}},$$

where $\boldsymbol{I}$ is the $\mathcal{N} \times \mathcal{N}$ identity matrix. If we assume that the eigenvalues $\lambda_{1,i+1/2}, \dots, \lambda_{\mathcal{N},i+1/2}$ of $\boldsymbol{A}$ are real, then a possible choice for S_{L} and S_{R} is

$$S_{\mathrm{L}} = \min\{\lambda_{1,i+1/2}, \dots, \lambda_{\mathcal{N},i+1/2}\}, \quad S_{\mathrm{R}} = \max\{\lambda_{1,i+1/2}, \dots, \lambda_{\mathcal{N},i+1/2}\}.$$

In general S_{R} and S_{L} represent upper and lower bounds of the region in which the eigenvalues of the system are located.

1.2.2 Dry/wet fronts

The term “dry/wet front” (DWF) is frequently used to address the interface between a region with fluid and a region without fluid. In the case of a tsunami simulation, the DWF describes the interface between the advancing tsunami wave and the dry land. As the wave approaches the coastline, the DWF moves inland, with the speed and behavior of the front affected by a variety of factors, such as the topography and bathymetry of the coastline, and the magnitude and duration of the wave. Accurately modeling the behavior of the DWF is evidently important for predicting the behavior of waves in coastal areas, and for assessing the risk and impact of tsunami events. A correct implementation of this front is crucial to preserve the well-balancing properties of the numerical method, this is, the method should preserve the equilibrium state of the fluid flow, where the water level is constant and the velocity is zero, in the presence of non-uniform bottom topography or other sources of external forces, which is critical for predicting the behavior of waves in coastal areas. In particular, well-balanced methods ensure that the numerical solution accurately captures the location of the DWF and the speed of its movement. Numerical methods that are not well-balanced can produce spurious oscillations or artificial numerical diffusion at the DWF, which can lead to inaccurate simulation results. Such methods can also violate the conservation laws leading to nonphysical solutions.

1.2.3 Well-balanced property

Consider a simple shallow-water system of equations

$$\begin{aligned} \partial_t h + \partial_x q_u &= 0, \\ \partial_t q_u + \partial_x \left(\frac{q_u^2}{h} + \frac{1}{2} g h^2 \right) &= -g h z_{\mathrm{b}}'(x), \end{aligned} \tag{2.3}$$

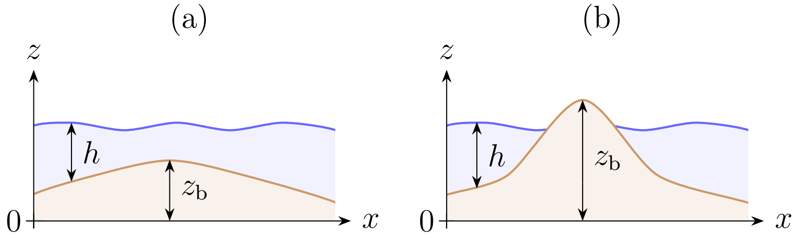

Figure 1.1: Schematic (a) of the physical system, (b) of the physical system with dry fronts.

where h is the water depth, u is the water velocity, $q_u := hu$ and $z_\mathrm{b} = z_\mathrm{b}(x)$ is the channel bottom with $x \in [0, L]$ and $t \in [0, T]$, see Figure 1.1 (a). To derive this model, and in general any other Boussinesq system, from the Navier-Stokes equations it is assumed that $h > 0$. However, this assumption does not allow us, for example, to simulate waves reaching a coast. One needs to extend this model to handle physically correctly situations when $h = 0$. To this end, the definition

$$\eta(x, t) := h(x, t) + z_\mathrm{b}(x)$$

is very useful since in a steady state, η should be a constant. In fact, for $q_u = 0$ the shallow water system (2.3) reduces to

$$\partial_t h = 0, \quad gh\partial_x h = -ghz_\mathrm{b}' \quad \Rightarrow \quad h = h(x), \quad \partial_x(h + z_\mathrm{b}) = 0.$$

To achieve that the numerical scheme does not introduce non-physical oscillations, Audusse et al. [6] introduced the following well-balanced condition called “conservation property” or “C-property”:

Definition 1.2.1 (C-property)**.** *A numerical scheme is said to* possess the C-property *if it exactly reproduces the steady-state solutions* $q_u \equiv 0$*,* $h \equiv \eta - z_\mathrm{b}$*, where* η *is a constant such that* $\eta > \max_{x\in[0,L]} z_\mathrm{b}(x)$.

Consequently, for model with $h > 0$ a stable numerical scheme should have the C-property to avoid non-physical oscillations. However, this property does not handle dry fronts. In fact, in the situation of Figure 1.1 (b) there are regions where $h(x)$ is not well defined, and even if we set $h(x) = 0$ in these regions, the steady state is not satisfied because η in a dry region is higher than in a wet region. To include these cases, Castro et al. defined in [21] the following “extended C-property”:

Definition 1.2.2 (Extended C-property)**.** *A numerical scheme is said to have the* extended C-property *if it exactly reproduces the steady-state solutions*

$$q_u \equiv 0, \quad h(x) = \begin{cases} \eta - b(x) & \text{if } \eta > z_\mathrm{b}(x), \\ 0 & \text{otherwise.} \end{cases}$$

Since h can be zero, we need to renormalize this quantity to avoid dividing by zero (for example in the term q_u^2/h in the second equation of (2.3)). In general, for a given variable q divided by h the corresponding quotient is approximated by

$$\frac{q}{h} \approx \frac{\sqrt{2}qh}{\sqrt{h^4 + \max\{h^4, \varepsilon^4\}}},$$

where $0 < \varepsilon \ll 1$ a small constant (in general it is chosen as $\varepsilon = 10^{-6}$ or smaller), cf., e.g., [47]. This property is fundamental to correctly describe coastal scenarios. However, shallow water models do in general not have this property but, for the model to be compatible with the extended C-property it must be treated. This treatment will be presented below.

1.2.4 Hydrostatic reconstruction

To ensure that our numerical scheme satisfies the extended C-property, we reformulate the shallow-water scheme to properly handle the existence of dry fronts. The main challenge is the preservation of steady states while balancing the flux and source terms, especially when the water height disappears. We proceed by rewriting system (2.3) as

$$\partial_t \boldsymbol{W} + \partial_x \boldsymbol{F}(\boldsymbol{W}) = \boldsymbol{S} z_{\mathrm{b}}',$$

where we define the vectors

$$\boldsymbol{W} := \begin{pmatrix} h \\ q_u \end{pmatrix}, \quad \boldsymbol{F}(\boldsymbol{W}) := \begin{pmatrix} q_u \\ \dfrac{q_u^2}{h} + \dfrac{gh^2}{2} \end{pmatrix}, \quad \boldsymbol{S} := \begin{pmatrix} 0 \\ gh \end{pmatrix}$$

and the matrix of the system, that is, the Jacobian matrix of $\boldsymbol{F}(\boldsymbol{W})$,

$$\boldsymbol{A}(\boldsymbol{W}) = \frac{\partial \boldsymbol{F}(\boldsymbol{W})}{\partial \boldsymbol{W}} = \begin{bmatrix} 0 & 1 \\ gh - \dfrac{q_u^2}{h^2} & 2\dfrac{q_u}{h} \end{bmatrix}$$

that has the eigenvalues

$$\lambda_1 = u - \sqrt{gh}, \quad \lambda_2 = u + \sqrt{gh}.$$

The $\boldsymbol{F}$- and $\boldsymbol{S}$-terms of the numerical flux (2.2) are given by

$$\begin{aligned} &\boldsymbol{F}(\boldsymbol{W}_{i+1}) - \boldsymbol{F}(\boldsymbol{W}_i) - \frac{1}{2}(\sigma_{i+1} - \sigma_i)(\boldsymbol{S}_{i+1} + \boldsymbol{S}_i) \\ &= \begin{pmatrix} q_{u,i+1}^{\nu} - q_{u,i}^{\nu} \\ \dfrac{(q_{u,i+1}^{\nu})^2}{h_i^{\nu}} + g\dfrac{(h_{i+1}^{\nu})^2}{2} - \dfrac{(q_{u,i}^{\nu})^2}{h_{i-1}^{\nu}} - g\dfrac{(h_i^{\nu})^2}{2} \end{pmatrix} + \begin{pmatrix} 0 \\ \dfrac{g}{2}(h_{i+1}^{\nu} + h_i^{\nu})(z_{\mathrm{b},i+1} - z_{\mathrm{b},i}) \end{pmatrix}. \end{aligned} \tag{2.4}$$

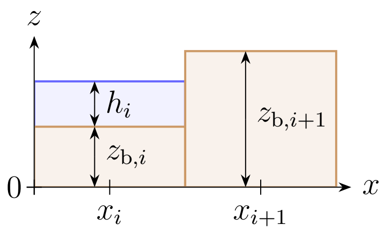

Figure 1.2: Schematic of a dry front.

At steady state, $q^{\nu}_{u,i} = 0$ for all i, and the second component of (2.4) becomes

$$\begin{aligned} &\frac{g}{2}\big((h^{\nu}_{i+1})^2 - (h^{\nu}_i)^2\big) + \frac{g}{2}\big((h^{\nu}_{i+1} + h^{\nu}_i)(z_{\mathrm{b},i+1} - z_{\mathrm{b},i})\big) \\ &= \frac{g}{2}(h^{\nu}_{i+1} - h^{\nu}_i)(h^{\nu}_{i+1} + h^{n}_i) + \frac{g}{2}\big((h^{\nu}_{i+1} + h^{\nu}_i)(z_{\mathrm{b},i+1} - z_{\mathrm{b},i})\big) \\ &= \frac{g}{2}(h^{\nu}_{i+1} + h^{\nu}_i)\big((h^{\nu}_{i+1} + z_{\mathrm{b},i+1}) - (h^{\nu}_i + z_{\mathrm{b},i})\big). \end{aligned} \tag{2.5}$$

In absence of dry fronts this last expression is zero because at steady state, $h + z_{\mathrm{b}}$ is constant, but in a system where $h = 0$ is allowed, it may occur that, for example, $h^{\nu}_i > 0$, $h^{\nu}_{i+1} = 0$, and $h_i < z_{i+1} - z_i$, as is shown in Figure 1.2. In this case the last expression in (2.5) reduces to

$$\frac{g}{2}h^{\nu}_i\big(z_{\mathrm{b},i+1} - (h^{\nu}_i + z_{\mathrm{b},i})\big) < 0;$$

in other words, we will get non-physical velocities that can break our simulation. The hydrostatic reconstruction method, originally introduced by Audusse et al. [6], provides a way to handle this issue by ensuring well-balanced properties in numerical schemes ensuring that the scheme satisfies the extended C-property. The hydrostatic reconstruction is defined as

$$h^{-}_{i+1/2} \coloneqq \max\{z_{\mathrm{b},i} + h_i - z^*, 0\}, \quad h^{+}_{i+1/2} \coloneqq \max\{z_{\mathrm{b},i+1} + h_{i+1} - z^*, 0\}, \tag{2.6}$$

where $z^* \coloneqq \max\{z_{\mathrm{b},i}, z_{\mathrm{b},i+1}\}$, along with

$$(hu)^{-}_{i+1/2} \coloneqq u_i h^{-}_{i+1/2} \quad \text{and} \quad (hu)^{+}_{i+1/2} \coloneqq u_{i+1} h^{+}_{i+1/2}. \tag{2.7}$$

Using this reconstruction we may show that

$$\tilde{G}_{i+1/2} \coloneqq \frac{1}{\Delta x}\left(\frac{1}{2}g\big(h^{+}_{i+1/2}\big)^2 - \frac{1}{2}g\big(h^{-}_{i+1/2}\big)^2\right)$$

is a first-order approximation of $gh\partial_x(h + z_{\mathrm{b}})$; indeed,

$$\begin{aligned} \tilde{G}_{i+1/2} &= \frac{g}{2\Delta x}\big(h^{+}_{i+1/2} + h^{-}_{i+1/2}\big)\big(h^{+}_{i+1/2} - h^{-}_{i+1/2}\big) \\ &= \frac{g}{2\Delta x}\big(h_i + h_{i+1} + \mathcal{O}(\Delta x)\big)\big(\partial_x(h + z_{\mathrm{b}}) + \mathcal{O}(\Delta x)\big), \end{aligned} \tag{2.8}$$

hence this last discretization is consistent with the system and independent of the bottom function.

Furthermore, by using the reconstruction (2.6), (2.7) we can see how the problem of Figure 1.2 is now solved. For that case, $z^* = \max\{z_{\mathrm{b},i}, z_{\mathrm{b},i+1}\} = z_{\mathrm{b},i+1}$, hence

$$h^-_{i+1/2} = \max\{z_{\mathrm{b},i} + h_i - z_{\mathrm{b},i+1}, 0\} = 0, \quad h^+_{i+1/2} = \max\{z_{\mathrm{b},i+1} + h_{i+1} - z_{\mathrm{b},i+1}, 0\} = 0,$$

and therefore $\tilde{G}_{i+1/2} = 0$, which demonstrates that the extended C-property is satisfied.

Finally, as stated before, by using this reconstruction we may treat the system (2.3) as the (shallow water) system of conservation laws

$$\partial_t h + \partial_x(hu) = 0, \quad \partial_t(hu) + \partial_x\left(hu^2 + \frac{1}{2}gh^2\right) = 0.$$

In absence of an explicit bottom term the scheme (2.1), (2.2) now simplifies to (2.1) along with

$$\boldsymbol{D}^{\nu,\pm}_{i+1/2} = \frac{1}{2}\big(\boldsymbol{F}(\boldsymbol{W}^\nu_{i+1}) - \boldsymbol{F}(\boldsymbol{W}^\nu_i) \pm \boldsymbol{Q}^\nu_{i+1/2}(\boldsymbol{W}^\nu_{i+1} - \boldsymbol{W}^\nu_i)\big).$$

1.2.5 Linearized discontinuous non-hydrostatic model (LDNH$_0$ model)

The LDNH$_0$ model of computational fluid dynamics (CFD) accounts for non-hydrostatic forces. In the present model a vertically constant profile for the horizontal velocity u and the vertical velocity w are assumed along with a linear vertical profile for the non-hydrostatic pressure p. This model is given by

$$\partial_t h + \partial_x(hu) = 0, \tag{2.9a}$$

$$\partial_t(hu) + \partial_x\left(hu^2 + \frac{1}{2}gh^2 + hp\right) = -(gh + 2p)z_{\mathrm{b}}', \tag{2.9b}$$

$$\partial_t(hw) + \partial_x(huw) = 2p, \tag{2.9c}$$

$$\partial_x u + 2\frac{w - uz_{\mathrm{b}}'}{h} = 0. \tag{2.9d}$$

Since no evolution equation exists for p, this system is solved numerically by a projection method consisting of two steps per time step of length Δt. As is stated in Sections 1.1.1 and 1.1.3, this procedure mimics Chorin's well-known method for solving the incompressible Navier-Stokes equations.

1. In the first step we solve the system

$$\begin{aligned} \partial_t h + \partial_x(hu) &= 0, \\ \partial_t(hu) + \partial_x\left(hu^2 + \frac{1}{2}gh^2\right) &= -(gh)z_{\mathrm{b}}', \\ \partial_t(hw) + \partial_x(huw) &= 0 \end{aligned} \tag{2.10}$$

that arises from (2.9) by setting the non-hydrostatic pressure p to zero and omitting the last equation (2.9d). The homogeneous version of system (2.10) can be written as a first-order system

$$\partial_t \boldsymbol{W} + \partial_x \boldsymbol{F}(\boldsymbol{W}) = \boldsymbol{0}, \quad \boldsymbol{W} = (h, hu, hw)^{\mathrm{T}}, \quad \boldsymbol{F}(\boldsymbol{W}) = \left(hu, hu^2 + \frac{1}{2}gh^2, huw\right)^{\mathrm{T}},$$

where the eigenvalues of the flux Jacobian matrix $\partial\boldsymbol{F}(\boldsymbol{W})/\partial\boldsymbol{W}$ are given by

$$\lambda_1 = u - \sqrt{gh}, \quad \lambda_2 = u, \quad \lambda_3 = u + \sqrt{gh}, \tag{2.11}$$

and which is therefore hyperbolic. The system (2.10) has the form (1.1), so we can apply the aforementioned discretization and the hydrostatic reconstruction. The intermediate updated variables are given by

$$\boldsymbol{W}_i^{\nu+1/2} = \boldsymbol{W}_i^{\nu} - \frac{\Delta t}{\Delta x}\big(\boldsymbol{D}_{i-1/2}^{\nu,+} + \boldsymbol{D}_{i+1/2}^{\nu,-}\big).$$

In particular, since we are using an HLL viscosity matrix we can rewrite $\boldsymbol{D}_{i+1/2}^{\nu,\pm}$ as

$$\boldsymbol{D}_{i+1/2}^{\nu,\pm} = \frac{1}{2}\Big((1 \pm \alpha_1)\big(\boldsymbol{F}(\boldsymbol{W}_{i+1}^{\nu}) - \boldsymbol{F}(\boldsymbol{W}_i^{\nu})\big) \pm \alpha_0(\boldsymbol{W}_{i+1}^{\nu} - \boldsymbol{W}_i^{\nu})\Big). \tag{2.12}$$

2. Once the first step is calculated, we can proceed with the second step, namely the projection step. In semi-discrete form this step can be written as

$$\frac{1}{\Delta t}(\boldsymbol{W}^{\nu+1} - \boldsymbol{W}^{\nu+1/2}) + \big((\nabla P)^{\nu+1}\big)^{\mathrm{T}} = \boldsymbol{0}, \tag{2.13}$$

where we define

$$\nabla P := \big(0, \partial_x(hp) + 2pz_{\mathrm{b}}', -2p\big) = (0, \widetilde{\nabla P}), \quad \widetilde{\nabla P} := \big(\partial_x(hp) + 2pz_{\mathrm{b}}', -2p\big). \tag{2.14}$$

Next, we define

$$\boldsymbol{X} := \begin{pmatrix} u \\ w \end{pmatrix}, \quad \text{such that} \quad \boldsymbol{W} = \begin{pmatrix} h \\ h\boldsymbol{X} \end{pmatrix}.$$

Now (2.13) can be written as

$$\frac{h^{\nu+1} - h^{\nu+1/2}}{\Delta t} = 0, \tag{2.15a}$$

$$\frac{1}{\Delta t}\big((h\boldsymbol{X})^{\nu+1} - (h\boldsymbol{X})^{\nu+1/2}\big) + \big(\widetilde{\nabla P}^{\nu+1}\big)^{\mathrm{T}} = \boldsymbol{0}. \tag{2.15b}$$

From (2.15a) we get $h^{\nu+1} = h^{\nu+1/2}$, whereas to solve (2.15b) in order to obtain $(h\boldsymbol{X})^{\nu+1}$ (that is, $\boldsymbol{X}^{\nu+1}$ since $h^{\nu+1}$ is known at that moment), we first need to use the constraint

(2.9d), evaluated at time $t_{\nu+1}$, to obtain $p^{\nu+1}$, and thereby $\widetilde{\nabla P}^{\nu+1}$ (cf. (2.14)). Writing (2.15b) component-wise, we get

$$h^{\nu+1}u^{\nu+1} = (hu)^{\nu+1/2} - \Delta t\big(\partial_x(h^{\nu+1}p^{\nu+1}) + 2p^{\nu+1}z_{\mathrm{b}}'\big), \tag{2.16}$$

$$h^{\nu+1}w^{\nu+1} = (hw)^{\nu+1/2} + 2\Delta t p^{\nu+1}. \tag{2.17}$$

On the other hand, (2.9d) can be written as

$$2hw - hu(\partial_x h + 2z_{\mathrm{b}}') + h\partial_x(hu) = 0. \tag{2.18}$$

Then, replacing $h^{\nu+1}$, $(hu)^{\nu+1}$ and $(hw)^{\nu+1}$ from (2.16) and (2.17) in (2.18) yields the desired equation for $p^{\nu+1}$. To state it, for sake of simplicity, we rename the time index $\nu+1/2$ by $*$. The result is

$$\begin{aligned} &2(hw)^* - (hu)^*(\partial_x h^* + 2z_{\mathrm{b}}') + h^*\partial_x(hu)^* + \Delta t\Big(p^{\nu+1}\big(4 + 2z_{\mathrm{b}}'(\partial_x h^* + 2z_{\mathrm{b}}')\big) \\ &+ \partial_x(h^*p^{\nu+1})(\partial_x h^* + 2z_{\mathrm{b}}') - 2h^*\partial_x(z_{\mathrm{b}}'p^{\nu+1}) - h^*\partial_{xx}(h^*p^{\nu+1})\Big) = 0. \end{aligned} \tag{2.19}$$

To solve (2.19) numerically for $p^{\nu+1}$, we discretize this equation on a uniform spatial grid $x_i = i\Delta x$, $i = 1, 2, \ldots, N$. The first-order derivatives are approximated by

$$\partial_x(h^*p^{\nu+1}) \approx \frac{h^*_{i+1}p^{\nu+1}_{i+1} - h^*_{i-1}p^{\nu+1}_{i-1}}{2\Delta x} \tag{2.20}$$

and the second-order derivatives by

$$\partial_{xx}(h^*p^{\nu+1}) \approx \frac{h^*_{i+1}p^{\nu+1}_{i+1} - 2h^*_i p^{\nu+1}_i + h^*_{i-1}p^{\nu+1}_{i-1}}{\Delta x^2}. \tag{2.21}$$

Rewriting (2.19) in a discrete form in terms of unknowns $p_i^{\nu+1}$, we obtain a system

$$T_{i,i-1}p^{\nu+1}_{i-1} + T_{i,i}p^{\nu+1}_i + T_{i,i+1}p^{\nu+1}_{i+1} = P_{0,i}, \quad i = 1, \ldots, N-1,$$

where the coefficients $T_{i,i-1}$, $T_{i,i}$, and $T_{i,i+1}$ arise from the finite-difference approximations (2.20) and (2.21). In matrix form the final system can be written as

$$\boldsymbol{T}\boldsymbol{P} = \boldsymbol{P}_0, \tag{2.22}$$

where

$$\boldsymbol{P} = (p_0^{\nu+1}, p_1^{\nu+1}, \ldots, p_N^{\nu+1})^{\mathrm{T}} \tag{2.23}$$

is the vector of unknowns,

$$\boldsymbol{P}_0 = (p_{0,0}, p_{0,1}, \ldots, p_{0,N})^{\mathrm{T}} \tag{2.24}$$

is the vector of right-hand sides defined by (2.19), that is

$$p_{0,i} = \big(2(hw)^* - (hu)^*(\partial_x h^* + 2z_{\mathrm{b}}') + h^*\partial_x(hu)^*\big)\big|_{x=x_i}, \quad i = 0, \ldots, N, \tag{2.25}$$

> and $\boldsymbol{T} = (T_{i,j})_{0\le i,j\le N}$ is a tridiagonal matrix whose entries are defined by
>
> $$\begin{aligned} T_{i,i} &= 4 + 2\big(z_{\mathrm{b}}'(\partial_x h^* + 2z_{\mathrm{b}}')\big)\big|_{x=x_i} + 2\frac{(h_i^*)^2}{\Delta x^2}, \\ T_{i,i+1} &= (\partial_x h^* + 2z_{\mathrm{b}}')\big|_{x=x_i}\frac{h_{i+1}^*}{2\Delta x} - \frac{h_i^* z_{\mathrm{b}}'|_{x=x_{i+1}}}{\Delta x} - \frac{h_i^* h_{i+1}^*}{\Delta x^2}, \\ T_{i,i-1} &= -(\partial_x h^* + 2z_{\mathrm{b}}')\big|_{x=x_i}\frac{h_{i-1}^*}{2\Delta x} + \frac{h_i^* z_{\mathrm{b}}'|_{x=x_{i-1}}}{\Delta x} - \frac{h_i^* h_{i-1}^*}{\Delta x^2}, \end{aligned}$$
>
> and $T_{i,j} = 0$ for $|i-j| > 1$. Once the system (2.22) is solved, we may evaluate $\widetilde{\nabla P}^{\nu+1}$ via (2.14) and employ (2.15b) to update the values of $\boldsymbol{X}^{\nu+1/2}$ to give $\boldsymbol{X}^{\nu+1}$, and a new iteration is started. In [67] it is shown that the projection method preserves the order of the hyperbolic method for this type of models.

Since $\boldsymbol{T}$ is a tridiagonal matrix we can solve the system efficiently using the Thomas algorithm, which is specialized for tridiagonal systems with $\mathcal{O}(N)$ runtime.

1.2.6 Forest forces

Iimura and Tanaka [46] model the interaction between a tsunami and a forest through various forces and conduct experiments to validate them. Such forces are the bed resistance per unit area τ_{b}, the drag force per unit area f_{D}, and the inertia force per unit area f_{M}. If we define the forest porosity $\theta := 1 - n_{\mathrm{t}}\pi d^2/4$, where n_{t} is the vegetation density (number of trees per unit of area) and d is the diameter of the trees, then these forces are given by

$$\tau_{\mathrm{b}} := gm^2\frac{hu|hu|}{\theta^2 h^{7/3}}, \quad f_{\mathrm{D}} := \frac{C_{\mathrm{D}} d n_{\mathrm{t}}}{2}\frac{hu|hu|}{\theta^2 h}, \quad \text{and} \quad f_{\mathrm{M}} := C_{\mathrm{M}} n_{\mathrm{t}} h \frac{\pi d^2}{4\theta}\partial_t\left(\frac{hu}{h}\right),$$

where m is the Manning roughness coefficient, C_{D} is the drag coefficient, and C_{M} is the mass coefficient. The drag coefficient C_{D} is usually obtained by calibration and is a dimensionless coefficient related to the geometry of the object. If the fluid is a liquid, then C_{D} depends on the Reynolds number; if the fluid is a gas, then C_{D} depends on both the Reynolds number and the Mach number. In our case, the reference area is $A_{\mathrm{ref}} = hd$; in general, A_{ref} depends on the type of drag coefficient. For automobiles and many other objects, the reference area is the projected frontal area of the vehicle. This may not necessarily be the cross-sectional area of the vehicle, depending on where the cross-section is taken. For example, for a sphere $A = \pi r^2$.

Incorporating the forces and the effect of porosity into the non-hydrostatic LDNH_0 model (2.9) we get the non-hydrostatic LDNH_0 model specified for forest forces in final form:

$$\partial_t h + \frac{1}{\theta}\partial_x(hu) = 0, \tag{2.26a}$$

$$\partial_t(hu) + \frac{1}{\theta}\partial_x(hu^2) + \theta\partial_x\left(\frac{gh^2}{2} + hp\right) = -\theta(gh + 2p)z_{\mathrm{b}}' - \theta\tau_{\mathrm{b}} - \theta f_{\mathrm{D}} - \theta f_{\mathrm{M}}, \tag{2.26b}$$

$$\partial_t(hw) + \frac{1}{\theta}\partial_x(huw) = 2p, \tag{2.26c}$$

$$\partial_x u + 2\frac{w - uz_{\mathrm{b}}'}{h} = 0. \tag{2.26d}$$

1.3 Discretization of the LDNH_0 model with forest forces

1.3.1 An unstable discretization

As a first step toward the discretization of (2.26) we define the functions k_1 and k_2 and the constant k_3 by

$$k_1(h) \coloneqq \frac{gm^2}{\theta h^{7/3}}, \quad k_2(h) \coloneqq \frac{C_{\mathrm{D}} d n_{\mathrm{t}}}{2\theta h}, \quad \text{and} \quad k_3 \coloneqq C_{\mathrm{M}} n_{\mathrm{t}} \frac{\pi d^2}{4}.$$

Equation (2.26b) can then be written as

$$\begin{aligned}&\partial_t(hu) + \frac{1}{\theta}\partial_x(hu^2) + \theta\partial_x\left(\frac{gh^2}{2} + hp\right) \\ &= -\theta(gh + 2p)z_{\mathrm{b}}' - (k_1 + k_2)(hu)|hu| - k_3\left(\partial_t(hu) - \frac{hu\partial_t h}{h}\right).\end{aligned}$$

Renaming $q_u \coloneqq hu$ and $q_w \coloneqq hw$ and keeping in mind that (2.26d) plays the role of a constraint, we may write (2.26a), (2.26b) and (2.26c) as the new system

$$\boldsymbol{M}\partial_t\begin{pmatrix} h \\ q_u \\ q_w \end{pmatrix} + \frac{1}{\theta}\partial_x\begin{pmatrix} q_u \\ q_u^2/h \\ q_u q_w/h \end{pmatrix} + \theta g h \partial_x\begin{pmatrix} 0 \\ h + z_{\mathrm{b}} \\ 0 \end{pmatrix} + \theta\partial_x\begin{pmatrix} 0 \\ hp \\ 0 \end{pmatrix} = \begin{pmatrix} 0 \\ -(k_1 + k_2)q_u|q_u| \\ 2p \end{pmatrix},$$

where we define the matrix

$$\boldsymbol{M} \coloneqq \begin{bmatrix} 1 & 0 & 0 \\ -(q_u/h)k_3 & 1 + k_3 & 0 \\ 0 & 0 & 1 \end{bmatrix}.$$

Using the notation

$$\boldsymbol{\mathcal{L}} \coloneqq \begin{pmatrix} \mathcal{L}_u \\ \mathcal{L}_{q_u} \\ \mathcal{L}_{q_w} \end{pmatrix} \coloneqq \frac{1}{\theta}\partial_x\begin{pmatrix} q_u \\ q_u^2/h \\ q_u q_w/h \end{pmatrix} + \theta g h \partial_x\begin{pmatrix} 0 \\ h + z_{\mathrm{b}} \\ 0 \end{pmatrix} \tag{3.1}$$

we may rewrite the system as

$$\partial_t\begin{pmatrix} h \\ q_u \\ q_w \end{pmatrix} + \boldsymbol{C}\boldsymbol{\mathcal{L}} + \boldsymbol{C}\theta\partial_x\begin{pmatrix} 0 \\ hp \\ 0 \end{pmatrix} = \boldsymbol{C}\begin{pmatrix} 0 \\ -(k_1 + k_2)q_u|q_u| \\ 2p \end{pmatrix}, \tag{3.2}$$

where we define

$$\boldsymbol{C} := \boldsymbol{M}^{-1} = \begin{bmatrix} 1 & 0 & 0 \\ q_u k_3/((1+k_3)h) & 1/(1+k_3) & 0 \\ 0 & 0 & 1 \end{bmatrix}.$$

Assume now that $\boldsymbol{\mathcal{L}}_{\boldsymbol{i}}^{\boldsymbol{\nu}}$, $\mathcal{L}_{u,i}^{\nu}$, $\mathcal{L}_{q_u,i}^{\nu}$ and $\mathcal{L}_{q_w,i}^{\nu}$ are discrete versions of $\boldsymbol{\mathcal{L}}$, $\mathcal{L}_u$, $\mathcal{L}_{q_u}$ and $\mathcal{L}_{q_w}$, respectively, associated with $x = x_i$ and $t = t_\nu$. Then a discretization of (3.2) can be formulated as follows, where the term $q_u|q_u|$ is discretized as $q_{u,i}^{\nu+1}|q_{u,i}^{\nu}|$ for stability reasons:

$$\begin{aligned} &h_i^{\nu+1} = h_i^{\nu} - \Delta t \mathcal{L}_{u,i}^{\nu}, \\ &q_{u,i}^{\nu+1} = \left(q_{u,i}^{\nu} - \frac{\Delta t q_{u,i}^{\nu} k_3}{h^{\nu}(1+k_3)} \mathcal{L}_{u,i}^{\nu} - \frac{\Delta t}{1+k_3} \mathcal{L}_{q_u,i}^{\nu} - \theta \Delta t \frac{(\partial_x(hp))_i^{\nu+1}}{1+k_3} \right) \bigg/ \left(1 + \frac{(k_{1,i}^{\nu} + k_{2,i}^{\nu})|q_{u,i}^{\nu}|\Delta t}{1+k_3} \right), \\ &q_{w,i}^{\nu+1} = q_{w,i}^{\nu} - \Delta t \mathcal{L}_{q_w,i}^{\nu} + \Delta t 2 p_i^{\nu+1} \end{aligned} \tag{3.3}$$

along with the constraint (2.26d). Notice that here we do not discretize the non-hydrostatic pressure terms because these are handled by the projection method.

The discrete version of (3.1) is chosen as

$$\boldsymbol{\mathcal{L}}_i^{\nu} = \frac{1}{\theta_i} \big(\boldsymbol{D}_{i-1/2}^{\nu,+} + \boldsymbol{D}_{i+1/2}^{\nu,-} \big),$$

where $\boldsymbol{D}_{i+1/2}^{\nu,\pm}$ is given by (2.12) and

$$\boldsymbol{F}(\boldsymbol{W}) = \left(q_u, \frac{q_u^2}{h} + \frac{gh^2}{2}, \frac{q_u q_w}{h} \right)^{\mathrm{T}}.$$

Since we are using a hydrostatic reconstruction, and as is shown in (2.8), the term $gh\partial_x(h+z_b)$ can be approximated in a conservative form as $\tilde{G}_{i+1/2}$. Thus, the first step is given by

$$\boldsymbol{W}_i^{\nu+1/2} = \boldsymbol{W}_i^{\nu} - \boldsymbol{C}_i^{-1} \frac{\Delta t}{\Delta x} \big(\boldsymbol{D}_{i-1/2}^{\nu,+} + \boldsymbol{D}_{i+1/2}^{\nu,-} \big).$$

This way to discretize the model turned out to be unstable due to the nature of the inertia force, so we should also evaluate $\boldsymbol{C}$ in the control volumes.

1.3.2 A stable discretization

An alternative discretization of the system (2.26) is based on applying the matrix $\boldsymbol{M}^{-1}$ within the discretization. To formulate it, we multiply the model

$$\boldsymbol{M}\partial_t \boldsymbol{W} + \partial_x \boldsymbol{F}(\boldsymbol{W}) + \boldsymbol{B}(\boldsymbol{W})\partial_x \boldsymbol{W} = \sigma' \boldsymbol{S}(\boldsymbol{W}) \tag{3.4}$$

by $\boldsymbol{M}^{-1}$ before space discretization. In (2.26), the term $\partial_x \boldsymbol{F}$ is multiplied by $1/\theta$, but to keep the method simple, we now assume that $1/\theta$ is part of $\boldsymbol{C}$, so in this subsection we utilize

$$\boldsymbol{C} := \frac{1}{\theta} \boldsymbol{M}^{-1}, \tag{3.5}$$

hence pressure terms should be amplified by θ. Consequently, the system (3.4) is now written as

$$\partial_t \boldsymbol{W} + \boldsymbol{C}\partial_x \boldsymbol{F}(\boldsymbol{W}) + \boldsymbol{C}\boldsymbol{B}(\boldsymbol{W})\partial_x \boldsymbol{W} = \sigma'(x)\boldsymbol{C}\boldsymbol{S},$$

and can be discretized as

$$\boldsymbol{W}_i^{\nu+1} = \boldsymbol{N}_i\Big(\boldsymbol{W}_i^{\nu} - \frac{\Delta t}{\Delta x}(\boldsymbol{D}_{i-1/2}^{\nu,+} + \boldsymbol{D}_{i+1/2}^{\nu,-})\Big),$$

where we define the diagonal matrix

$$\boldsymbol{N}_i := \operatorname{diag}\left(1, 1\Big/\left(1 + \frac{(k_{1,i}^{\nu} + k_{2,i}^{\nu})|q_{u,i}^{\nu}|\Delta t}{1+k_3}\right), 1\right) = \operatorname{diag}\left(1, \frac{1+k_3}{1+k_3+(k_{1,i}^{\nu}+k_{2,i}^{\nu})|q_{u,i}^{\nu}|\Delta t}, 1\right) \tag{3.6}$$

and $\boldsymbol{D}_{i+1/2}^{\nu,\pm}$ is given by

$$\begin{aligned}\boldsymbol{D}_{i+1/2}^{\nu,\pm} &= \frac{1}{2}\boldsymbol{C}_{i+1/2}\big(\boldsymbol{F}(\boldsymbol{W}_{i+1}^{\nu}) - \boldsymbol{F}(\boldsymbol{W}_i^{\nu}) \pm \boldsymbol{Q}_{i+1/2}^{\nu}(\boldsymbol{W}_{i+1}^{\nu} - \boldsymbol{W}_i^{\nu})\big)\\ &= \frac{1}{2}\boldsymbol{C}_{i+1/2}\Big((1\pm\alpha_1)\big(\boldsymbol{F}(\boldsymbol{W}_{i+1/2}^{\nu,+}) - \boldsymbol{F}(\boldsymbol{W}_{i+1/2}^{\nu,-})\big) \pm \alpha_0(\boldsymbol{W}_{i+1/2}^{\nu,+} - \boldsymbol{W}_{i+1/2}^{\nu,-})\Big).\end{aligned}$$

Again, we do not consider non-hydrostatic pressure terms in these calculations, because we will use a projection method. However, these terms are easy to incorporate and their contribution must be equal to how it appears in (3.3). The present discretization of the system (2.26) turned out to be stable and will be applied in the remainder of this work.

We remark that the source of the unstable behaviour of the discretization of Section 1.3.1 is the presence of supplementary terms associated with forest forces and porosity. In fact, in the absence of these terms, we have $k_1 = k_2 = k_3 = 0$, and the unstable and stable discretizations coincide.

1.3.3 Eigenvalues

Since external forces are taken into account, the eigenvalues will be different from the typical values $\lambda_0 = u$ and $\lambda_{\pm} = u \pm \sqrt{gh}$ (see (2.11)). We need to calculate the eigenvalues of $\boldsymbol{C}\boldsymbol{A}$, where $\boldsymbol{A} = \partial\boldsymbol{F}/\partial\boldsymbol{W}$ is the matrix of the system and $\boldsymbol{C}$ is given by (3.5), i.e.,

$$\begin{aligned}\boldsymbol{C}\boldsymbol{A} &= \frac{1}{\theta}\begin{bmatrix} 1 & 0 & 0\\ q_u k_3/((1+k_3)h) & 1/(1+k_3) & 0\\ 0 & 0 & 1\end{bmatrix}\begin{bmatrix} 0 & 1 & 0\\ -q_u^2/h^2 + gh\theta^2 & 2q_u/h & 0\\ -q_u q_w/h^2 & q_w/h & q_u/h\end{bmatrix}\\ &= \frac{1}{\theta}\begin{bmatrix} 0 & 1 & 0\\ -q_u^2/((1+k_3)h^2) + gh\theta^2/(1+k_3) & (2+k_3)q_u/((1+k_3)h) & 0\\ -q_u q_w/h^2 & q_w/h & q_u/h\end{bmatrix}.\end{aligned}$$

The eigenvalues of $\boldsymbol{C}\boldsymbol{A}$ are

$$\lambda_1 = \frac{(2+k_3)u - \sqrt{4gh\theta^2(1+k_3) + u^2k_3}}{2\theta(1+k_3)}, \quad \lambda_2 = \frac{u}{\theta}, \quad \lambda_3 = \frac{(2+k_3)u + \sqrt{4gh\theta^2(1+k_3) + u^2k_3}}{2\theta(1+k_3)}.$$

1.3.4 Scheme for the elliptic problem

Once the hyperbolic step has been solved, one needs to correct the intermediate values (indexed by $\nu + 1/2$) and update the pressure value by solving an elliptic problem. As before we rename $()^{\nu+1/2}$ as $()^*$. The analogue of (2.15) now takes the form

$$h^{\nu+1} = h^*, \tag{3.7a}$$

$$(hu)^{\nu+1} = (hu)^* - \Delta t\theta \frac{2p^{\nu+1}z_{\mathrm{b}}' + \partial_x(hp)^{\nu+1}}{1 + k_3 + (k_1^* + k_2^*)|h^*u^*|\Delta t}, \tag{3.7b}$$

$$(hw)^{\nu+1} = (hw)^* + 2\Delta t p^{\nu+1}, \tag{3.7c}$$

$$0 = 2(hw)^{\nu+1} - (hu)^{\nu+1}(\partial_x h^{\nu+1} + 2z_{\mathrm{b}}') + h^{\nu+1}\partial_x(hu)^{\nu+1}. \tag{3.7d}$$

Now, replacing (3.7a), (3.7b) and (3.7c) in (3.7d) yields

$$\begin{aligned}&2(hw)^* - (hu)^*(\partial_x h^* + 2z_{\mathrm{b}}') + h^*\partial_x(hu)^* + \Delta t\Big(p^{\nu+1}\big(4 + 2z_{\mathrm{b}}'(\partial_x h^* + 2z_{\mathrm{b}}')f^*\big)\\ &+ \partial_x(h^*p^{\nu+1})\big(f^*(\partial_x h^* + 2z_{\mathrm{b}}') - h^*\partial_x(f^*)\big) - 2h^*\partial_x(f^*z_{\mathrm{b}}'p^{\nu+1}) - h^*f^*\partial_{xx}(h^*p^{\nu+1})\Big) = 0,\end{aligned} \tag{3.8}$$

where we define

$$f := \frac{\theta}{1 + k_3 + (k_1 + k_2)|hu|\Delta t}.$$

As we stated before, (3.8) can be solved numerically by writing the discretized problem in the form $\boldsymbol{A}\boldsymbol{P} = \boldsymbol{P}_0$, where $\boldsymbol{P}_0$ is given by (2.24) and (2.25), $\boldsymbol{P}$ is the vector of unknowns (2.23) and $\boldsymbol{A} = (A_{i,j})$ this time is a tridiagonal matrix given by

$$\begin{aligned}A_{i,i} &= 4 + 2\big(z_{\mathrm{b}}'(\partial_x h^* + 2z_{\mathrm{b}}')f\big)_i + 2\frac{(h_i^*)^2 f_i^*}{\Delta x^2},\\ A_{i,i+1} &= \big(f^*(\partial_x h^* + 2z_{\mathrm{b}}') - h^*\partial_x f^*\big)_i \frac{h_{i+1}^*}{2\Delta_x} - \frac{h_i^*(f^*z_{\mathrm{b}}')_{i+1}}{\Delta x} - \frac{h_i^*h_{i+1}^*f_i^*}{\Delta x^2},\\ A_{i,i-1} &= -\big(f^*(\partial_x h^* + 2z_{\mathrm{b}}') - h^*\partial_x f^*\big)_i \frac{h_{i-1}^*}{2\Delta_x} + \frac{h_i^*(f^*z_{\mathrm{b}}')_{i-1}}{\Delta x} - \frac{h_i^*h_{i-1}^*f_i^*}{\Delta x^2},\end{aligned}$$

and $A_{i,j} = 0$ for $|i - j| > 1$. Inverting this matrix we can find $\boldsymbol{P} = \boldsymbol{A}^{-1}\boldsymbol{P}_0$. Then we can correct the values of u and w.

1.4 LDNH$_0$ multilayer model

1.4.1 Definition of multiple layers

According to standard definitions in the multilayer approach we subdivide the vertical interval between $z_{\mathrm{b}}(x)$ and $z_{\mathrm{b}}(x)+h(x,t)$ into N layers, layers 1 to N, of thickness $h_\alpha(x,t)$, $\alpha = 1, \ldots, N$,

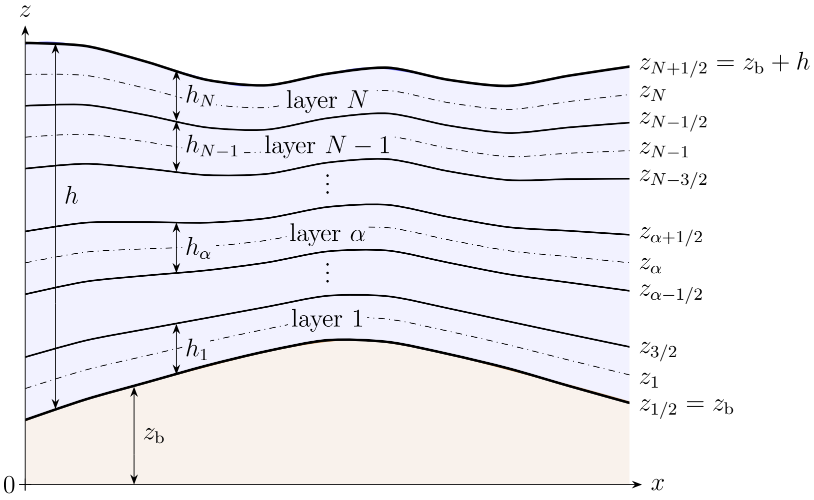

Figure 1.3: Definition of layers 1 to N, their interfaces (solid curves), and centerlines (dash-dotted).

such that $h_1(x,t) + \cdots + h_N(x,t) = h(x,t)$ or equivalently, $l_1 + \cdots + l_N = 1$, where $l_\alpha = h_\alpha/h$, see Figure 1.3. Moreover, we define the layer interfaces

$$z_{\alpha+1/2} \coloneqq z_{\alpha+1/2}(x,t) \coloneqq z_b + \sum_{\beta=0}^{\alpha} l_\beta h, \quad \alpha = 0, \dots, N,$$

and the layer centerlines

$$z_\alpha \coloneqq z_\alpha(x,t) \coloneqq z_b + \sum_{\beta=0}^{\alpha-1} l_\beta h + l_\alpha \frac{h}{2}, \quad \alpha = 1, \dots, N.$$

where $z_{1/2} = z_b$ is the bottom. This means that $z_{\alpha+1/2} - z_{\alpha-1/2} = l_\alpha h = h_\alpha$.

1.4.2 LDNH$_0$ multilayer model (without forces and porosity)

The shallow water equations are derived from a vertical integration of the Euler equations for an ideal fluid. In the same way, in the derivation of the LDNH$_0$ model we can subdivide vertical integration into multiple parts, each one with its own velocity, pressure, and size (layer thickness). The balance equations in differential form for N layers resulting from the previous discussion are

$$\begin{aligned}
&\partial_t h + \partial_x(h\bar{\bar{u}}) = 0 \quad \text{with} \quad \bar{\bar{u}} = l_1\bar{u}_1 + \cdots + l_N\bar{u}_N,\\
&\partial_t(h_\alpha\bar{u}_\alpha) + \partial_x(h_\alpha\bar{u}_\alpha^2 + h_\alpha q_\alpha) - \partial_x z_{\alpha+1/2} q_{\alpha+1/2} + \partial_x z_{\alpha-1/2} q_{\alpha-1/2}\\
&= -g h_\alpha \partial_x \eta + \tilde{u}_{\alpha+1/2}\Gamma_{\alpha+1/2} - \tilde{u}_{\alpha-1/2}\Gamma_{\alpha-1/2},\\
&\partial_t(h_\alpha\bar{w}_\alpha) + \partial_x(h_\alpha\bar{u}_\alpha\bar{w}_\alpha) + q_{\alpha+1/2} - q_{\alpha-1/2}
\end{aligned}$$

$$= \tilde{w}_{\alpha+1/2}\Gamma_{\alpha+1/2} - \tilde{w}_{\alpha-1/2}\Gamma_{\alpha-1/2}, \quad \alpha = 1, \dots, N,$$

with $q_\alpha = \frac{1}{2}(q_{\alpha+1/2} + q_{\alpha-1/2})$ along with the diagnostic equations

$$\begin{aligned} \bar{w}_\alpha - \bar{w}_{\alpha-1} - (\bar{u}_\alpha - \bar{u}_{\alpha-1})\partial_x z_{\alpha-1/2} - \frac{1}{2}(h_{\alpha-1}\partial_x \bar{u}_{\alpha-1} + h_\alpha \partial_x \bar{u}_\alpha) = 0, \quad \alpha = 2, \dots, N, \\ \bar{w}_1 - \bar{u}_1 \partial_x z_{\mathrm{b}} + \frac{1}{2} h_1 \partial_x \bar{u}_1 = 0 \end{aligned}$$

and the boundary condition $q_{N+1/2} = 0$. (Here we recall that especially in the geophysical and meteorological context, a diagnostic equation is one that links the values of its variables simultaneously, either because the equation (or model) is time-independent, or the variables all refer to the values at the same time.)

The mass transfer term is given by

$$\Gamma_{\alpha+1/2} = \sum_{\beta=1}^{\alpha} \partial_x \big(h_\beta (\bar{u}_\beta - \bar{\bar{u}}) \big).$$

Moreover, we define

$$\begin{aligned} \tilde{u}_{\alpha+1/2} &:= (1 - \gamma_{\alpha+1/2})\bar{u}_{\alpha+1} + \gamma_{\alpha+1/2}\bar{u}_\alpha, \\ \tilde{w}_{\alpha+1/2} &:= (1 - \gamma_{\alpha+1/2})\left(\bar{w}_{\alpha+1} + \frac{h_{\alpha+1}}{2}\partial_x \bar{u}_{\alpha+1} \right) + \gamma_{\alpha+1/2}\left(\bar{w}_\alpha - \frac{h_\alpha}{2}\partial_x \bar{u}_\alpha \right) \end{aligned}$$

for any $\gamma_{\alpha+1/2} \in [0, 1]$. For sake of simplicity from we now rename $\bar{u}_\alpha$ as u_α and $\bar{w}_\alpha$ as w_α.

1.4.3 Effect of porosity

The porosity θ is a parameter related to the fraction of area available to be occupied by the fluid. In our case, since the vegetation uses a physical area, some regions cannot by fully filled by fluid. To determine how porosity affects the mass conservation equation we consider an infinitesimal element of area of the spatial domain $\Delta x \Delta h$ in a region with vegetation. In the x-direction we have an effective length $\theta_x \Delta x$ and in the z-direction an effective height $\theta_z \Delta h$. Then, if fluid with velocity u enters the area during a time interval of length Δt time, the balance equation becomes

$$\theta_x \theta_z \Delta x \Delta h = \big(hu(x_0) - hu(x_0 + \theta_x \Delta x) \big) \Delta t.$$

Then,

$$\frac{\theta_z \Delta h}{\Delta t} = \frac{hu(x_0) - hu(x_0 + \theta_x \Delta x)}{\theta_x \Delta x} \approx -\partial_x (hu).$$

Simplifying, renaming θ_z as θ and taking the limit we obtain

$$\theta \partial_t h + \partial_x (hu) = 0.$$

1.4.4 Transfer terms

We now derive a formula for the transfer terms between layers. Let us consider the balance equation for layer α, namely

$$\theta_\alpha \partial_t h_\alpha + \partial_x (h_\alpha u_\alpha) = \frac{1}{l_\alpha}(\Gamma_{\alpha+1/2} - \Gamma_{\alpha-1/2}), \quad \alpha = 1, \dots, N.$$

Now, consider for a fixed $\alpha \in \{1, \dots, N\}$ the sums of the these equations from layer $\beta = 1$ to layer $\beta = \alpha$ and from layer $\beta = \alpha + 1$ to the last layer $\beta = N$. This yields

$$\sum_{\beta=1}^{\alpha} l_\beta \theta_\beta \partial_t h_\beta + \sum_{\beta=1}^{\alpha} l_\beta \partial_x (h_\beta u_\beta) = \Gamma_{\alpha+1/2} - \Gamma_{1/2},$$
$$\sum_{\beta=\alpha+1}^{N} l_\beta \theta_\beta \partial_t h_\beta + \sum_{\beta=\alpha+1}^{N} l_\beta \partial_x (h_\beta u_\beta) = \Gamma_{N+1/2} - \Gamma_{\alpha+1/2}.$$

If all layers have the same height at a given x-position, that is setting $h_\beta = h/N$ for all β, we obtain

$$(\partial_t h) \sum_{\beta=1}^{\alpha} \frac{\theta_\beta}{N} + \sum_{\beta=1}^{\alpha} \partial_x (h_\beta u_\beta) = \Gamma_{\alpha+1/2} - \Gamma_{1/2}, \tag{4.1}$$

$$(\partial_t h) \sum_{\beta=\alpha+1}^{N} \frac{\theta_\beta}{N} + \sum_{\beta=\alpha+1}^{N} \partial_x (h_\beta u_\beta) = \Gamma_{N+1/2} - \Gamma_{\alpha+1/2} \tag{4.2}$$

along with the equivalence

$$\bar{\theta} = \frac{1}{h} \int_{z_{1/2}}^{z_{N+1/2}} \theta(z) dz = \frac{1}{h} \sum_{\beta=1}^{N} \int_{z_{\beta-1/2}}^{z_{\beta+1/2}} \theta(z)\, \mathrm{d}z = \sum_{\beta=1}^{N} \frac{\theta_\beta}{N}.$$

Then we can rewrite equation (4.2) as

$$(\partial_t h) \left(\bar{\theta} - \sum_{\beta=1}^{\alpha} \frac{\theta_\beta}{N} \right) + \sum_{\beta=\alpha+1}^{N} \partial_x (h_\beta u_\beta) = \Gamma_{N+1/2} - \Gamma_{\alpha+1/2}. \tag{4.3}$$

To find the transfer terms we multiply (4.1) by $\bar{\theta} - \sum_{\beta=1}^{\alpha} \theta_\beta / N$ and (4.3) by $\sum_{\beta=1}^{\alpha} \theta_\beta / N$. Subtracting the results we obtain

$$\begin{aligned} &\left(\bar{\theta} - \sum_{\beta=1}^{\alpha} \frac{\theta_\beta}{N} \right) \sum_{\beta=1}^{\alpha} \partial_x (h_\beta u_\beta) - \left(\sum_{\beta=1}^{\alpha} \frac{\theta_\beta}{N} \right) \sum_{\beta=\alpha+1}^{N} \partial_x (h_\beta u_\beta) \\ &= \left(\bar{\theta} - \sum_{\beta=1}^{\alpha} \frac{\theta_\beta}{N} \right) (\Gamma_{\alpha+1/2} - \Gamma_{1/2}) - \left(\sum_{\beta=1}^{\alpha} \frac{\theta_\beta}{N} \right) (\Gamma_{N+1/2} - \Gamma_{\alpha+1/2}). \end{aligned} \tag{4.4}$$

Since the boundary transfer terms are zero, i.e., $\Gamma_{1/2} = \Gamma_{N+1/2} = 0$, (4.4) reduces to an identity that can be written as

$$\Gamma_{\alpha+1/2} = \sum_{\beta=1}^{N} \gamma_{\alpha,\beta}\partial_x(h_\beta u_\beta), \quad \text{where} \quad \gamma_{\alpha,\beta} := \begin{cases} 1 - \displaystyle\sum_{k=1}^{\alpha} \frac{\theta_k}{N\bar{\theta}} & \text{for } \alpha \geq \beta, \\ -\displaystyle\sum_{k=1}^{\alpha} \frac{\theta_k}{N\bar{\theta}} & \text{for } \alpha < \beta. \end{cases}$$

1.4.5 Drag and inertia forces for the multilayer system

A widely used definition of the drag force is

$$f_{\mathrm{D}} = \frac{1}{2}\rho C_{\mathrm{D}} A_{\mathrm{v}} |u| u,$$

where A_{v} is the effective "vertical" side face area of the object and C_{D} is the drag coefficient. Furthermore, to describe properties of individual trees, we use the height coordinate ζ that is measured from the ground surface, identified here with z_{b}. For trees, Tanaka et al. [70] characterize C_{D} by

$$C_{\mathrm{D}} = C_{\mathrm{D,ref}}\overline{c_{\mathrm{tr}}c_{\mathrm{le}}},$$

where we denote by $\overline{c_{\mathrm{tr}}c_{\mathrm{le}}}$ the vertical average of the product of the coefficients $c_{\mathrm{tr}}(\zeta)$ and $c_{\mathrm{le}}(\zeta)$ that represent the effect of the trunk and leaves of the trees, respectively:

$$\overline{c_{\mathrm{tr}}c_{\mathrm{le}}} := \frac{1}{h}\int_0^h c_{\mathrm{tr}}(\zeta)c_{\mathrm{le}}(\zeta)\,\mathrm{d}\zeta$$

and $A_{\mathrm{v}} = dh$. Within a multilayer system the averages must be calculated for each layer α ($\alpha = 1, \dots, N$). This is done by defining

$$C_{\mathrm{D},\alpha} := C_{\mathrm{D,ref}}(\overline{c_{\mathrm{tr}}c_{\mathrm{le}}})_\alpha, \quad \text{where} \quad (\overline{c_{\mathrm{tr}}c_{\mathrm{le}}})_\alpha := \frac{1}{h_\alpha}\int_{z_{\alpha-1/2}-z_{\mathrm{b}}}^{z_{\alpha+1/2}-z_{\mathrm{b}}} c_{\mathrm{tr}}(\zeta)c_{\mathrm{le}}(\zeta)\,\mathrm{d}\zeta, \quad \alpha = 1, \dots, N.$$

On the other hand, if the diameter of a tree at height ζ is $d(\zeta)$, then we employ

$$A_{\mathrm{v},\alpha} := h_\alpha \bar{d}_\alpha, \quad \text{where} \quad \bar{d}_\alpha := \frac{1}{h_\alpha}\int_{z_{\alpha-1/2}-z_{\mathrm{b}}}^{z_{\alpha+1/2}-z_{\mathrm{b}}} d(\zeta)\,\mathrm{d}\zeta, \quad \alpha = 1, \dots, N. \tag{4.5}$$

If we assume that the trees are symmetric along the z-axis the layer-specific transversal area $A_{\mathrm{t},\alpha}$ of each tree is $A_{\mathrm{t},\alpha} := \pi(\bar{d}_\alpha)^2/4$ for $\alpha = 1, \dots, N$. Summarizing all ingredients, we obtain that the drag force for one tree associated with layer α is given by

$$f_{\mathrm{t},\alpha} := \frac{1}{2}\rho C_{\mathrm{D},\alpha} A_{\mathrm{v},\alpha}|u_\alpha|u_\alpha = \frac{1}{2}\rho C_{\mathrm{D,ref}}(\overline{c_{\mathrm{tr}}c_{\mathrm{le}}})_\alpha \bar{d}_\alpha |h_\alpha u_\alpha| u_\alpha, \quad \alpha = 1, \dots, N.$$

On the other hand, Tanaka et al. [70] calculate the effective density n_{t} of the forest as

$$n_{\mathrm{t}} = \frac{dnc_{\mathrm{tr}}c_{\mathrm{le}}}{A_{\mathrm{F}}},$$

where A_{F} is the forest area and n denotes the number of trees divided by the forest length in flow direction. Consequently, the effective forest density $n_{\mathrm{t},\alpha}$ and the corresponding porosity θ_α for layer α are given by the respective expressions

$$n_{\mathrm{t},\alpha} = \frac{\bar{d}_\alpha n(\overline{c_{\mathrm{tr}}c_{\mathrm{le}}})_\alpha}{A_{\mathrm{F}}}, \quad \theta_\alpha = 1 - \frac{n_{\mathrm{t}\alpha}\pi\bar{d}_\alpha^2}{4}.$$

Combining all ingredients we obtain the total forest drag force associated with layer α

$$f_{\mathrm{D},\alpha} = \frac{n_{\mathrm{t},\alpha}}{\theta_\alpha^2} f_{\mathrm{t},\alpha} = \frac{1}{2}\frac{n_{\mathrm{t},\alpha}}{\theta_\alpha^2}\rho C_{\mathrm{D,ref}}(\overline{c_{\mathrm{tr}}c_{\mathrm{le}}})_\alpha \bar{d}_\alpha |h_\alpha u_\alpha| u_\alpha, \quad \alpha = 1, \dots, N.$$

Finally, assuming radial symmetry of the trees along the z-axis we obtain the inertia force

$$f_{\mathrm{M},\alpha} = C_{\mathrm{M}} \frac{n_{\mathrm{t},\alpha}}{\theta_\alpha} h_\alpha \frac{\pi\bar{d}_\alpha^2}{4} \partial_t \left(\frac{h_\alpha u_\alpha}{h_\alpha}\right), \quad \alpha = 1, \dots, N.$$

1.4.6 Gauckler-Manning friction and viscosity

The friction force with respect to the ground τ_α is present in the bottom layer only ($\alpha = 1$). Therefore, we define

$$\tau_\alpha := k_{1,\alpha}|h_\alpha u_\alpha| h_\alpha u_\alpha = \begin{cases} \dfrac{gm^2|u_\alpha|u_\alpha}{\theta_\alpha h^{1/3}} & \text{for } \alpha = 1, \\ 0 & \text{for } \alpha = 2, \dots, N. \end{cases}$$

The upper layers will be not affected directly by this force, but physically, the interaction with the ground is transferred to the upper layers by the viscosity of the fluid. This phenomenon is modeled by vertical viscosity terms $K_{\alpha+1/2}$ and $K_{\alpha-1/2}$ defined by

$$K_{\alpha+1/2} := -\eta_0 \frac{u_{\alpha+1} - u_\alpha}{h_{\alpha+1} + h_\alpha}, \tag{4.6}$$

where we take into account that $K_{N+1/2} = 0$ and $K_{1/2} = -\tau_1$ and η_0 is the viscosity constant of the fluid. These viscosity therms are a simplified expression of the general case when each layer can have different size and fluids, see [31] for further explanations.

1.4.7 Forces in the model

Now, combining all the forces with the multilayer model, we arrive at the following governing equations of the multilayer approach:

$$\begin{aligned}
&\partial_t h_\alpha + \frac{\partial_x(h_\alpha u_\alpha)}{\theta_\alpha} - \frac{\Gamma_{\alpha+1/2}}{\theta_\alpha} + \frac{\Gamma_{\alpha-1/2}}{\theta_\alpha} = 0,\\
&\partial_t(h_\alpha u_\alpha) + \frac{\partial_x(h_\alpha u_\alpha^2)}{\theta_\alpha} + \theta_\alpha \partial_x(h_\alpha q_\alpha) - \theta_\alpha \partial_x z_{\alpha+1/2} q_{\alpha+1/2} + \theta_\alpha \partial_x z_{\alpha-1/2} q_{\alpha-1/2}\\
&= -g h_\alpha \theta_\alpha \partial_x \eta + \frac{\tilde{u}_{\alpha+1/2}\Gamma_{\alpha+1/2}}{\theta_\alpha} - \frac{\tilde{u}_{\alpha-1/2}\Gamma_{\alpha-1/2}}{\theta_\alpha} - f_{\mathrm{D}\alpha} - f_{\mathrm{M}\alpha} + \frac{K_{\alpha-1/2}}{\theta_\alpha} - \frac{K_{\alpha+1/2}}{\theta_\alpha},\\
&\partial_t(h_\alpha w_\alpha) + \frac{\partial_x(h_\alpha u_\alpha w_\alpha)}{\theta_\alpha} + q_{\alpha+1/2} - q_{\alpha-1/2} = \frac{\tilde{w}_{\alpha+1/2}\Gamma_{\alpha+1/2}}{\theta_\alpha} - \frac{\tilde{w}_{\alpha-1/2}\Gamma_{\alpha-1/2}}{\theta_\alpha},
\end{aligned} \tag{4.7}$$

where $\alpha = 1, \dots, N$. Based on our previous calculations we get that we obtain the same kind of system of equations as (2.26) but this time for each layer.

1.4.8 Solving the first-order system

Initially, our focus is on solving the first-order equations of the problem. Therefore, we assume that all pressures in (4.7) are zero during this stage of the analysis. The impact of viscosity will be incorporated in the final stages of the calculations and, hence, is disregarded in this section. Similarly to our previous approach, we derive the flow rate equation by incorporating the relevant external forces, which can be expressed as

$$\begin{aligned}
&\partial_t(h_\alpha u_\alpha) + \frac{\partial_x(h_\alpha u_\alpha^2)}{\theta_\alpha} - \frac{\tilde{u}_{\alpha+1/2}\Gamma_{\alpha+1/2}}{\theta_\alpha} + \frac{\tilde{u}_{\alpha-1/2}\Gamma_{\alpha-1/2}}{\theta_\alpha}\\
&= -g h_\alpha \theta_\alpha \partial_x \eta - k_{2,\alpha}(h_\alpha u_\alpha)|h_\alpha u_\alpha| - k_{3,\alpha}\left(\partial_t(h_\alpha u_\alpha) - \frac{h_\alpha u_\alpha \partial_t h_\alpha}{h_\alpha}\right),\\
&(1 + k_{3,\alpha})\partial_t(h_\alpha u_\alpha) - k_{3,\alpha} u_\alpha \partial_t h_\alpha + \frac{\partial_x(h_\alpha u_\alpha^2)}{\theta_\alpha} - \frac{\tilde{u}_{\alpha+1/2}\Gamma_{\alpha+1/2}}{\theta_\alpha} + \frac{\tilde{u}_{\alpha-1/2}\Gamma_{\alpha-1/2}}{\theta_\alpha}\\
&= -g h_\alpha \theta_\alpha \partial_x \eta - k_{2,\alpha}(h_\alpha u_\alpha)|h_\alpha u_\alpha|,
\end{aligned}$$

where we define the constants

$$k_{2,\alpha} := \frac{C_{\mathrm{D},\alpha} d_\alpha n_{\mathrm{t},\alpha}}{2\theta h_\alpha} \quad \text{and} \quad k_{3,\alpha} = C_{\mathrm{M}} \frac{n_{\mathrm{t},\alpha}\pi \bar{d}_\alpha^2}{4}.$$

For every $\alpha = 1, \dots, N$ we need to solve the system of balance equations

$$\boldsymbol{\mathcal{M}}_\alpha \partial_t \begin{pmatrix} h_\alpha \\ h_\alpha u_\alpha \\ h_\alpha w_\alpha \end{pmatrix} + \frac{1}{\theta_\alpha}\partial_x \begin{pmatrix} h_\alpha u_\alpha \\ h_\alpha u_\alpha^2 \\ h_\alpha u_\alpha w_\alpha \end{pmatrix} + \frac{1}{\theta_\alpha}\begin{bmatrix} \boldsymbol{B}_{h,\alpha} \\ \boldsymbol{B}_{hu,\alpha} \\ \boldsymbol{B}_{hw,\alpha} \end{bmatrix} \partial_x \boldsymbol{W} = -\begin{pmatrix} 0 \\ k_{2,\alpha}(h_\alpha u_\alpha)|h_\alpha u_\alpha| \\ 0 \end{pmatrix}, \tag{4.8}$$

where we define

$$\boldsymbol{\mathcal{M}}_\alpha := \begin{bmatrix} 1 & 0 & 0 \\ -u_\alpha k_{3,\alpha} & 1 + k_{3,\alpha} & 0 \\ 0 & 0 & 1 \end{bmatrix}$$

and $\boldsymbol{B}_{h,\alpha}$, $\boldsymbol{B}_{hu,\alpha}$ and $\boldsymbol{B}_{hw,\alpha}$ represent the corresponding rows of $\boldsymbol{B}_\alpha$. Since the transfer terms depend on the velocities of all layers, $\boldsymbol{W}$ is a vector defined as

$$\boldsymbol{W} := (h_1, h_1u_1, h_1w_1, h_2, h_2u_2, h_2w_2, \ldots, h_N, h_Nu_N, h_Nw_N)^{\mathrm{T}} \in \mathbb{R}^{3N}.$$

Multiplying (4.8) from the left by

$$\boldsymbol{\mathcal{C}}_\alpha := \boldsymbol{\mathcal{M}}_\alpha^{-1} = \begin{bmatrix} 1 & 0 & 0 \\ u_\alpha k_{3,\alpha}/(1 + k_{3,\alpha}) & 1/(1 + k_{3,\alpha}) & 0 \\ 0 & 0 & 1 \end{bmatrix}$$

we obtain

$$\partial_t \begin{pmatrix} h_\alpha \\ h_\alpha u_\alpha \\ h_\alpha w_\alpha \end{pmatrix} + \frac{1}{\theta_\alpha}\mathcal{C}_\alpha \partial_x \begin{pmatrix} h_\alpha u_\alpha \\ h_\alpha u_\alpha^2 \\ h_\alpha u_\alpha w_\alpha \end{pmatrix} + \frac{1}{\theta_\alpha}\mathcal{C}_\alpha \begin{bmatrix} \boldsymbol{B}_{h,\alpha} \\ \boldsymbol{B}_{hu,\alpha} \\ \boldsymbol{B}_{hw,\alpha} \end{bmatrix} \partial_x \boldsymbol{W} = -\boldsymbol{\mathcal{C}}_\alpha \begin{pmatrix} 0 \\ k_{2,\alpha}(h_\alpha u_\alpha)|h_\alpha u_\alpha| \\ 0 \end{pmatrix}. \quad (4.9)$$

Now we can use the FV method described before to numerically solve the system of PDEs (4.9), but to improve the stability of the numerical scheme we discretize the remaining external forces in a semi-implicit form, this means that $h_\alpha u_\alpha |h_\alpha u_\alpha|$ is evaluated as

$$h_\alpha u_\alpha |h_\alpha u_\alpha| \approx (h_\alpha u_\alpha)^{\nu+1} |h_\alpha u_\alpha|^\nu.$$

Consequently, the hyperbolic scheme for layer α becomes

$$\boldsymbol{W}_{\alpha,i}^{\nu+1} = \boldsymbol{N}_{\alpha,i}\Big(\boldsymbol{W}_{\alpha,i}^\nu - \frac{\Delta t}{\Delta x}\big(\boldsymbol{D}_{\alpha,i-1/2}^{\nu,+} + \boldsymbol{D}_{\alpha,i+1/2}^{\nu,-}\big)\Big),$$

where the diagonal matrix $\boldsymbol{N}_\alpha$ is defined analogously to (3.6); namely we here get

$$\boldsymbol{N}_{\alpha,i} := \mathrm{diag}\bigg(1, 1 \Big/ \bigg(1 + \frac{k_{2,\alpha}^\nu |h_{\alpha,i}^\nu u_{\alpha,i}^\nu| \Delta t}{1 + k_{3,\alpha}}\bigg), 1\bigg) = \mathrm{diag}\bigg(1, \frac{1 + k_{3,\alpha}}{1 + k_{3,\alpha} + k_{2,\alpha}^\nu |h_{\alpha,i}^\nu u_{\alpha,i}^\nu| \Delta t}, 1\bigg),$$

and

$$\begin{aligned}\boldsymbol{D}_{\alpha,i+1/2}^{\nu,\pm} = \frac{1}{2\theta_{\alpha,i+1/2}^\nu}\boldsymbol{\mathcal{C}}_{\alpha,i+1/2}^\nu \big(&\boldsymbol{F}(\boldsymbol{W}_{\alpha,i+1}^\nu) - \boldsymbol{F}(\boldsymbol{W}_{\alpha,i}^\nu) + \boldsymbol{B}_{\alpha,i+1/2}^\nu(\boldsymbol{W}_{\alpha,i+1}^\nu - \boldsymbol{W}_{\alpha,i}^\nu) \\ &\pm \boldsymbol{Q}_{\alpha,i+1/2}^\nu(\boldsymbol{W}_{\alpha,i+1}^\nu - \boldsymbol{W}_{\alpha,i}^\nu)\big).\end{aligned}$$

1.4.9 Projection matrix

Similarly to (3.7) the elliptic problems for each layer can be written as

$$\begin{aligned} h^{\nu+1} &= h^* \\ (h_\alpha u_\alpha)^{\nu+1} &= (h_\alpha u_\alpha)^* + \Delta t f_\alpha^* \big(\partial_x z^*_{\alpha+1/2} q^{\nu+1}_{\alpha+1/2} - \partial_x z^*_{\alpha-1/2} q^{\nu+1}_{\alpha-1/2} - h^*_\alpha q^{\nu+1}_\alpha\big), \\ (h_\alpha w_\alpha)^{\nu+1} &= (h_\alpha w_\alpha)^* - \Delta t \big(q^{\nu+1}_{\alpha+1/2} - q^{\nu+1}_{\alpha-1/2}\big), \end{aligned} \tag{4.10}$$

where f_α represents the multiplicative factors caused by the treatment of the vegetation forces, i.e.,

$$f_\alpha = \frac{\theta_\alpha}{1 + k_{3,\alpha} + k_{2,\alpha}|h_\alpha u_\alpha|\Delta t}.$$

For $\alpha = 2, \ldots, N$ the constraints can be rewritten as

$$h_\alpha w_\alpha - h_\alpha w_{\alpha-1} - h_\alpha u_\alpha \partial_x z_\alpha + h_{\alpha-1} u_{\alpha-1} \partial_x z_{\alpha-1} + \frac{h_\alpha}{2} \partial_x \left(h_\alpha u_\alpha + h_{\alpha-1} u_{\alpha-1}\right) = 0 \tag{4.11}$$

and for the first layer ($\alpha = 1$) as

$$h_1 w_1 - h_1 u_1 \partial_x z_1 + \frac{h_1}{2} \partial_x (h_1 u_1) = 0 \tag{4.12}$$

Typically, the variables are evaluated in volumes while the pressures are defined on the edges. To apply the projection method, we discretize the terms $(h_\alpha u_\alpha)^{\nu+1}$ and $(h_\alpha w_\alpha)^{\nu+1}$ on the edges and substitute them into the constraint equations (4.11) and (4.12). Alternatively, we can substitute these terms into (4.11) and (4.12) first and then discretize them "at $i+1/2$", that is, on the edges. In this context, we have opted for the latter approach, which yields the equation

$$\begin{aligned} \frac{4N^2 P^*}{\Delta t} &+ q_{\alpha-1/2}\big(8N^2 + f_\alpha \phi_\alpha^2 + f_{\alpha-1}\phi_{\alpha-1}^2 - h\partial_x(f_\alpha \phi_\alpha) + h\partial_x(f_{\alpha-1}\phi_{\alpha-1})\big) \\ &- (\partial_x q_{\alpha-1/2})\big(h\partial_x(f_\alpha h) + h\partial_x(f_{\alpha-1} h)\big) - \partial_{xx} q_{\alpha-1/2}\big(h^2(f_\alpha + f_{\alpha-1})\big) \\ &+ q_{\alpha-3/2}\big(2N^2 + f_{\alpha-1}\phi_{\alpha-1}^2 + h\partial_x(f_{\alpha-1}\phi_{\alpha-1})\big) \\ &+ (\partial_x q_{\alpha-3/2})\big(h f_{\alpha-1}\phi_{\alpha-1} + h^2 \partial_x(f_{\alpha-1}) + h f_{\alpha-1}\phi_{\alpha-1/2}\big) + (\partial_{xx} q_{\alpha-3/2})(h^2 f_{\alpha-1}) \\ &+ q_{\alpha+1/2}\big(2N^2 + f_\alpha \phi_\alpha^2 - h\partial_x(f_\alpha \phi_\alpha)\big) \\ &+ (\partial_x q_{\alpha+1/2})\big(h f_\alpha \phi_\alpha + h^2 \partial_x(f_\alpha) + h f_\alpha \phi_{\alpha-1/2}\big) + \partial_{xx} q_{\alpha+1/2}\big(h^2 f_\alpha\big) = 0, \end{aligned} \tag{4.13}$$

where P^* are the independent terms. The system (4.13) is solved numerically by an iterative Jacobi method. In this way we only need to write out the part of the matrix associated with $q_{\alpha-1/2}$. If we denote this matrix by $\boldsymbol{M} = (M_{i,j})$ then

$$\begin{aligned} M_{i,i} = 8N^2 &+ f_\alpha \phi_\alpha^2 + f_{\alpha-1}\phi_{\alpha-1}^2 - h_{i+1/2}\partial_x(f_{\alpha,i+1/2}\phi_{\alpha,i+1/2}) + h_{i+1/2}\partial_x(f_{\alpha-1,i+1/2}\phi_{\alpha-1,i+1/2}) \\ &+ \frac{2}{\Delta x^2} h_{i+1/2}^2 (f_{\alpha,i+1/2} + f_{\alpha-1,i+1/2}), \end{aligned}$$

$$\begin{aligned}
M_{i,i+1} &= -\frac{1}{2\Delta x}\big(h_{i+1/2}\partial_x(f_{\alpha,i+1/2}h_{i+1/2}) + h_{i+1/2}\partial_x(f_{\alpha-1,i+1/2}h_{i+1/2})\big)\\
&\quad - \frac{1}{\Delta x^2}h^2_{i+1/2}(f_{\alpha,i+1/2}+f_{\alpha-1,i+1/2}),\\
M_{i,i-1} &= \frac{1}{2\Delta x}\big(h_{i+1/2}\partial_x(f_{\alpha,i+1/2}h_{i+1/2}) + h_{i+1/2}\partial_x(f_{\alpha-1,i+1/2}h_{i+1/2})\big)\\
&\quad - \frac{1}{\Delta x^2}h^2_{i+1/2}(f_{\alpha,i+1/2}+f_{\alpha-1,i+1/2})
\end{aligned}$$

and $M_{i,j} = 0$ for $|i-j| > 1$. Notice that $\partial_x h = \phi_\alpha - \phi_{\alpha-1}$, where

$$\phi_\alpha = 2N\partial_x\left(z_{\alpha-1/2} + \frac{h_\alpha}{2}\right).$$

As stated before, once the values of $q_{\alpha-3/2}$, $q_{\alpha-1/2}$ and $q_{\alpha+1/2}$ have been found for each layer, we must update the values of u_α and w_α for each layer using (4.10).

1.4.10 Adding viscosity and friction

At this point we have variables evaluated at time step $t_{\nu+1}$ but we must add the viscosity effect, so we will rename this time as $*$ and because we are only correcting the velocity, thereby omitting the superscript in h_α. Thus, we obtain

$$h_\alpha u_\alpha^{\nu+1} = h_\alpha u_\alpha^* + \frac{\Delta t}{\theta_\alpha}K^{\nu+1}_{\alpha-1/2} - \frac{\Delta t}{\theta_\alpha}K^{\nu+1}_{\alpha+1/2}.$$

By using the definition (4.6) we get

$$\begin{aligned}
h_1u_1^{\nu+1} &= h_1u_1^* - \Delta t k_1|h_1u_1^*|h_1u_1^{\nu+1} + \Delta t\frac{\eta_0}{2\theta_\alpha}\frac{u_2^{\nu+1}-u_1^{\nu+1}}{h_1},\\
h_\alpha u_\alpha^{\nu+1} &= h_\alpha u_\alpha^* - \Delta t\frac{\eta_0}{2\theta_\alpha}\frac{u_\alpha^{\nu+1}-u_{\alpha-1}^{\nu+1}}{h_\alpha} + \Delta t\frac{\eta_0}{2\theta_\alpha}\frac{u_{\alpha+1}^{\nu+1}-u_\alpha^{\nu+1}}{h_\alpha}, \quad \alpha = 2,\dots,N-1,\\
h_Nu_N^{\nu+1} &= h_Nu_N^* - \Delta t\frac{\eta_0}{2\theta_\alpha}\frac{u_N^{\nu+1}-u_{N-1}^{\nu+1}}{h_N}.
\end{aligned}$$

For the unknowns $u_1^{\nu+1},\dots,u_N^{\nu+1}$ we obtain the linear system of equations

$$\begin{gathered}
\left(1+\frac{\eta_0\Delta t}{2\theta_\alpha h_1^2} + \Delta t k_1|h_1u_1^*|\right)h_1u_1^{\nu+1} - \frac{\eta_0\Delta t}{2\theta_\alpha h_\alpha^2}h_\alpha u_2^{\nu+1} = h_1u_1^*,\\
\left(1+\frac{\eta_0\Delta t}{\theta_\alpha h_\alpha^2}\right)h_\alpha u_\alpha^{\nu+1} - \frac{\eta_0\Delta t}{2\theta_\alpha h_\alpha^2}h_\alpha u_{\alpha-1}^{\nu+1} - \frac{\eta_0\Delta t}{2\theta_\alpha h_\alpha^2}h_\alpha u_{\alpha+1}^{\nu+1} = h_\alpha u_\alpha^*, \quad \alpha = 2,\dots,N-1,\\
\left(1+\frac{\eta_0\Delta t}{2\theta_\alpha h_N^2}\right)h_Nu_N^{\nu+1} - \frac{\eta_0\Delta t}{2\theta_\alpha h_\alpha^2}h_\alpha u_{N-1}^{\nu+1} = h_Nu_N^*.
\end{gathered}$$

This system has a tridiagonal matrix and is solved by a Thomas algorithm.

Table 1.1: Example 1.1: convergence test (comparison with an exact soliton solution).

Number of cells $\mathcal{J}$	L^1 error e_h	rate	L^1 error e_{hu}	rate	L^1 error e_{hw}	rate
50	1.17E-02	—	3.99E-02	—	1.14E-02	—
100	5.30E-03	1.14	1.78E-02	1.16	6.20E-03	0.88
200	3.00E-03	0.82	1.01E-02	0.82	3.80E-03	0.71
400	1.70E-03	0.82	5.70E-03	0.83	2.20E-03	0.79
800	9.11E-04	0.90	3.00E-03	0.93	1.20E-03	0.87
1600	4.75E-04	0.94	1.60E-03	0.91	6.56E-04	0.87

1.5 Numerical results

1.5.1 Example 1.1: convergence test

As a first test of the accuracy of the scheme we consider the exact soliton solution of the LDNH_0 model, which is described in Appendix A. The computational domain is the x-interval $X = [-25, 25]$, which is subdivided into $\mathcal{J}$ subintervals of length $\Delta x = 50/\mathcal{J}$, and we let $\varphi(x_i, t)$ denote the numerical approximation of the exact value $\varphi_{\text{exact}}(x_i, t)$, where x_i is the $i-$th discrete spatial point in the grid. We measure the L^1 error in φ at simulated time $t = 10\,\mathrm{s}$ as follows:

$$e_\varphi(t) := \frac{1}{\mathcal{J}} \sum_{i=1}^{\mathcal{J}} \bigl|\varphi(x_i, t) - \varphi_{\text{exact}}(x_i, t)\bigr|;$$

this is done for $\varphi = h$, $\varphi = hu$, and $\varphi = hw$. We utilize a CFL number of 0.8 and obtain the errors displayed in Table 1.1. We observe that the error decreases at a rate slightly smaller than one, in agreement with the formal first-order accuracy of the numerical scheme.

1.5.2 Examples 1.2 to 1.6: Iimura-Tanaka experiments and tests for the LDNH_0 single-layer model

The model and numerical method are motivated by a series of experiments reported by Iimura and Tanaka [46] that represents a scale 1:100 scenario for a real-world tsunami. The experimental setup consists in a channel of width 0.4 m and length 15 m with a bottom topography representing a beach (coastal area) with two slopes, see [46, Figure 1] and our Figure 1.4. At the seaward end of the channel, at $x = 0\,\mathrm{m}$, a wave-making plate is located, and between $x = 10.36\,\mathrm{m}$ and $x = 11.36\,\mathrm{m}$ various arrangements of vertical cylinders, each with a diameter of $d = 0.005\,\mathrm{m}$ can be placed to model the coastal vegetation (see Figure 1.5). The level of water

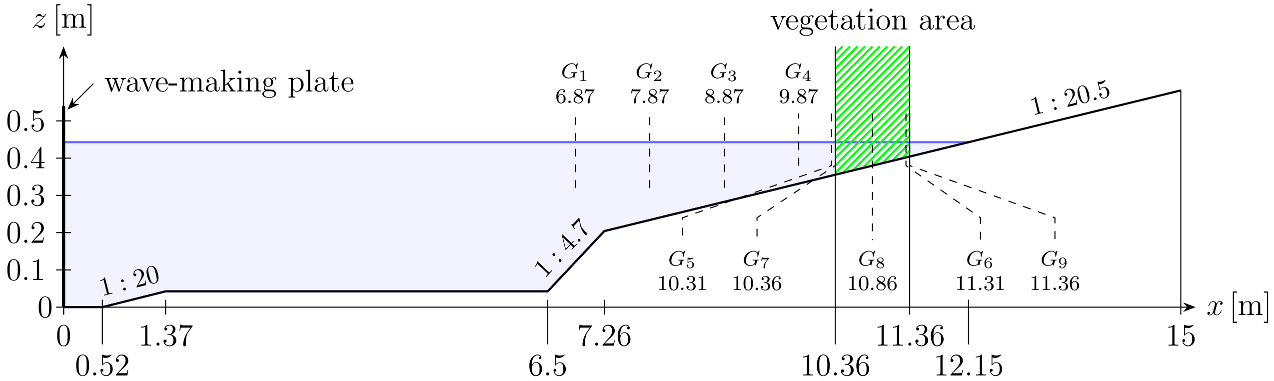

Figure 1.4: Schematic of the experiment, showing the positions of the nine measurement points $G_1, \ldots, G_9$. The positions of G_1 to G_6 are fixed, G_7 and G_8 are in front of and behind the vegetation, and G_8 is in the middle of the vegetation for uniform arrangements (in this study, Cases 1, 3 and 5 of [46]) and at the boundary of two different tree densities in the combined arrangements (in this work, Cases 8 and 13 of [46]). The specific situation in this plot with $G_7 = 10.36\,\mathrm{m}$, $G_8 = 10.36\,\mathrm{m}$ and $G_9 = 11.36\,\mathrm{m}$ corresponds to Case 1. Notice that the vertical scale is five times larger than the horizontal.

at rest is 0.4 m. The run-up height, water level, and force acting on a cylinder were measured at nine different points ($G_1, \ldots, G_9$; see Figure 1.4 for the corresponding x-positions).

Among the 15 different distributions of coastal vegetation tested in [46], Cases 1 to 15, we used five, namely Cases 1, 3, 5, 8, and 13, for numerical simulation. To specify the corresponding parameters, we recall from [46] that for given a tree distribution such as the one drawn in Figure 1.5, the thickness of vegetation is calculated as

$$d_n = \frac{2}{\sqrt{3}D_\mathrm{f}^2} W_\mathrm{f} d \times 10^5 + \frac{2}{\sqrt{3}D_\mathrm{b}^2} W_\mathrm{b} d \times 10^5, \tag{5.1}$$

where the factor 10^5 adjusts a unit of d_n because D and W are measured in millimeters and d in meters. In the experiments, d_n was set to a constant 231 in all experiments [46]. The width of the channel is 0.4 m; then, the tree density, measured in trees per square metre, can be calculated as

$$n_\mathrm{t} = \frac{d_n}{W \times 0.4\,\mathrm{m}}.$$

The wave-making plate at $x = 0\,\mathrm{m}$ generates a solitary wave with a height of 3.14 cm in the vicinity of the left boundary.

The parameters defining the five cases considered herein are summarized in Table 1.2. The drag coefficient C_D is defined as a function of x obtained by piecewise linear interpolation of values of C_D specified at x_7, x_8, and x_9, or at $x_{8,\mathrm{f}}$ and $x_{8,\mathrm{b}}$ instead of x_8 in the case that the "front" and "back" limiting values of C_D differ (see Figure 1.5).

On the other hand, in [44], the authors analyse and compare of different approaches for describing and generating solitary waves by plates in a flume. We found that the profile that

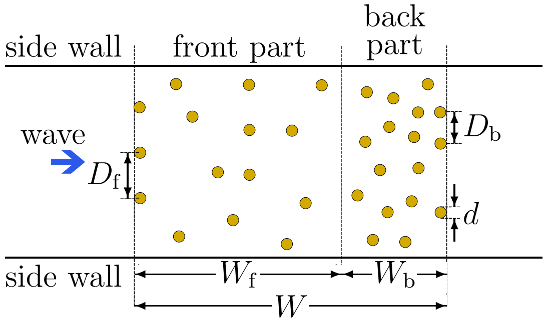

Figure 1.5: Schematic of the distribution of trees in the experiment, as seen from above. The (model) forest in flow direction has the total length W, and is subdivided into a front part and a back part of lengths W_f and W_b, respectively. These parts may be equipped with different models of vegetation.

best matched the initial condition was the solution found by Rayleigh [66] that is given by

$$\eta(x,0) = \eta_0 \mathrm{sech}^2(\beta x) \quad \text{with} \quad \beta = \sqrt{\frac{3\eta_0}{4h_0^2(h_0+\eta_0)}}, \tag{5.2}$$

where η_0 is the wave amplitude and h_0 height of water. This means that the initial wave velocity is

$$u(x,0) = c\frac{\eta(x,0)}{h(x,0)} \quad \text{with} \quad c = \sqrt{g(h_0+\eta_0)}.$$

In order to fit the wave into the channel we slightly extend the computational domain to $x < 0$.

In addition to the experimental data we include in Figure 1.6 numerical simulations of the maximal water level. All numerical simulations for Examples 1.2 to 1.6 have been obtained with $\Delta x = 0.02\,\mathrm{m}$ and are based on a CFL number of 0.8. The simulations of Examples 1.2 to 1.6 in Figure 1.6 have been obtained by the LDNH$_0$. For Case 3 of [46] (our Example 1.3) we also display in Figure 1.8 (b) the simulated water height at $x = x_9 = 11.36\,\mathrm{m}$, the position of G_9, as a function of time. Furthermore, Figure 1.7 illustrates the temporal evolution of the water surface elevation for selected test cases, where the three-dimensional representation (x, t, z) highlights the propagation and interaction of the free-surface dynamics over time.

1.5.3 Examples 1.7 to 1.8: Iimura-Tanaka experiment and LDNH$_0$ multi-layer tests.

Having calibrated the model using the experimental data, we are now ready to simulate diverse scenarios that account for trees with properties that vary along the vertical axis. We use the same initial condition as for Examples 1.2 to 1.6. All simulations employ the same initial condition for the water waves, namely the one given by (5.2).

Table 1.2: Parameters and drag coefficients for Cases 1, 3, 5, 8, and 13 from Iimura and Tanaka [46]. The table includes tree spacing, forest length, drag coefficient values, and tree densities for each case. Examples 1.2 to 1.6 correspond to the simulations in Figure 1.6.

Parameter	Example 1.2 Case 1	Example 1.3 Case 3	Example 1.4 Case 5	Example 1.5 Case 8	Example 1.6 Case 13
D_b [mm]	50	30	10	40	20
D_f [mm]	0	0	0	20	40
W_b [mm]	0	360	40	320	80
W_f [mm]	1000	0	0	80	320
x_F [m]	10.32	11.00	11.32	10.96	10.96
$C_\mathrm{D}(x_7)$	0.71	0.66	1.73	0.83	0.76
$C_\mathrm{D}(x_{8,\mathrm{f}})$	0.94	0.79	1.32	1.07	0.76
$C_\mathrm{D}(x_{8,\mathrm{b}})$	0.94	0.79	1.32	0.84	0.92
$C_\mathrm{D}(x_9)$	0.77	0.94	2.23	0.74	1.26
n_t [m^{-2}]	577.5	1604.16	14437.5	$n_{\mathrm{t,f}} = 3609.4$ $n_{\mathrm{t,b}} = 902.3$	$n_{\mathrm{t,f}} = 902.3$ $n_{\mathrm{t,b}} = 3609.4$

Now the vegetation parameters depend on height z. Equation (5.1) is replaced by

$$d_{n,\alpha} = \frac{2}{\sqrt{3}D_\mathrm{f}^2} W_\mathrm{f} \bar{d}_\alpha \times 10^5 + \frac{2}{\sqrt{3}D_\mathrm{b}^2} W_\mathrm{b} \bar{d}_\alpha \times 10^5, \quad \alpha = 1, \dots, N,$$

that is we assume that d_n is specific for each layer α. The average tree diameter $\bar{d}_\alpha$ is defined in (4.5). On the other hand, D_f and D_b are calculated from the centers of the trees and we assume trees have layer-wise cylindrical symmetry so they do not change with respect to ζ. Likewise, W_f and W_b do not depend on ζ or z either. Furthermore, to include the effects of branches and leaves given by $c_\mathrm{tr}(\zeta)c_\mathrm{le}(\zeta)$ (see Section 1.4.5) one usually defines $d_{n,\mathrm{all}} := d_n \times c_\mathrm{tr}c_\mathrm{le}$. For the multilayer model we generalize this as

$$d_{n,\mathrm{all},\alpha} = d_{n,\alpha} \times (\overline{c_\mathrm{tr}c_\mathrm{le}})_\alpha, \quad \alpha = 1, \dots, N.$$

Next, we investigate the impact of varying tree heights. In Example 1.7 we assume that the trees have a height of 0.03 m (measured from ground). This information is incorporated by setting

$$d(\zeta) = \begin{cases} 0.03\,\mathrm{m} & \text{for } \zeta < 0.03\,\mathrm{m}, \\ 0\,\mathrm{m} & \text{for } \zeta \geq 0.03\,\mathrm{m}. \end{cases}$$

In this case differences in the numerical solution in dependence of the number of layers do become visible in the forest areas (Example 1.7, see Figure 1.9 (a)).

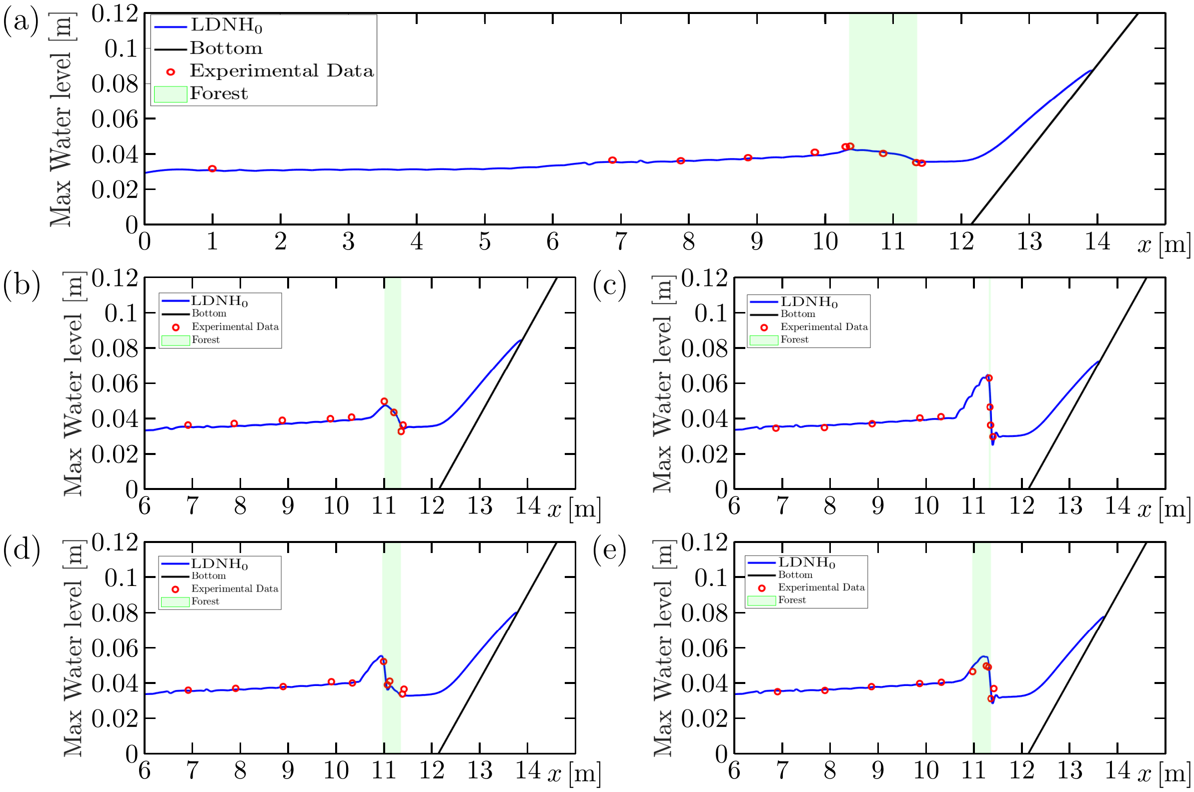

Figure 1.6: Examples 1.2 to 1.6: experimental data (red dots) and LDNH$_0$ simulations for (a) Example 1.2 [46, Case 1], (b) Example 1.3 [46, Case 3], (c) Example 1.4 [46, Case 5], (d) Example 1.5 [46, Case 8] and (e) Example 1.6 [46, Case 13].

Finally, Example 1.8 (see Figure 1.9 (b)) shows how the water level, simulated with $N = 10$ layers, depends on the height of trees that varies between 0 m (no vegetation at all) to the unlimited case. Note that the numerical solutions corresponding to each of the seven cases are ordered consistently, and that while the cases with no vegetation or small tree height cause slightly higher water levels around $t = 7$ s, the returning wave produces a marked extremum around $t = 13$ s for the unlimited tree height or when the tree height is 0.05 m or 0.04 m. This property alerts to the accumulation of water behind the forest when the wave returns.

1.5.4 Examples 1.9 to 1.13: simulations with height-dependent tree properties

As the case of Example 1.7 showed, utilizing a multilayer scheme instead of a single-layer approach does not produce significantly new results when the vegetation is vertically homogeneous. However, when the vegetation has properties that strongly vary with height then results significantly depend on the number of layers. To illustrate this point we consider a vegetation

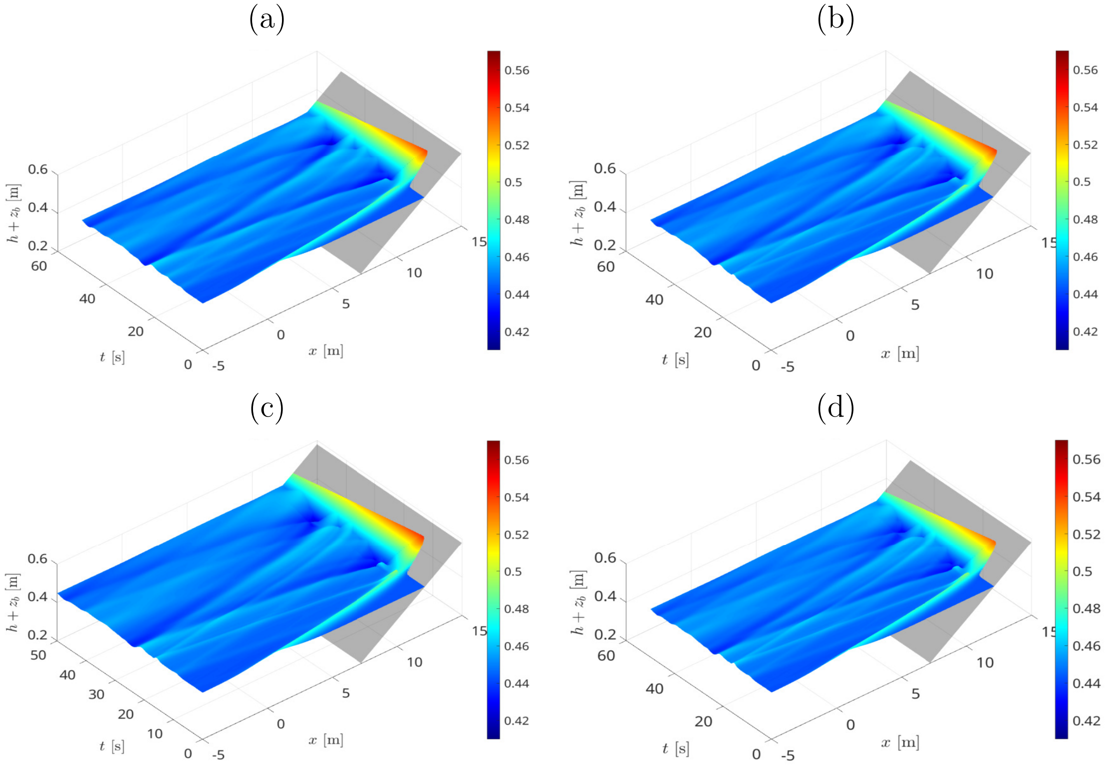

Figure 1.7: Numerical simulations of (a) Case 1, (b) Case 3, (c) Case 5 and (d) Case 13.

area of trees for which the parameter $c_{\mathrm{tr}}c_{\mathrm{le}}$ (see Section 1.4.5) varies with height. To this end we fit a polynomial to the experimental data.

We utilize information by Tanaka et al. [70] who estimated the product $(c_{\mathrm{tr}}c_{\mathrm{le}})(\zeta)$ for a number of tree species that are representative of the coastal vegetation affected by the Indian Ocean tsunami of 26 December 2004. (Here ζ denotes height along one tree measured from the ground.) Two of these species, *Pandanus odoratissumus*, a representative tree that grows in beach sand, and *Anarcadium occidentale*, a plantation species in the coastal zone of Sri Lanka and the Andaman coast of Thailand, are selected here because their properties change appreciably along the vertical axis (see [70] for detailed information). Figure 9 of [70] displays empirical information on the vertical distribution of $c_{\mathrm{tr}}c_{\mathrm{le}}$ for these (and other) species. We have used this information, scaled by 1/100, to provide this function in both cases after fitting the measured values to a polynomial of suitable degree (Figure 1.10).

Examples 1.9 and 1.10 are based on [46, Case 3], as are Examples 1.2, 1.7, and 1.8, but we now utilize tree properties that depend on height as described by the function $(c_{\mathrm{tr}}c_{\mathrm{le}})(\zeta)$ corresponding to *P. Odoratissimus*. Figure 1.11 (a) displays the differences in the numerical solution coming from the use of various numbers of layers N. The results obtained by $N = 1$ layer and more layers are almost indistinguishable. The likely reason for this behaviour is that the amplitude of the soliton is too small to produce appreciable vertical changes. In Figure 1.11 (b) we simulate the same scenario but this time the soliton has an amplitude of

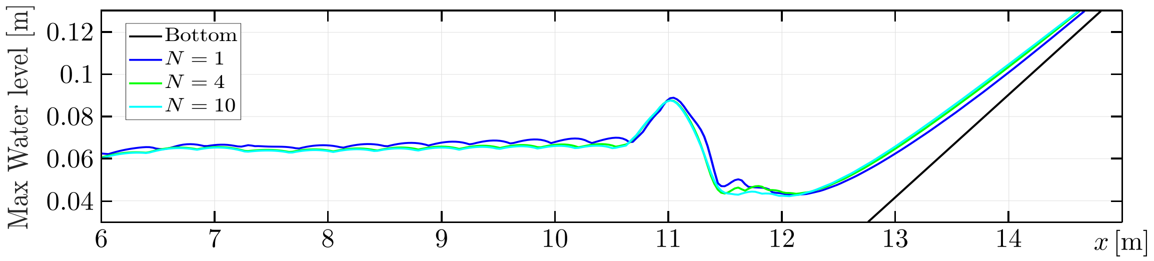

Figure 1.8: Examples 1.2 to 1.6: (a) initial condition of the simulation, (b) Example 3 [46, Case 3]: temporal evolution at $x = 11.36\,\mathrm{m}$ compared with experimental data.

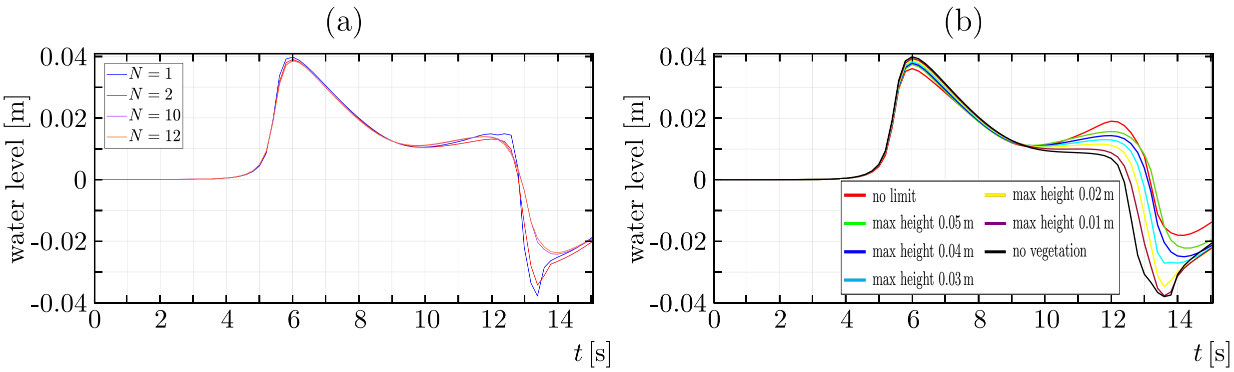

Figure 1.9: Examples 1.7 and 1.8: simulated water levels at $x = 11.36\,\mathrm{m}$ for variants of [46, Case 3]: (a) Example 1.7: result for maximum tree height 0.03 m, (b) Example 8: water levels for various maximum heights of vegetation for $N = 10$ layers.

$h_0 = 0.0628\,\mathrm{m}$, that is the double of the original test. This time we obtain significant differences between the single-layer and the multi-layer model. In particular, $N = 4$ layers provide a satisfactory level of precision while also being significantly less computationally demanding compared to the model with $N = 10$ layers. In general results with more than four layers are almost identical. This observation is supported by Figure 1.12 where we consider again Example 11 but now measure the maximal water level for various values of N.

Results are slightly different if instead of *P. Odoratissimus* we consider the species *A. Occidentale*, for which significant differences are observed between using a single layer and multiple layers, as depicted in Figures 1.13 (a) and (b). The model with only one layer tends to overestimate the maximum wave height while underestimating the minimum water level. However, it is notable that using four layers once again proves to be sufficient in accurately modeling the situation. For Example 1.13 we also plot (in Figure 1.14) the simulated maximum water level for various numbers of layers. In particular in the vegetation zone (enlarged area) differences between models with one layer and two or more layers become significant.

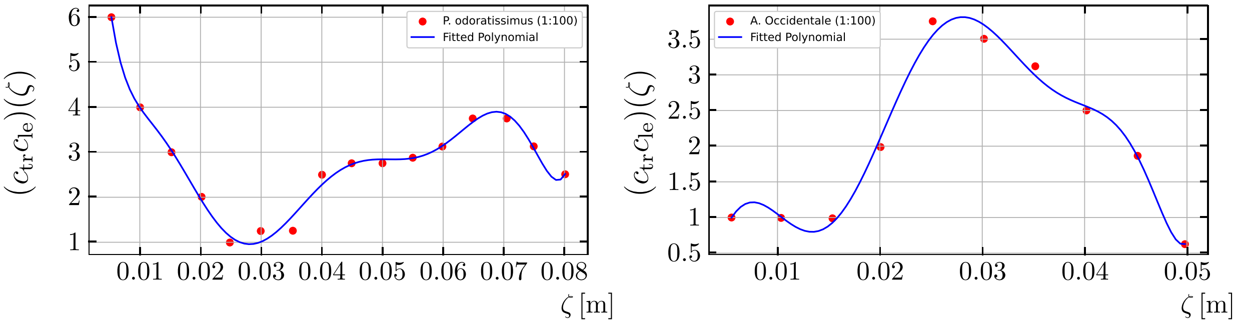
(a)

(b)

Figure 1.10: Examples 1.9 to 1.13: approximation of experimental information from [70] on $(c_{\mathrm{tr}}c_{\mathrm{le}})(\zeta)$, scaled to 1/100, by fitting polynomials of degree 8 to data of (a) *P. Odoratissimus*, (b) *A. Occidentale*. Note that ζ measures height along one tree from ground.

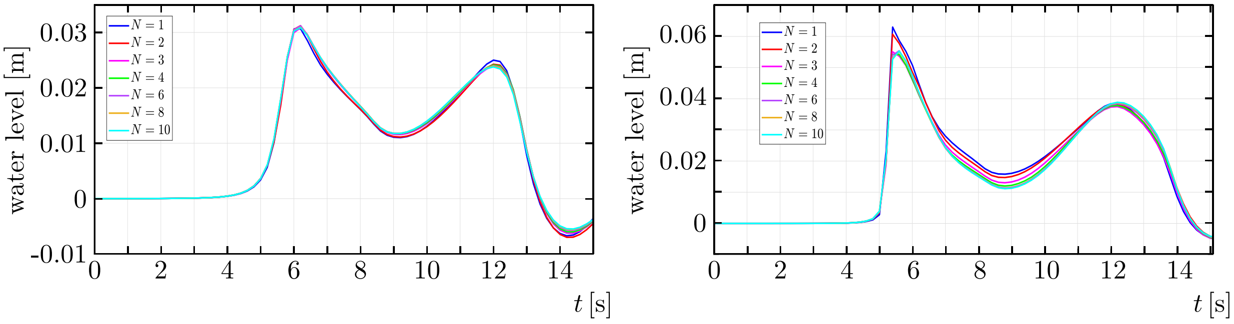
(a)

(b)

Figure 1.11: Examples 1.9 and 1.10: simulated water levels observed at $x = 11.36\,\mathrm{m}$ with $(c_{\mathrm{tr}}c_{\mathrm{le}})(\zeta)$ corresponding to *P. Odoratissimus*, trees of height 0.08 m, and various numbers of layers N: (a) with a soliton amplitude $h_0 = 0.0314\,\mathrm{m}$ (Example 1.11), (a) with a soliton amplitude $h_0 = 0.0628\,\mathrm{m}$ (Example 1.12).

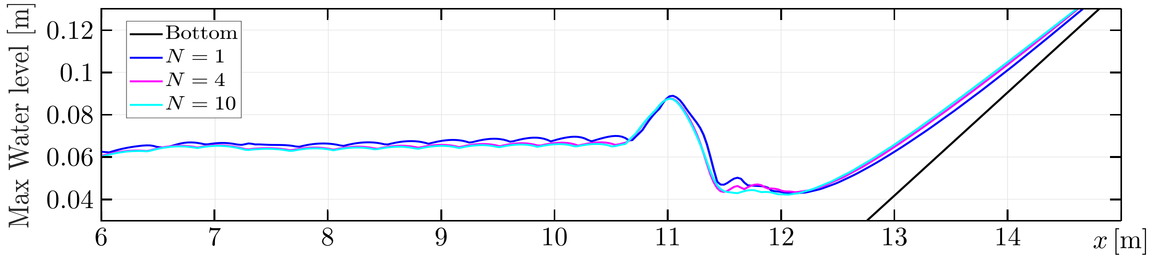

Figure 1.12: Example 1.11: maximum water levels for various numbers of layers N.

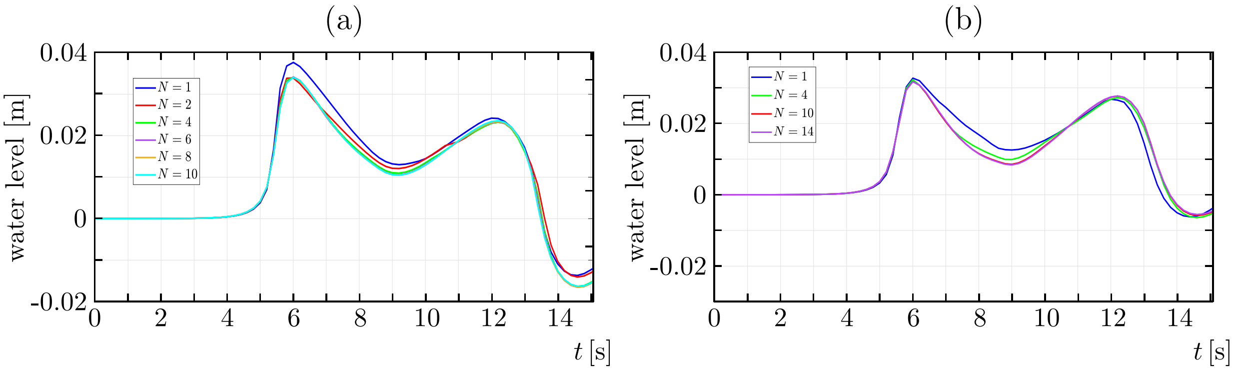

Figure 1.13: Examples 1.12 and 1.13: simulated water levels measured at $x = 11.36\,\text{m}$ for various numbers of layers for a vegetation of *A. Occidentale* with a tree height of 0.05 m and a distribution of vegetation according to (a) [46, Case 3] (Example 1.12), (b) [46, Case 13] (Example 1.13).

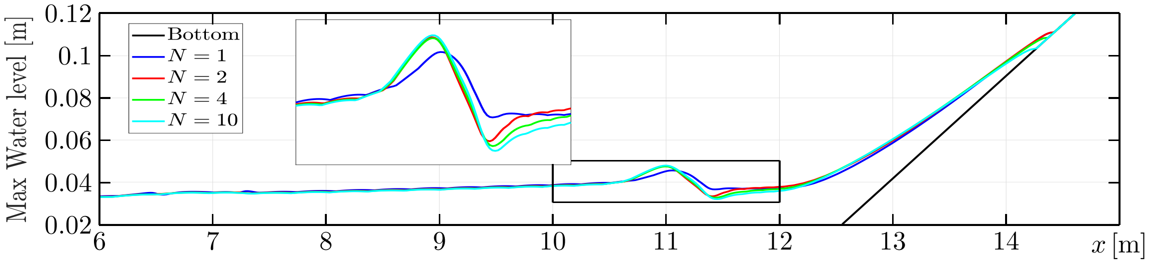

Figure 1.14: Example 1.13: maximum water levels for various numbers of layers for a vegetation of *A. Occidentale* with a tree height of 0.05 m and a distribution of vegetation according to [46, Case 3], inserted: enlarged view of marked area.

CHAPTER 2

Well-balanced physics-based methods for sediment transport models

2.1 Introduction

2.1.1 Scope

The dynamics of sediment transport is determined by the interplay between bedload, erosion, and deposition processes. While bedload involves the transport of sediment particles captured in an erodible bottom, erosion refers to the entrainment of sediment into the fluid, and deposition occurs when sediment particles settle back onto the bed. These processes affect sediment transport rates, which in turn influence river morphology and sediment distribution. Accurate modelling of these processes requires the formulation of appropriate deposition rates, settling velocities, and sediment entrainment factors. The Saint-Venant-Exner (SVE) system is widely used to describe bedload sediment transport. It combines the Saint-Venant (or shallow water) system for hydrodynamics with a continuity equation (the Exner equation) to model the bed evolution. Furthermore, erosion and deposition are commonly described by empirical formulas.

The Exner equation [30] defines sediment transport in terms of the solid transport discharge, which requires specifying a model closure. For this purpose, several empirical models have been introduced, although they often lack dissipative energy properties and/or violate mass conservation. Moreover, many of these models are only validated for nearly horizontal sediment beds, which is also a major limitation. Several SVE-type models have been formulated in terms of the closure of the solid transport discharge.

Equilibrium models are based on the hypothesis that erosion and deposition rates between moving and static particles of the sediment bed are equal. From this assumption, an approximation of the thickness of moving particles in the bed is deduced. In general, it is defined as a linear formula depending on the difference between the Shields parameter and the critical Shields parameter. Bagnold [10] deduced this linear relation from experimental laboratory data. Some examples of models using this approach are the ones introduced by Meyer-Peter and Müller [53], Ashida-Mishiue [3], Fernández-Luque and Van Beek [50], Nielsen [54] or Ribberink [58], among others.

This hypothesis does not hold, for instance, when the sediment evolves over a non-erodible bed. There, one may obtain a gain or loss of sediment mass. This lack of sediment mass conservation does not occur in the case of non-equilibrium models, where the thickness of the moving particles in the bed is a model unknown (see e.g. [23, 37, 51]). Nevertheless, these non-equilibrium models are defined, in general, under the assumption of a small bottom slope and do not account for gravitational effects.

Furthermore, they do not consider a modification of the friction law in the momentum equation of the fluid. Actually, when considering just a classical friction formula in the momentum equation, such as Manning's law, the model does not satisfy a dissipative energy balance. Notice that classical laws are deduced for fixed bottom, so they only depend on the velocity of the fluid. However, in order to obtain a model with a dissipative energy balance, a friction law in terms of the relative velocity between the fluid and the sediment bed layer must be considered.

Fernández-Nieto *et al.* [35] formally deduced SVE models from an asymptotic analysis of a coupled system with the shallow water system and a Reynolds equation. The proposed models include several versions with equilibrium and non-equilibrium assumptions. These models satisfy a dissipative energy balance. Moreover, two corrections for classical models are proposed: first, gravitational effects are incorporated through a novel definition of the effective Shields parameter; second, the friction is defined in terms of the difference between the fluid and sediment velocities. The latter correction is a key point to obtain a model with a dissipative energy balance.

In [40], a specific semi-implicit numerical method for the model introduced in [35] in equilibrium conditions is introduced. That method is designed for subcritical flows. The difficulty relies in the non-linear degenerate parabolic behaviour of the gravitational terms in the solid transport discharge. To overcome this difficulty, a particular formulation of the solid transport discharge suitable for the application of a semi-implicit numerical discretization is introduced in [40]. This formulation will be used here.

Shallow water systems, which usually form the hydrodynamic part of sediment transport models, are typically based on a hydrostatic framework for the fluid, which means that vertical acceleration and dispersive effects are neglected. Nevertheless, non-hydrostatic pressure may strongly influence the fluid dynamics, as it is shown in several studies of depth-averaged models (see e.g. [11, 65, 74, 75] and references cited in these works). Roughly speaking, these models form two big families, namely Boussinesq-type and non-hydrostatic models, although many of them may be rewritten in both formulations (see [29]). The main difference is that dispersive Boussinesq-type models introduce high-order derivatives to account for dispersive effects, whereas the so-called non-hydrostatic models incorporate new unknowns and additional equations. This property simplifies the numerical approximation since only first-order derivatives appear (see e.g. [36, 67, 76]).

Numerical approximations of SVE-type models formulated as hyperbolic systems of first-order partial differential equations are usually based on finite volume (FV) methods. In the context of geophysical flows, these systems frequently include non-conservative products, which complicate the application of standard FV schemes. A widely studied problem of this kind is the incorporation of an erodible or fixed bottom into the shallow water equations. A well-known class of FV schemes that properly handle non-conservative products are the so-called path-conservative schemes [22, 57, 73]. These schemes have been successfully applied to hyperbolic systems with non-conservative products in many applications, including multilayer shallow water systems, compressible gas dynamics, or magnetohydrodynamics. Furthermore, Parés and Castro [55] proposed a generalization of the Roe method (see also [73]). However, its implementation requires explicit knowledge of the eigenstructure of the intermediate matrices. To overcome this limitation, Castro and Fernández-Nieto [28] introduced a specific family of path-conservative schemes, named polynomial viscosity matrix (PVM) methods, which extend many FV schemes based on incomplete Riemann solvers such as the Lax-Friedrichs scheme, the Rusanov scheme (also called local Lax-Friedrichs (LLF) scheme, [48]) and the Harten-Lax-van Leer (HLL) scheme [45]. One of the difficulties of designing such schemes is related to the well-balance property, which refers to the ability of the scheme to preserve certain stationary solutions, in particular, the steady at rest (or water at rest) solutions, i.e., flat free surface and zero velocity. For a fixed bottom, numerous schemes are well-balanced. However, if one of these schemes (that are well-balanced for a fixed bottom) is used to solve the SVE equations then its steady solutions will not be preserved in many cases, even in the case of no fluid velocity and zero solid transport discharge, because the bed sediment will move continuously. This unphysical behaviour comes from uncontrolled numerical diffusion in the discretization of the bed evolution equation within the SVE model; this problem does not arise in the case of a fixed bottom (see [49]).

In this work, we introduce a modified SVE-type model that is deduced from a general model with density variation and a Boussinesq-type assumption to account for all these effects. Specifically, the model includes a non-hydrostatic pressure for the fluid layer, gravitational effects, and sediment in suspension. Each of these effects can be activated or deactivated as needed. Furthermore, a general formulation for the solid transport discharge in the sediment layer makes it possible to formulate this simplified model in equilibrium (erosion rate equals deposition rate) or non-equilibrium conditions. Moreover, an energy balance implies that under appropriate boundary conditions, the contributions of energy are controlled by dominantly dissipative mechanisms. Another contribution is a novel time-dependent semi-analytical solution for the non-equilibrium model used to validate the methods proposed. The principal novelty, however, are two new techniques to achieve the well-balance property of schemes for the general SVE-type model: firstly, a physically motivated correction of the numerical diffusion term for Rusanov and HLL schemes; and secondly a scheme denoted here by PVM-2I, which coincides with the HLL scheme for the flow variables but modifies the numerical approximation of the bed evolution equation according to its related characteristic speed. To our knowledge, no technique in the literature has been presented that would be well-balanced for Rusanov and HLL-type methods for SVE models. As mentioned, Rusanov and HLL methods can be expressed as PVM methods involving constant and linear polynomials of the system matrix. An advantage of these methods is their preservation of the positivity of the water depth (see [12]). On the contrary, PVM methods including a second-order term, which includes a square of the system matrix, present challenges in proving positivity. As a consequence, the well-balanced Rusanov and HLL methods proposed in this paper are excellent candidates to be considered as basal schemes for the development on high-order well-balanced FV method based on reconstructed states. Gravitational terms are discretized by following the approach of [40] not only in subcritical flows but also in supercritical regimes.

2.1.2 Outline of the chapter

The remainder of this chapter is organized as follows. Section 2.2 is dedicated to the derivation and definition of the model, along with the analysis of its key properties. The proposed model describes bedload transport and the interaction between fluid and sediment through the processes of erosion and deposition of suspended particles. First, in Section 2.2.1 the balance equations are formulated. These describe conservation of mass and linear momentum, sediment transport, and bed evolution. The resulting balance equations are supplemented by an incompressibility condition. In Section 2.2.2 the bedload flux is defined for several cases including non-equilibrium and equilibrium models with and without gravitational effects. Bedload discharge represents the quantity of sediment particles transported along the riverbed or channel per unit time. Next, in Section 2.2.3 we verify that the model complies with mass conservation. Then, in Section 2.2.4 we demonstrate that the total mechanical energy of the model satisfies a dissipative energy balance. Section 2.3 focuses on the numerical approximation of the model, including the treatment of source terms coming form the erosion and deposition rates, non-hydrostatic pressure, and gravitational effects. To this end, we introduce in Section 2.3.1 some preliminaries and outline in Section 2.3.2 the finite volume method for the governing hyperbolic system with non-conservative products. The main contributions of this paper are in Sections 2.3.3 and 2.3.4 where the well-balanced corrections for Rusanov and HLL methods, and the new PVM-2I method, are presented. Furthermore, in Section 2.3.5 we introduce a semi-implicit numerical scheme to handle gravitational terms that influence the vertical motion of particles, particularly their settling and redistribution. The semi-implicit treatment enhances stability while maintaining computational efficiency. Next, in Section 2.3.6 we deal with the source terms related to erosion and deposition, and conclude the formulation of the scheme with description of the projection method to handle the non-hydrostatic pressure (Section 2.3.7). Section 2.4 is devoted to the numerical tests. We validate our numerical schemes through a series of test cases, including semi-analytical solutions, academic test, and comparisons with experimental data. Here, various simplified cases are considered, such as the

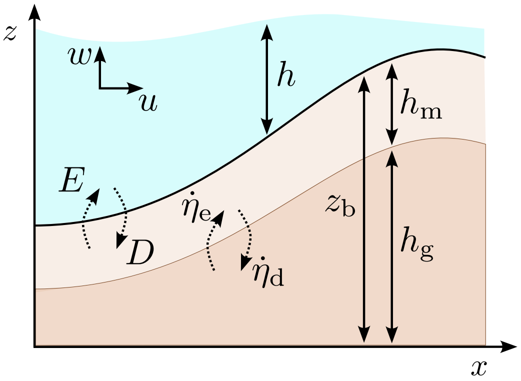

Figure 2.1: Schematic representation of the proposed model, illustrating key variables such as the water depth h and the height of the erodible bed z_{b}, composed of an active layer h_{m} and a fixed layer h_{g}, see Table 2.1.

case to consider or not sediment in suspension, equilibrium and non-equilibrium models and the influence of gravitational effects. In particular, we illustrate the well-balancedness of the proposed method and the accuracy of the PVM-2I scheme with respect to the Rusanov and HLL methods due to the reduction of numerical diffusion for the bed evolution equation.

2.2 Model of sediment transport with suspended particles

The framework of the sediment transport model is sketched in Figure 2.1. A central feature of the model is the inclusion of the so-called active layer, which refers to the uppermost portion of the erodible bed that directly interacts with the overlying flow. This layer is characterized by the continuous exchange of sediment particles via entrainment and deposition. This process plays a crucial role in controlling the short-term dynamics of sediment transport. Typically, the active layer has a finite thickness and consists of grains that are more mobile than those in the underlying layer [35].

2.2.1 Balance equations

In Table 2.1 we indicate the variables that are used. With these definitions, the governing equations in the non-hydrostatic case are given by

$$\partial_t(h\rho) + \partial_x(h\rho u) = \rho_0 \frac{E-D}{1-\psi_0}, \tag{2.1}$$

$$\partial_t(h\rho u) + \partial_x\left(h\rho u^2 + \frac{1}{2}gh^2\rho + h\hat{p}_{\mathrm{nh}}\right) = -(\rho g h + 2\hat{p}_{\mathrm{nh}})\partial_x z_{\mathrm{b}} - \tau + \frac{u}{2}\rho_0\frac{E-D}{1-\psi_0}, \tag{2.2}$$

$$\partial_t(h\rho w) + \partial_x(h\rho u w) = 2\hat{p}_{\mathrm{nh}} + \frac{w}{2}\rho_0\frac{E-D}{1-\psi_0}, \tag{2.3}$$

Table 2.1: Definition of key variables associated to Figure 2.1.

Symbol	Description
h	water depth
u, w	horizontal and vertical velocities
c	sediment concentration
z_{b}	position of erodible bed
h_{g}	fixed bed level
E, D	sediment erosion (E) and deposition (D) rates
$\dot{\eta}_{\mathrm{e}}, \dot{\eta}_{\mathrm{d}}$	entrainment and deposition velocities
ρ_{f}	density of fluid
ρ_{s}	density of sediment
ψ_0	porosity
$r_{\mathrm{s}} = \rho_{\mathrm{s}}/\rho_{\mathrm{f}}$	sediment-fluid density ratio
$\rho_0 = \psi_0\rho_{\mathrm{f}} + (1-\psi_0)\rho_{\mathrm{s}}$	bulk density of the mixture
$\rho = c\rho_{\mathrm{s}} + (1-c)\rho_{\mathrm{f}}$	mixture density
$\hat{p}_{\mathrm{nh}}$	non-hydrostatic pressure
p_{nh}	$\hat{p}_{\mathrm{nh}}/\rho$
τ	friction law (Manning or Darcy-Weisbach)

$$\partial_t(hc) + \partial_x(huc) = E - D, \tag{2.4}$$

$$\partial_t z_{\mathrm{b}} + \frac{1}{1-\psi_0}\partial_x q_{\mathrm{b}} = -\frac{E-D}{1-\psi_0}, \tag{2.5}$$

$$\partial_t h_{\mathrm{g}} = -(\dot{\eta}_{\mathrm{e}} - \dot{\eta}_{\mathrm{d}}). \tag{2.6}$$

The specific definitions of E, D, $\dot{\eta}_{\mathrm{e}}$, and $\dot{\eta}_{\mathrm{d}}$ are provided in Section 2.2.2. The quantity τ is introduced in Section 2.2.4. Equations (2.1)–(2.4) describe conservation of mass and momentum, (2.5) models sediment transport, and (2.6) describes bed evolution. The last terms on the right-hand side of (2.2) and (2.3) describe the transfer of linear momentum between the fluid and sediment layers where the choice of the coefficients $u/2$ and $w/2$ ensures cancellation of the transfer terms between fluid and sediment layers in the energy balance. Equations (2.1) to (2.6) are supplemented by the incompressibility condition

$$w - u\partial_x z_{\mathrm{b}} + \partial_t z_{\mathrm{b}} + \frac{h}{2}\partial_x u = 0.$$

The system (2.1)–(2.3) may be rewritten in terms of the unknowns h, hu, and hw. First, combining (2.1) and (2.4), we get

$$\partial_t h + \partial_x(hu) = \frac{E-D}{1-\psi_0}.$$

Using this equation we obtain the momentum balance equations for hu and hw

$$\begin{aligned}\partial_t(hu)+\partial_x(hu^2)+gh\partial_x(h+z_{\mathrm{b}})+\frac{1}{\rho}\frac{gh^2}{2}\partial_x\rho+\frac{1}{\rho}\partial_x(h\hat{p}_{\mathrm{nh}})&\\ =-2\frac{\hat{p}_{\mathrm{nh}}}{\rho}\partial_x z_{\mathrm{b}}-\tau+\left(1-\frac{\rho_0}{2\rho}\right)u\frac{E-D}{1-\psi_0}&,\\ \partial_t(hw)+\partial_x(huw)=2\frac{\hat{p}_{\mathrm{nh}}}{\rho}+\left(1-\frac{\rho_0}{2\rho}\right)w\frac{E-D}{1-\psi_0}&.\end{aligned}$$

At this point, we make two assumptions to obtain a simplified model with a dissipative energy balance: firstly, we assume that the fluid and sediment densities are very close at the fluid/sediment interface. In fact, if the fluid density tends to the saturation density, then ρ may be approximated by ρ_0 in the transfer terms, which yields

$$1-\frac{\rho_0}{2\rho}\approx\frac{1}{2}.$$

Secondly, in the case of low concentrations, the Boussinesq assumption is justified. Then $\rho\approx\rho_{\mathrm{f}}$ in all terms except for the term representing the deviation from a hydrostatic pressure $\partial_x\rho$. Consequently, we obtain

$$\frac{1}{\rho}g\frac{h^2}{2}\partial_x\rho\approx\frac{1}{\rho_{\mathrm{f}}}g\frac{h^2}{2}\partial_x\rho=(r_{\mathrm{s}}-1)g\frac{h^2}{2}\partial_x c=(r_{\mathrm{s}}-1)\frac{g}{2}\left(h\partial_x(hc)-hc\partial_x h\right).$$

On the other hand, using the mixture density $\rho=\rho_{\mathrm{s}}c+\rho_{\mathrm{f}}(1-c)$ and combining equations (2.1) and (2.4), we may write the mixture mass balance as

$$\begin{aligned}\rho_0\frac{E-D}{1-\psi_0}&=\partial_t(h\rho)+\partial_x(h\rho u)=\rho_{\mathrm{f}}\big(\partial_t((1-c)h)+\partial_x((1-c)hu)\big)+\rho_{\mathrm{s}}\big(\partial_t(hc)+\partial_x(huc)\big)\\ &=\rho_{\mathrm{f}}\big(\partial_t((1-c)h)+\partial_x((1-c)hu)\big)+\rho_{\mathrm{s}}(E-D).\end{aligned}$$

Expanding the last equality yields

$$\begin{aligned}&\rho_{\mathrm{f}}\big(\partial_t h+\partial_x(hu)\big)-\rho_{\mathrm{f}}\big(\partial_t(hc)+\partial_x(huc)\big)+\rho_{\mathrm{s}}(E-D)\\ &=\rho_{\mathrm{f}}\big(\partial_t h+\partial_x(hu)\big)+(\rho_{\mathrm{s}}-\rho_{\mathrm{f}})(E-D).\end{aligned}$$

Finally, replacing the expression from (2.1) for the right-hand side, we obtain

$$\partial_t h+\partial_x(hu)=\frac{1}{\rho_{\mathrm{f}}}\frac{E-D}{1-\psi_0}\big(\rho_0+(\rho_{\mathrm{f}}-\rho_{\mathrm{s}})(1-\psi_0)\big)=\frac{E-D}{1-\psi_0}.$$

Analogously, for the horizontal momentum conservation equation, we write

$$\partial_t(h\rho u)+\partial_x(h\rho u^2)=\rho\big(\partial_t(hu)+\partial_x(hu^2)\big)+u\big(\partial_t(h\rho)+\partial_x(h\rho u)\big)-u\rho\big(\partial_t h+\partial_x(hu)\big),$$

and similarly for the vertical momentum equation (2.3). Then, using the previously derived continuity equation and dividing by ρ, we get the final simplified model

$$\begin{aligned}
&\partial_t h + \partial_x(hu) = \frac{E-D}{1-\psi_0},\\
&\partial_t(hu) + \partial_x\left(hu^2 + \frac{gh^2}{2} + hp_{\mathrm{nh}}\right) + (r_{\mathrm{s}}-1)\frac{g}{2}\left(h\partial_x(hc) - hc\,\partial_x h\right)\\
&\qquad\qquad\qquad\qquad = -(2p_{\mathrm{nh}} + gh)\partial_x z_{\mathrm{b}} - \frac{\hat{\tau}}{\rho_{\mathrm{f}}} + \frac{u}{2}\frac{E-D}{1-\psi_0},\\
&\partial_t(hw) + \partial_x(huw) = 2p_{\mathrm{nh}} + \frac{w}{2}\frac{E-D}{1-\psi_0},\\
&\partial_t(hc) + \partial_x(huc) = E-D,\\
&\partial_t z_{\mathrm{b}} + \frac{1}{1-\psi_0}\partial_x q_{\mathrm{b}} = -\frac{E-D}{1-\psi_0},\\
&\partial_t h_{\mathrm{g}} = -(\dot{\eta}_{\mathrm{e}} - \dot{\eta}_{\mathrm{d}}),
\end{aligned} \tag{2.7a}$$

together with the incompressibility condition

$$w - u\partial_x z_{\mathrm{b}} + \partial_t z_{\mathrm{b}} + \frac{h}{2}\partial_x u = 0. \tag{2.7b}$$

This model consists of seven partial differential equations from which one seeks to determine the same number of scalar unknowns, namely h, u, w, c, z_{b}, h_{g}, and p_{nh} as functions of horizontal spatial position x and time t.

2.2.2 Bedload modelling

The bedload discharge is typically determined based on the shear stress acting on the bed and the critical shear stress required to initiate sediment motion. When the shear stress exceeds the critical threshold, sediment transport occurs. Various empirical models exist to predict bedload discharge, but many exhibit limitations such as the absence of a dissipative energy balance, mass conservation inconsistencies, or restricted applicability to specific flow conditions [35, 40]. In this subsection we present a class of bedload models that satisfies an energy balance (see Theorem 2.2). Firstly, non-equilibrium models are introduced. Secondly, the simplified case of equilibrium models, which is widely used in the literature, is presented. Finally, bedload models that take into account gravitational effects are discussed.

Non-equilibrium bedload models

In this case the bed evolution equations are given by

$$\partial_t z_{\mathrm{b}} + \frac{1}{1-\psi_0}\partial_x q_{\mathrm{b}} = -\frac{E-D}{1-\psi_0}, \quad \partial_t h_{\mathrm{g}} = \dot{\eta}_{\mathrm{d}} - \dot{\eta}_{\mathrm{e}},$$

where the bedload flux is modelled as $q_{\mathrm{b}} := h_{\mathrm{m}} V_{\mathrm{b}}$, with $h_{\mathrm{m}} := z_{\mathrm{b}} - h_{\mathrm{g}}$,

$$V_{\mathrm{b}} := v_{\mathrm{b}} \sqrt{(r_{\mathrm{s}} - 1) g d_{\mathrm{s}}}, \tag{2.8}$$

and $r_{\mathrm{s}} = \rho_{\mathrm{s}}/\rho_{\mathrm{f}}$ the density ratio. The sediment transport velocity is given by

$$v_{\mathrm{b}} := \mathrm{sgn}(\tau)(\sqrt{\theta} - \sqrt{\theta_{\mathrm{c}}})_{+}, \tag{2.9}$$

where the so-called Shields parameter θ is defined by

$$\theta := \frac{|\tau|}{\rho_{\mathrm{f}}(r_{\mathrm{s}} - 1) g d_{\mathrm{s}}},$$

and θ_{c} is the critical Shields parameter. Here τ represents the shear stress defined by

$$\frac{\tau}{\rho_{\mathrm{f}}} = C_{\mathrm{f}} u|u| \quad \text{with } C_{\mathrm{f}} = g n^2 h^{-1/3} \text{ (Manning law) or } C_{\mathrm{f}} = \xi/8 \text{ (Darcy-Weisbach law).} \tag{2.10}$$

Finally, the vertical entrainment and deposition rates are given by

$$\dot{\eta}_{\mathrm{e}} = (\theta - \theta_{\mathrm{c}})_{+} \frac{k_{\mathrm{e}}}{1 - \psi_0} \sqrt{(r_{\mathrm{s}} - 1) g d_{\mathrm{s}}}, \quad \dot{\eta}_{\mathrm{d}} = h_{\mathrm{m}} \frac{k_{\mathrm{d}}}{d_{\mathrm{s}}} \sqrt{(r_{\mathrm{s}} - 1) g d_{\mathrm{s}}}. \tag{2.11}$$

The erosion and deposition rates (E and D) are defined by empirical formulations, which will be detailed later in the numerical test (Section 2.4).

Equilibrium bedload models

If equilibrium conditions are assumed, i.e., $\dot{\eta}_{\mathrm{e}} = \dot{\eta}_{\mathrm{d}}$, we obtain by equating the right-hand sides in (2.11)

$$h_{\mathrm{m}} = \frac{d_{\mathrm{s}} k_{\mathrm{e}}}{k_{\mathrm{d}}(1 - \psi_0)} (\theta - \theta_{\mathrm{c}})_{+}, \tag{2.12}$$

which leads to the simplified bedload flux

$$q_{\mathrm{b}} = \mathrm{sgn}(\tau) \frac{k_{\mathrm{e}}}{k_{\mathrm{d}}} (\theta - \theta_{\mathrm{c}})_{+} (\sqrt{\theta} - \sqrt{\theta_{\mathrm{c}}}) \frac{d_{\mathrm{s}}}{1 - \psi_0} \sqrt{(r_{\mathrm{s}} - 1) g d_{\mathrm{s}}}. \tag{2.13}$$

This expression for q_{b} is substituted into the evolution equation for z_{b} in system (2.7a). Since the last equation, the evolution equation for h_{g}, is no longer needed, we obtain as a result the equilibrium version of model (2.7).

Notice that other definitions of $\dot{\eta}_{\mathrm{e}}$ and $\dot{\eta}_{\mathrm{d}}$ also imply different definitions of h_{m} for equilibrium models. The definition of h_{m} (2.12) implies the definition of q_{b} given by (2.13), that is a generalization of Ashida-Mishiue model [3]. Another variant of the definition of $\dot{\eta}_{\mathrm{e}}$ is

$$\dot{\eta}_{\mathrm{e}} = \frac{(\theta - \theta_{\mathrm{c}})_{+}^{3/2}}{\sqrt{\theta} - \sqrt{\theta_{\mathrm{c}}}} \frac{k_{\mathrm{e}}}{1 - \psi_0} \sqrt{(r_{\mathrm{s}} - 1) g d_{\mathrm{s}}},$$

which in the equilibrium case implies the solid transport discharge

$$q_{\mathrm{b}} = \mathrm{sgn}(\tau) \frac{k_{\mathrm{e}}}{k_{\mathrm{d}}} (\theta - \theta_{\mathrm{c}})_{+}^{3/2} \frac{d_{\mathrm{s}}}{1 - \psi_0} \sqrt{(r_{\mathrm{s}} - 1) g d_{\mathrm{s}}},$$

which is a generalization of the well-known Meyer-Peter and Müller model [53].

Shear stress and gravitational effects

The shear stress τ is typically chosen based on Manning's law but can be generalized to include gravitational effects in sediment transport. Following [40], we define an effective shear stress τ_{eff}:

$$\frac{\tau_{\mathrm{eff}}}{\rho_{\mathrm{f}}} = \frac{\tau}{\rho_{\mathrm{f}}} - k_1 \partial_x (h + z_{\mathrm{b}}) - k_2 \partial_x z_{\mathrm{b}}, \tag{2.14}$$

where $k_1 := \vartheta g d_{\mathrm{s}}$, $k_2 := \vartheta g d_{\mathrm{s}}(r_{\mathrm{s}} - 1)$, and $\vartheta := \theta_{\mathrm{c}} / \tan\delta$, with δ representing the angle of repose of the sediment material (commonly $\delta \approx 25°$). These additional terms account for gravitational effects through bed and free surface slopes. If τ_{eff} is used instead of τ then we obtain the effective Shields parameter

$$\theta_{\mathrm{eff}} := \frac{|\tau_{\mathrm{eff}}|}{\rho_{\mathrm{f}}(r_{\mathrm{s}} - 1) g d_{\mathrm{s}}}. \tag{2.15}$$

By writing τ_{eff} and θ_{eff} in place of τ and θ, respectively, in Eqs. (2.9) and (2.11) we obtain the final non-equilibrium model (2.7) with gravitational effects. Analogously, the final equilibrium model with gravitational effects is obtained by modifying Eq. (2.13) for the solid transport discharge accordingly with τ_{eff} and θ_{eff}.

If τ_{eff} as given by (2.14) is used within (2.15), then equation (2.5) will include second-order spatial derivatives. Consequently, explicit numerical methods require a stability condition of CFL $\propto 1/\Delta x^2$, which leads to undesirably small time steps. To mitigate this issue, a semi-implicit method [40] should be employed to ensure numerical stability without excessively restricting the time step size. This is detailed in next section.

2.2.3 Mass conservation

The principle of mass conservation is essential for constructing accurate models of sediment transport. The sediment mass $m_{\mathrm{s}} = m_{\mathrm{s}}(x,t)$ and the fluid mass $m_{\mathrm{f}} = m_{\mathrm{f}}(x,t)$ at position x and time t are given by

$$\begin{aligned} m_{\mathrm{s}}(x,t) &:= \rho_{\mathrm{s}}\big(h(x,t)c(x,t) + (1-\psi_0) z_{\mathrm{b}}(x,t)\big), \\ m_{\mathrm{f}}(x,t) &:= \rho_{\mathrm{f}}\big(h(x,t)(1-c(x,t)) + \psi_0 z_{\mathrm{b}}(x,t)\big), \end{aligned}$$

respectively. Namely, we obtain the following result, which is obtained straightforward from (2.1), (2.4), and (2.5):

Theorem 2.1 (Mass conservation)**.** *The model satisfies mass conservation. Specifically, the model implies the equations of conservation of sediment and fluid mass*

$$\begin{aligned} \partial_t m_{\mathrm{s}} + \partial_x \left(huc + q_{\mathrm{b}} \right) &= 0, \\ \partial_t m_{\mathrm{f}} + \partial_x \left(hu(1-c) + \frac{\psi_0}{1-\psi_0} q_{\mathrm{b}} \right) &= 0. \end{aligned}$$

2.2.4 Energy balance

The solid transport discharge q_b is defined in Section 2.2.2 in several alternative forms. All these definitions can be written in the general form

$$q_\mathrm{b} = h_\mathrm{m} V_\mathrm{b}, \quad V_\mathrm{b} = u - P, \quad P := C_1 \partial_x (h + z_\mathrm{b}) + C_2 \partial_x z_\mathrm{b} + C_3 (r_\mathrm{s} - 1) \operatorname{sgn}(V_\mathrm{b}) \tan\delta \tag{2.16}$$

with dimensional parameters C_1, C_2, C_3 that are defined in terms of physical values such as the gravity constant, the mean grain size diameter, and the critical Shields parameter (see Section 2.2.2). Moreover, $h_\mathrm{m} = z_\mathrm{b} - h_\mathrm{g}$ for non-equilibrium models while h_m is defined by (2.12) for equilibrium models. Finally, we define

$$\hat{\tau} := \tau + \rho_\mathrm{f} h_\mathrm{m} P, \tag{2.17}$$

where τ is a generic friction term (e.g., Manning or Darcy-Weisbach), see equation (2.10). This model satisfies the following dissipative energy balance:

Theorem 2.2 (Energy balance)**.** *Consider the system of equations (2.7), (2.16), and (2.17), describing shallow water flow with sediment transport and bed evolution. Then the total mechanical energy*

$$\mathcal{E} := \frac{g(h + z_\mathrm{b})^2}{2} + \frac{h(u^2 + w^2)}{2}$$

satisfies the dissipative balance law:

$$\begin{aligned} &\partial_t \mathcal{E} + \partial_x \left(u \left(\frac{hu^2 + hw^2}{2} + \frac{gh^2(1 + c(r_\mathrm{s} - 1))}{2} + p_\mathrm{nh} \right) + q_\mathrm{b}\, g(h + z_\mathrm{b}) + ghuz_\mathrm{b} \right) \\ &\le -\left\{ (r_\mathrm{s} - 1) h_\mathrm{m} |v_\mathrm{b}| \tan\delta + h_\mathrm{m} P^2 + u \frac{\tau}{\rho_\mathrm{f}} \right\} + c \partial_x (h^2 u) \frac{g(r_\mathrm{s} - 1)}{2}. \end{aligned} \tag{2.18}$$

For brevity, we omit the proof, which follows similar steps to those presented in [35]. Clearly, term in curled brackets on the right-hand side of (2.18) is non-negative under standard physical assumptions, and hence it contributes to energy dissipation.

However, the last term, which involves the spatial derivative $\partial_x (h^2 u)$, is not in conservative form and, in principle, may act either as a source or a sink of energy depending on the sign of the derivative. However, the structure of the term allows for a meaningful interpretation. In regions where $\partial_x (h^2 u) < 0$, the contribution is manifestly dissipative, since $c \in [0, 1]$ and the entire term is non-positive. In regions where $\partial_x (h^2 u) > 0$, the term can be rewritten as

$$c \partial_x (h^2 u) = \partial_x (h^2 u) - (1 - c) \partial_x (h^2 u),$$

where the first term $\partial_x (h^2 u)$ is conservative and can be absorbed into the energy flux (especially under appropriate boundary conditions). The second term, $-(1 - c) \partial_x (h^2 u)$, is non-positive in this case and thus it contributes to dissipation. In general, we have the identity

$$c\, \partial_x (h^2 u) = \partial_x \left(\frac{1 + \operatorname{sgn}(\partial_x (h^2 u))}{2} h^2 u \right) - \left(\frac{1 + \operatorname{sgn}(\partial_x (h^2 u))}{2} - c \right) \partial_x (h^2 u),$$

which is composed of a conservative term and a dissipative one. It follows that the full energy inequality consists of a collection of dissipative terms, and conservative fluxes that vanish under suitable boundary conditions. Therefore, the total mechanical energy satisfies a net dissipative balance law, and energy is non-increasing in time under these assumptions.

It is worth noting that, during the derivation of the energy balance (2.18), the term multiplying the non-hydrostatic pressure naturally yields the incompressibility condition (2.7b).

2.3 Numerical implementation

2.3.1 Preliminaries

To compute the model transition from time t_n to t_{n+1}, we should use a robust numerical scheme that can handle second derivatives, and preserve positivity of the needed variables. The discretization of governing system (2.7a) combines the following four ingredients: the underlying hydrostatic hyperbolic system with non-conservative products is solved; second-order derivative terms coming from the gravitational effects are included; source terms corresponding to the friction and erosion are deposition rates are incorporated; and non-hydrostatic pressure is computed and the horizontal and vertical velocities are accordingly corrected.

In the following we write the compact form of system (2.7a) in the non-equilibrium case but we do not include gravitational effects yet. These are handled in Section 2.3.5. To this aim, we denote by $\boldsymbol{W}$ the vector of conservative variables. The system (2.7a) is written in compact form as

$$\partial_t \boldsymbol{W} + \partial_x \boldsymbol{F}(\boldsymbol{W}) + \boldsymbol{B}(\boldsymbol{W})\partial_x \boldsymbol{W} = \boldsymbol{K}(\boldsymbol{W}) + \nabla_{\mathrm{NH}}\boldsymbol{Q}, \tag{3.1}$$

where we define

$$\boldsymbol{W} := \begin{pmatrix} h \\ hu \\ hw \\ hc \\ z_{\mathrm{b}} \\ h_{\mathrm{g}} \end{pmatrix}, \quad \boldsymbol{F}(\boldsymbol{W}) := \begin{pmatrix} hu \\ hu^2 + gh^2/2 \\ huw \\ huc \\ q_{\mathrm{b}}/(1-\psi_0) \\ 0 \end{pmatrix}, \quad \boldsymbol{B}(\boldsymbol{W}) := \begin{bmatrix} 0 & 0 & 0 & 0 & 0 & 0 \\ -c\gamma & 0 & 0 & \gamma & gh & 0 \\ 0 & 0 & 0 & 0 & 0 & 0 \\ 0 & 0 & 0 & 0 & 0 & 0 \\ 0 & 0 & 0 & 0 & 0 & 0 \\ 0 & 0 & 0 & 0 & 0 & 0 \end{bmatrix}, \tag{3.2}$$

along with $\gamma := g(r_{\mathrm{s}} - 1)h/2$, and the source and non-hydrostatic terms

$$\boldsymbol{K}(\boldsymbol{W}) := \begin{pmatrix} 0 \\ -\tau \\ 0 \\ 0 \\ 0 \\ \dot{\eta}_{\mathrm{d}} - \dot{\eta}_{\mathrm{e}} \end{pmatrix} + \frac{E-D}{1-\psi_0}\begin{pmatrix} 1 \\ u/2 \\ w/2 \\ 1-\psi_0 \\ -1 \\ 0 \end{pmatrix}, \quad \nabla_{\mathrm{NH}}\boldsymbol{Q} = \begin{pmatrix} 0 \\ -\partial_x(hq) - 2q\partial_x z_{\mathrm{b}} \\ 2q \\ 0 \\ 0 \\ 0 \end{pmatrix}.$$

We now describe the steps of the numerical scheme for non-equilibrium model with gravitational effects and non-hydrostatic pressure. This scheme is easily adapted to particular cases as hydrostatic pressure, the absence of gravitational effects, or the equilibrium regime. For simplicity, at each step we assume that the solution evolves from time t_* to t_{n+1}. So, $\boldsymbol{W}^*$ must be understood as the output of a previous stage.

2.3.2 Finite volume methods for non-conservative hyperbolic systems

We adopt the path-conservative framework [52, 55, 57] to deal with possible discontinuities in the solutions and the presence of non-conservative products in the underlying hyperbolic part of the system, i. e.,

$$\partial_t \boldsymbol{W} + \partial_x \boldsymbol{F}(\boldsymbol{W}) + \boldsymbol{B}(\boldsymbol{W})\partial_x \boldsymbol{W} = \boldsymbol{0}. \tag{3.3}$$

This system can be written in quasi-linear form as $\partial_t \boldsymbol{W} + \boldsymbol{A}(\boldsymbol{W})\partial_x \boldsymbol{W} = \boldsymbol{0}$ with the 6×6 matrix $\boldsymbol{A}(\boldsymbol{W}) \coloneqq \partial \boldsymbol{F}(\boldsymbol{W})/\partial \boldsymbol{W} + \boldsymbol{B}(\boldsymbol{W})$, whose eigenvalues are $\lambda \in \{0, u\}$ plus the four eigenvalues of the reduced matrix

$$\hat{\boldsymbol{A}}(\boldsymbol{W}) \coloneqq \begin{bmatrix} 0 & 1 & 0 & 0 \\ -u^2 + gh - c\gamma & 2u & \gamma & gh \\ -uc & c & u & 0 \\ \alpha_h & \alpha_{hu} & 0 & \alpha_{z_\mathrm{b}} \end{bmatrix}, \quad \alpha_\xi \coloneqq \frac{1}{1-\psi_0}\partial_\xi q_\mathrm{b} \quad \text{for } \xi \in \{h, hu, z_\mathrm{b}\}. \tag{3.4}$$

The characteristic polynomial of $\hat{\boldsymbol{A}}(\boldsymbol{W})$ can be written as

$$P(\lambda) = (\lambda - u)Q(\lambda),$$

with

$$Q(\lambda) = \lambda^3 - (\alpha_{z_\mathrm{b}} + u)\lambda^2 + (u^2 + 2u\alpha_{z_\mathrm{b}} - gh - gh\alpha_{hu})\lambda - u^2\alpha_{z_\mathrm{b}} - gh\alpha_h + gh\alpha_{z_\mathrm{b}}. \tag{3.5}$$

This factorization shows that the eigenvalues of the system are independent of the sediment concentration c since no terms involving c appear. The remaining three eigenvalues, associated with $Q(\lambda)$, can be computed analytically using Cardano's formula, yielding real and distinct values under typical flow conditions.

The FV discretization is based on the subdivision of the horizontal domain into uniform control volumes $V_i \coloneqq [x_{i-1/2}, x_{i+1/2}]$ of length Δx for $i \in \mathcal{I}$. It is assumed that $\boldsymbol{W}_i^n$ approximates the cell average of $\boldsymbol{W}$ on V_i at time t_n, i.e.,

$$\boldsymbol{W}_i^n \approx \frac{1}{\Delta x}\int_{V_i} \boldsymbol{W}(x, t_n)\,\mathrm{d}x.$$

For convenience, in the discretization we separate the convective and pressure terms in $\boldsymbol{F}(\boldsymbol{W})$. To this end we replace (3.3) by

$$\partial_t \boldsymbol{W} + \partial_x \boldsymbol{F}_\mathrm{c}(\boldsymbol{W}) + \boldsymbol{S}(\boldsymbol{W})\partial_x(h + z_\mathrm{b}) + \tilde{\boldsymbol{B}}(\boldsymbol{W})\partial_x \boldsymbol{W} = \boldsymbol{0},$$

where we define $\boldsymbol{S}(\boldsymbol{W}) \coloneqq (0, gh, 0, 0, 0, 0)^{\mathrm{T}}$. A usual first-order path-conservative explicit scheme now reads

$$\boldsymbol{W}_i^{n+1} = \boldsymbol{W}_i^n - \frac{\Delta x}{\Delta t}\left(\boldsymbol{\mathcal{F}}_{i+1/2}^n - \boldsymbol{\mathcal{F}}_{i-1/2}^n + \frac{1}{2}\big(\tilde{\boldsymbol{\mathcal{B}}}_{i+1/2}^n + \tilde{\boldsymbol{\mathcal{B}}}_{i-1/2}^n + \boldsymbol{\mathcal{S}}_{i+1/2}^n + \boldsymbol{\mathcal{S}}_{i-1/2}^n\big)\right),$$

where we define

$$\begin{aligned}
\tilde{\boldsymbol{\mathcal{B}}}_{i+1/2}^n &\coloneqq \frac{1}{2}\big(\tilde{\boldsymbol{B}}(\boldsymbol{W}_i^n) + \tilde{\boldsymbol{B}}(\boldsymbol{W}_{i+1}^n)\big)\big(\boldsymbol{W}_{i+1}^n - \boldsymbol{W}_i^n\big) \quad \text{and} \\
\boldsymbol{\mathcal{S}}_{i+1/2}^n &\coloneqq \frac{1}{2}\big(\boldsymbol{S}(\boldsymbol{W}_i^n) + \boldsymbol{S}(\boldsymbol{W}_{i+1}^n)\big)\big(h_{i+1/2}^{n,+} - h_{i+1/2}^{n,-}\big),
\end{aligned}$$

where $h_{i+1/2}^{n,\pm}$ are the reconstructed states to approximate the free surface gradient given by

$$\begin{aligned}
h_{i+1/2}^{n,+} &\coloneqq \max\big\{h_{i+1}^n + z_{\mathrm{b},i+1}^n - z_{i+1/2}^{*,n}, 0\big\}, \\
h_{i+1/2}^{n,-} &\coloneqq \max\big\{h_i^n + z_{\mathrm{b},i}^n - z_{i+1/2}^{*,n}, 0\big\}, \quad \text{and} \\
z_{i+1/2}^{*,n} &\coloneqq \max\big\{z_{\mathrm{b},i}^n, z_{\mathrm{b},i+1}^n\big\}.
\end{aligned}$$

These states are also useful to handle wet/dry areas. In what follows we omit the upper index n for simplicity. The numerical flux $\boldsymbol{\mathcal{F}}_{i+1/2}$ is defined according to a PVM scheme (see [28]), where the viscosity matrix is defined as a polynomial evaluation of the Roe matrix $\boldsymbol{A}_{i+1/2}$. This matrix is assumed to satisfy the relation

$$\boldsymbol{A}_{i+1/2}(\boldsymbol{W}_{i+1} - \boldsymbol{W}_i) = \boldsymbol{F}(\boldsymbol{W}_{i+1}) - \boldsymbol{F}(\boldsymbol{W}_i) + \int_0^1 \boldsymbol{B}_\Phi(s; \boldsymbol{W}_{i+1}, \boldsymbol{W}_i)\partial_s \Phi(s; \boldsymbol{W}_{i+1}, \boldsymbol{W}_i)\,\mathrm{d}s, \quad (3.6)$$

where $\boldsymbol{F}$ and $\boldsymbol{B}$ are as given in (3.2). For convenience, we assume a general second-order PVM scheme. This includes all particular cases studied herein, namely the Rusanov, HLL, and PVM-2I schemes. Then the general numerical flux is

$$\begin{aligned}
\boldsymbol{\mathcal{F}}_{i+1/2} = \frac{1}{2}\big(\boldsymbol{F}_{\mathrm{c}}(\boldsymbol{W}_{i+1}) + \boldsymbol{F}_{\mathrm{c}}(\boldsymbol{W}_i)\big) - \frac{1}{2}\Big(&\alpha_{0,i+1/2}\big(\boldsymbol{W}_{i+1/2}^+ - \boldsymbol{W}_{i+1/2}^-\big) \\
&+ (\alpha_{1,i+1/2}\boldsymbol{I} + \alpha_{2,i+1/2}\boldsymbol{A}_{i+1/2})\big(\boldsymbol{F}(\boldsymbol{W}_{i+1}) - \boldsymbol{F}(\boldsymbol{W}_i) + \tilde{\boldsymbol{\mathcal{B}}}_{i+1/2} + \boldsymbol{\mathcal{S}}_{i+1/2}\big)\Big)
\end{aligned} \quad (3.7)$$

with $\boldsymbol{I}$ the identity matrix, and $\boldsymbol{W}_{i+1/2}^{\pm}$ are the reconstructed states

$$\begin{aligned}
\boldsymbol{W}_{i+1/2}^- &\coloneqq \big(h_{i+1/2}^-, h_{i+1/2}^- u_i, h_{i+1/2}^- w_i, h_{i+1/2}^- c_i, z_{\mathrm{b},i}, h_{\mathrm{g},i}\big)^{\mathrm{T}}, \\
\boldsymbol{W}_{i+1/2}^+ &\coloneqq \big(h_{i+1/2}^+, h_{i+1/2}^+ u_{i+1}, h_{i+1/2}^+ w_{i+1}, h_{i+1/2}^+ c_{i+1}, z_{\mathrm{b},i+1}, h_{\mathrm{g},i+1}\big)^{\mathrm{T}}.
\end{aligned}$$

Notice that the reconstructed states are used just for the well-balancing of the scheme and the wet/dry treatment.

2.3.3 Well-balanced property of HLL and Rusanov methods for SVE systems

The well-balance property of the scheme is a requirement not only to preserve steady solutions but also to reproduce solutions that consist in small perturbations (similar to the truncation error of the method) of equilibrium states. For the design of the scheme for (2.7a) we focus on equilibrium states at rest, although other equilibrium states with $u \neq 0$ will equally be preserved (see, e.g., Section 2.4.2). The steady states at rest (with no erosion) satisfy

$$h + z_{\mathrm{b}} = \text{constant}, \quad |\partial_x z_{\mathrm{b}}| < \tan\delta, \quad u = w = p_{\mathrm{nh}} = 0, \quad c = 0, \quad E = D, \quad \dot{\eta}_{\mathrm{e}} = \dot{\eta}_{\mathrm{d}}. \tag{3.8}$$

The condition for the bottom slope is deduced from $\theta_{\mathrm{eff}} < \theta_{\mathrm{c}}$ with $u = 0$ and $h + z_{\mathrm{b}} = \text{const}$. It is remarkable that these are steady states when gravitational effects are incorporated. Otherwise, no condition on the bottom slope is necessary.

The Rusanov and HLL methods are defined by (3.7) where the numerical diffusion of the scheme is defined in terms of the constant and first-order polynomials $P_0^{\mathrm{RU}}(x)$ and $P_1^{\mathrm{HLL}}(x)$, respectively, given by $\alpha_2^{\mathrm{RU}} = \alpha_2^{\mathrm{HLL}} = 0$ and

$$\begin{aligned} &P_0^{\mathrm{RU}}(x) := \alpha_0^{\mathrm{RU}} \quad \text{with } \alpha_0^{\mathrm{RU}} := \max(\{|S_{\mathrm{L}}|, |S_{\mathrm{R}}|\}, \\ &P_1^{\mathrm{HLL}}(x) := \alpha_0^{\mathrm{HLL}} + \alpha_1^{\mathrm{HLL}} x \quad \text{with} \quad \alpha_0^{\mathrm{HLL}} := \frac{S_{\mathrm{R}}|S_{\mathrm{L}}| - S_{\mathrm{L}}|S_{\mathrm{R}}|}{S_{\mathrm{R}} - S_{\mathrm{L}}}, \quad \alpha_1^{\mathrm{HLL}} := \frac{|S_{\mathrm{R}}| - |S_{\mathrm{L}}|}{S_{\mathrm{R}} - S_{\mathrm{L}}}, \end{aligned} \tag{3.9}$$

where S_{L} and S_{R} are approximations of the largest and the smallest eigenvalues, respectively, of the Roe matrix of the system $\boldsymbol{A}_{i+1/2}$.

These definitions do not lead to a well-balanced scheme in the case of an SVE system due to the evolution equation for the sediment layer z_{b}. Concretely, the term $\alpha_{0,i+1/2}(z_{\mathrm{b},i+1} - z_{\mathrm{b},i})$ does not vanish in that equation for steady states. This behaviour results in a non-physical erosion of the bed. In [32] a modification of HLL method was proposed that neglects this term (in combination with an upwind approximation). Apart from that, to the best of our knowledge from literature, well-balanced Rusanov or HLL-type schemes for sediment transport problems have not been developed so far. Here we propose a simple modification of the Rusanov and HLL schemes for system (2.7a) with the well-balance property. This modification consists of an appropriate correction to the numerical viscosity related to the contribution $\alpha_{0,i+1/2}(z_{\mathrm{b},i+1} - z_{\mathrm{b},i})$ inspired by the case of the equilibrium model. So, a compelling approach to address this problem involves interpreting the non-equilibrium model as a generalization of the SVE framework. To this end, we consider the evolution equations for the bottom layer variables z_{b}, h_{m} and h_{g}:

$$\partial_t z_{\mathrm{b}} + \frac{1}{1-\psi_0}\partial_x q_{\mathrm{b}} = 0, \qquad \partial_t h_{\mathrm{m}} + \frac{1}{1-\psi_0}\partial_x q_{\mathrm{b}} = 0, \qquad \partial_t h_{\mathrm{g}} = 0,$$

where for sake of simplicity, we neglect erosion or deposition contributions (i.e., we set $E = D$) as in the steady state (3.8). In general, we use the equations for z_{b} and h_{g} to compute h_{m} as $z_{\mathrm{b}} - h_{\mathrm{g}}$. Let us consider the Rusanov or HLL method to evolve from t_n to t_{n+1}, i.e.,

$$\begin{aligned} z_{\mathrm{b},i}^{n+1} = z_{\mathrm{b},i}^{n} &- \frac{\Delta t}{\Delta x}\left(\frac{q_{\mathrm{b},i}^n + q_{\mathrm{b},i+1}^n}{2} - \frac{1}{2}\big(\alpha_{0,i+1/2}^n \Delta z_{\mathrm{b},i+1/2}^n + \alpha_{1,i+1/2}^n \Delta q_{\mathrm{b},i+1/2}^n\big)\right) \\ &+ \frac{\Delta t}{\Delta x}\left(\frac{q_{\mathrm{b},i}^n + q_{\mathrm{b},i-1}^n}{2} - \frac{1}{2}\left(\alpha_{0,i-1/2}^n \Delta z_{\mathrm{b},i-1/2}^n + \alpha_{1,i-1/2}^n \Delta q_{\mathrm{b},i-1/2}^n\right)\right), \end{aligned} \tag{3.10a}$$

$$
\begin{aligned}
h_{\mathrm{m},i}^{n+1} = h_{\mathrm{m},i}^{n} - \frac{\Delta t}{\Delta x}\left(\frac{q_{\mathrm{b},i}^{n}+q_{\mathrm{b},i+1}^{n}}{2} - \frac{1}{2}\big(\alpha_{0,i+1/2}^{n}\Delta h_{\mathrm{m},i+1/2}^{n} + \alpha_{1,i+1/2}^{n}\Delta q_{\mathrm{b},i+1/2}^{n}\big)\right) \\
+ \frac{\Delta t}{\Delta x}\left(\frac{q_{\mathrm{b},i}^{n}+q_{\mathrm{b},i-1}^{n}}{2} - \frac{1}{2}\left(\alpha_{0,i-1/2}^{n}\Delta h_{\mathrm{m},i-1/2}^{n} + \alpha_{1,i-1/2}^{n}\Delta q_{\mathrm{b},i-1/2}^{n}\right)\right), \qquad (3.10\mathrm{b})
\end{aligned}
$$

$$
h_{\mathrm{g},i}^{n+1} = h_{\mathrm{g},i}^{n}, \qquad (3.10\mathrm{c})
$$

where α_0, α_1 are defined by (3.9), and $\Delta\xi_{i+1/2} = \xi_{i+1} - \xi_i$ for $\xi \in \{z_\mathrm{b}, h_\mathrm{m}, q_\mathrm{b}\}$. By subtracting (3.10b) from (3.10a) we obtain for h_g

$$
h_{\mathrm{g},i}^{n+1} - h_{\mathrm{g},i}^{n} = \frac{1}{2}\frac{\Delta t}{\Delta x}\left[\alpha_{0,i+1/2}^{n}\left(\Delta z_{\mathrm{b},i+1/2}^{n} - \Delta h_{\mathrm{m},i+1/2}^{n}\right) - \alpha_{0,i-1/2}^{n}\left(\Delta z_{\mathrm{b},i-1/2}^{n} - \Delta h_{\mathrm{m},i-1/2}^{n}\right)\right], \qquad (3.11)
$$

whose right-hand side term will not vanish in general. This property produces an inconsistency error with respect to (3.10c) due to the numerical diffusion.

This inconsistency may lead to different numerical results depending on the pair of equations used to compute z_b, h_m, and h_g. In some cases, it may even produce unphysical values such as negative h_m (or z_b, h_g, depending on the formulation), or more generally, violate the relation $z_\mathrm{b} = h_\mathrm{m} + h_\mathrm{g}$ at the discrete level. Therefore, it is necessary to introduce a modified approach that resolves the discrepancy in the numerical viscosity term while ensuring consistency with the stationary solutions. To handle this issue we propose to replace the discrete differences Δz_b and Δh_m in Eqs. (3.10a) and (3.10b), respectively, by a consistent approximation based on the equilibrium model:

$$
h_\mathrm{m}^\mathrm{eq} = \frac{d_\mathrm{s} k_\mathrm{e}}{(1-\psi_0)k_\mathrm{d}}(\theta - \theta_\mathrm{c})_+, \qquad (3.12)
$$

However, since Δz_b originally appears in the numerical viscosity term, it plays a crucial role in determining the direction of artificial diffusion. In fact, replacing Δz_b by $\Delta h_\mathrm{m}^\mathrm{eq}$ without adjusting its sign may lead to inconsistencies in the numerical flux. To address this issue, we replace the expression of the discrete jump $\Delta z_{\mathrm{b},i+1/2}$ and $\Delta h_{\mathrm{m},i+1/2}$ in (3.10a) and (3.10b) by

$$
\Delta h_{\mathrm{m},i+1/2}^\mathrm{eq} = \frac{d_\mathrm{s} k_\mathrm{e}}{(1-\psi_0)k_\mathrm{d}}\left|(\theta_{i+1} - \theta_\mathrm{c})_+ - (\theta_i - \theta_\mathrm{c})_+\right| \operatorname{sgn}(\Delta z_{\mathrm{b},i+1/2}), \qquad (3.13)
$$

where we explicitly include the sign of the slope. This formulation ensures that we use the appropriate sign to preserve the directionality of the numerical viscosity. Thus, artificial oscillations or inconsistencies in the discrete sediment flux are avoided. Moreover, this modification guarantees consistency in the computation of z_b, h_m, and h_g independently of the chosen pair of equations in (3.10). It also preserves the desired steady states when $\theta_\mathrm{eff} < \theta_\mathrm{c}$, since $h_{\mathrm{m},i+1/2}^\mathrm{eq}$ naturally vanishes in those regions. Finally, since this correction is consistent with the definition of the equilibrium model, it results in a well-balanced scheme also in the equilibrium case. In order to clarify the effect of the proposed well-balanced correction on the numerical diffusion, we include a sketch in Figure 2.2, where non-steady and steady (3.8) states are depicted.

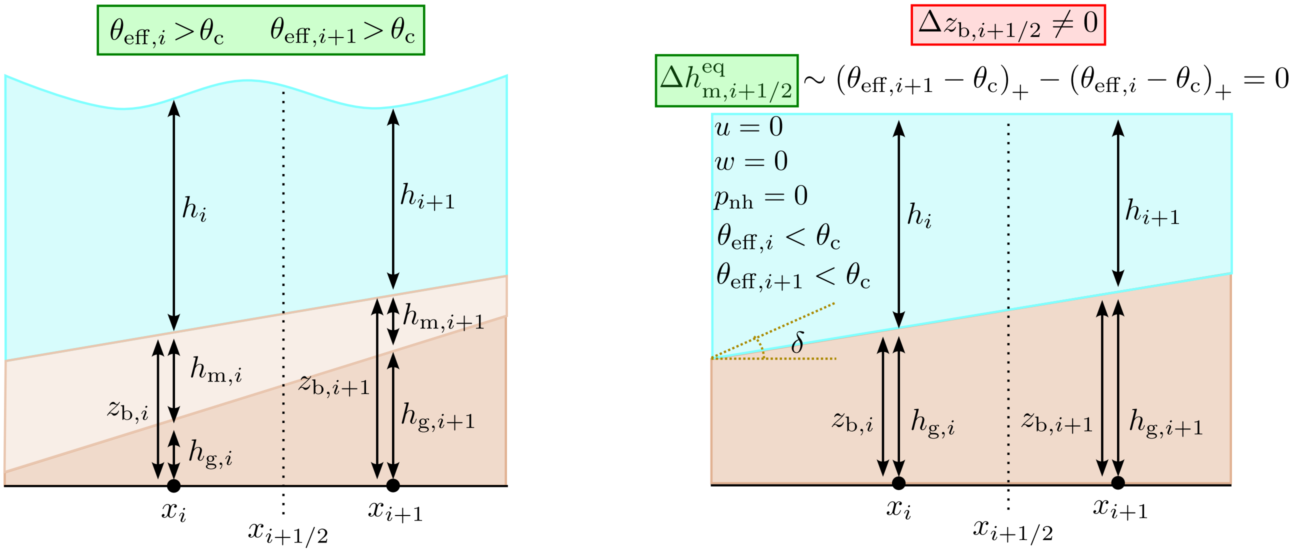

Figure 2.2: Sketch of non-steady configuration (left-hand side) and steady state (3.8) (right-hand side) with $\tan(\delta)$ and the well-balanced correction of the numerical diffusion, for Rusanov and HLL schemes, in terms of $\Delta h^{\mathrm{eq}}_{\mathrm{m},i+1/2}$ instead of $\Delta z_{\mathrm{b},i+1/2}$.

2.3.4 PVM-2I method

The introduction of a new accurate scheme for sediment transport is motivated by some shortcomings of the Rusanov and HLL methods. They are not only not well-balanced (without corrections) as mentioned earlier, but also introduce a high level of numerical viscosity, especially for the evolution equation of z_{b}, which causes excessively rapid, physically inaccurate erosion. To handle these issues we propose a combination of the Rusanov or HLL method with a three-wave PVM method. The resulting new method will be denoted as PVM-2I method (since it is defined by a quadratic polynomial and employs an intermediate eigenvalue), and it is well-balanced by construction. The main idea is, in order to reduce the numerical diffusion associated to the bottom evolution equation, to use a second-degree PVM method just for that equation. Thus, the PVM-2I method is defined by the numerical flux (3.7) for all unknowns except for the sediment bed, that in this case is

$$\begin{aligned}[\boldsymbol{\mathcal{F}}_{i+1/2}]_{z_{\mathrm{b}}} = {} & \frac{1}{2}(q_{\mathrm{b},i} + q_{\mathrm{b},i+1}) \\ & - \frac{1}{2}\big(\alpha^{2\mathrm{I}}_{0,i+1/2}\Delta z_{\mathrm{b},i+1/2} + \alpha^{2\mathrm{I}}_{1,i+1/2}\Delta q_{\mathrm{b},i+1/2} + \alpha^{2\mathrm{I}}_{2,i+1/2}[\boldsymbol{A}_{i+1/2}\Delta \boldsymbol{F}_{i+1/2}]_{z_{\mathrm{b}}}\big),\end{aligned} \tag{3.14}$$

where $[\boldsymbol{A}_{i+1/2}\Delta \boldsymbol{F}_{i+1/2}]_{z_{\mathrm{b}}}$ denotes the component corresponding to the evolution of z_{b} of the product

$$\boldsymbol{A}_{i+1/2}\Delta \boldsymbol{F}_{i+1/2} = \boldsymbol{A}_{i+1/2}\big(\boldsymbol{F}(\boldsymbol{W}_{i+1}) - \boldsymbol{F}(\boldsymbol{W}_i) + \tilde{\boldsymbol{\mathcal{B}}}_{i+1/2} + \boldsymbol{\mathcal{S}}_{i+1/2}\big),$$

and $\alpha^{2\mathrm{I}}_{k,i+1/2}$, $k = 0, 1, 2$, are the coefficients of the polynomial $P^{2\mathrm{I}}_2(x) \coloneqq \alpha^{2\mathrm{I}}_0 + \alpha^{2\mathrm{I}}_1 x + \alpha^{2\mathrm{I}}_2 x^2$ that satisfies $P_2(S_{\mathrm{L}}) = |S_{\mathrm{L}}|$, $P_2(S_{\mathrm{I}}) = |S_{\mathrm{I}}|$, and $P_2(S_{\mathrm{R}}) = |S_{\mathrm{R}}|$, where S_{I} is an estimate of an intermediate eigenvalue, which is detailed below. The coefficients of this polynomial are given by

$$\begin{aligned}
\alpha_0^{2\mathrm{I}} &= \alpha_0^{\mathrm{HLL}} + \alpha_2^{2\mathrm{I}} S_{\mathrm{L}} S_{\mathrm{R}}, \quad \alpha_1^{2\mathrm{I}} = \alpha_1^{\mathrm{HLL}} - \alpha_2^{2\mathrm{I}} (S_{\mathrm{R}} + S_{\mathrm{L}}), \\
\alpha_2^{2\mathrm{I}} &= \frac{(|S_{\mathrm{R}}| - |S_{\mathrm{I}}|)(S_{\mathrm{I}} - S_{\mathrm{L}}) - (|S_{\mathrm{I}}| - |S_{\mathrm{L}}|)(S_{\mathrm{R}} - S_{\mathrm{I}})}{(S_{\mathrm{R}} - S_{\mathrm{L}})(S_{\mathrm{R}} - S_{\mathrm{I}})(S_{\mathrm{I}} - S_{\mathrm{L}})}.
\end{aligned} \tag{3.15}$$

The key point is that S_{I} is chosen in such a way that $S_{\mathrm{I}} = 0$ in the case of no sediment transport. So, $\alpha_0^{2\mathrm{I}} = 0$ in such case, and the diffusion term in (3.14) vanishes, therefore steady solutions are preserved and non-physical erosion is avoided. With this in mind, we choose S_{I} as the intermediate root of the cubic polynomial given by (3.5). Notice that the new coefficients (3.15) can be seen as a correction of the numerical viscosity associated to the usual HLL scheme.

Let us remark that the PVM-2I scheme preserves the positivity of the water depth since it coincides with HLL for the mass and momentum equations for these equations (see [12]). It is worth mentioning that we are not able to prove the water depth positivity when applying the second-degree PVM with $\alpha_{0,1,2}^{2\mathrm{I}}$ given by (3.15) for the whole system. Furthermore, although we do not have a general proof of positivity of the sediment bed for the PVM-2I scheme, we have not observed related troubles in the numerical experiments. Actually, positivity can be controlled by diminishing the time step, and the bed evolution is related to a much smaller velocity than water waves. Consequently, as long as the time step is adapted with a CFL condition suitable for water waves, it is sufficiently small to handle the bed evolution. This property explains why in practice we have not found any trouble with sediment positivity thickness.

2.3.5 Semi-implicit step for gravitational terms

In numerical modelling of sediment transport, gravitational terms influence the vertical motion of particles, particularly their settling and redistribution. A fully explicit approach to incorporate gravitational effects may impose restrictive time-step constraints due to stability limitations, particularly when dealing with fine sediment or high particle concentrations. To overcome these limitations, a semi-implicit numerical scheme is employed, which enhances stability while maintaining computational efficiency. The semi-implicit formulation discretizes the gravitational terms in a manner that allows for larger time steps without introducing significant numerical errors. By treating some components implicitly, the method mitigates the instability associated with rapid particle settling while preserving accuracy.

First, following [40], rewrite the solid transport discharge in a form that is convenient for its discretization. Then, using the interpretation $\mathrm{sgn}(\tau_{\mathrm{eff}}) = \tau_{\mathrm{eff}}/|\tau_{\mathrm{eff}}|$, we may rewrite the solid transport discharge term as

$$\frac{1}{1-\psi_0} q_{\mathrm{b}} = \tilde{q}_{\mathrm{b}} \tau_{\mathrm{eff}} = \tilde{q}_{\mathrm{b}} \big(C_{\mathrm{f}} u|u| - \partial_x (k_1 (h + z_{\mathrm{b}}) + k_2 z_{\mathrm{b}}) \big), \tag{3.16}$$

Table 2.2: Efficiency comparison between the semi-implicit and explicit discretization of gravitational effects. L^1–e_h and L^1–e_{z_b} denote the L^1-norm errors of the water depth h and the bed elevation z_b, respectively, while CPU is the computational time measured. The reference solution was obtained using the semi-implicit scheme with 10.000 control volumes.

Number of	Semi-implicit			Explicit		
control volumes	CPU [s]	L^1-e_h	L^1-e_{z_b}	CPU [s]	L^1-e_h	L^1-e_{z_b}
500	1.24×10^3	2.90×10^{-3}	2.66×10^{-3}	2.81×10^4	2.71×10^{-3}	2.47×10^{-3}
1000	4.69×10^3	1.91×10^{-3}	1.75×10^{-3}	1.09×10^5	1.70×10^{-3}	1.54×10^{-3}
1500	9.95×10^3	1.32×10^{-3}	1.22×10^{-3}	2.44×10^5	1.10×10^{-3}	1.01×10^{-3}

with $k_1 := \vartheta g d_\mathrm{s}$, $k_2 := \vartheta g d_\mathrm{s}(r_\mathrm{s}-1)$, $\vartheta := \theta_\mathrm{c}/\tan\delta$, and

$$\tilde{q}_\mathrm{b} = \frac{h_\mathrm{m}\sqrt{(r_\mathrm{s}-1)gd_\mathrm{s}}\,(\sqrt{\theta_\mathrm{eff}}-\sqrt{\theta_\mathrm{c}})_+}{(1-\psi_0)|\tau_\mathrm{eff}/\rho_\mathrm{f}|}. \tag{3.17}$$

At this point, we incorporate the gravitational effects for the sediment evolution equation (z_b), which is discretized in time as

$$z_\mathrm{b}^{n+1} = z_\mathrm{b}^n - \Delta t\partial_x\left(\tilde{q}_\mathrm{b}^n(C_\mathrm{f}^n u^n|u^n| - k_1\partial_x(h^{n+1}+z_\mathrm{b}^{n+1}) - k_2\partial_x z_\mathrm{b}^{n+1})\right). \tag{3.18}$$

Using the Θ−method, we get

$$\begin{aligned} z_\mathrm{b}^{n+1} = z_\mathrm{b}^n - \Delta t\partial_x\big(\tilde{q}_\mathrm{b}^n C_\mathrm{f}^n u^n|u^n|\big) + (1-\Theta)\Delta t\partial_x\big(\tilde{q}_\mathrm{b}^n(k_1\partial_x(h^n+z_\mathrm{b}^n)+k_2\partial_x z_\mathrm{b}^n)\big) \\ + \Theta\Delta t\partial_x\big(\tilde{q}_\mathrm{b}^n(k_1\partial_x(h^{n+1}+z_\mathrm{b}^{n+1})+k_2\partial_x z_\mathrm{b}^{n+1})\big), \end{aligned} \tag{3.19}$$

where h^{n+1} was computed in the first hyperbolic step, see section 2.3.2. After using finite difference approximations for the space derivatives, a tridiagonal linear system for the unknowns $z_{\mathrm{b},i}^{n+1}$ is solved.

It is worth mentioning the practical advantage of the semi-implicit treatment of the gravitational terms compared to a fully explicit formulation. To illustrate this aspect, both approaches were tested under identical numerical conditions for the stationary test described in Section 2.4.2 (case $Q_0 = 10$). The results are summarized in Table 2.2. The semi-implicit scheme allows for significantly larger time steps and a considerable reduction in computational cost, while maintaining stable and accurate solutions.

We remark that, in case of dealing with subcritical flows (Fr $\ll 1$) a semi-implicit discretization as in [40], where the pressure gradient is removed from the stability restriction, may be convenient to improve the efficiency of large-time simulations. However, this is not the goal of this paper and it has not been implemented here.

2.3.6 Source terms related to erosion and deposition

In this step, we add the source terms related with the erosion (E/D) and deposition velocities ($\dot{\eta}_{\rm e}/\dot{\eta}_{\rm d}$). In order to ensure the positivity of the variables $z_{\rm b}$, $h_{\rm g}$, $h_{\rm m}$, and c we define

$$\hat{E} := \frac{E^n(h_{\rm m}^{n+1} + h_{\rm g}^{n+1})}{h_{\rm m}^n + h_{\rm g}^n} \qquad \text{and} \qquad \hat{D} := \frac{(hc)^{n+1}D^n}{(hc)^n}, \tag{3.20}$$

and apply a semi-implicit treatment similar to that of [43]. At each control volume V_i, this yields

$$\begin{aligned}
(1-\psi_0)h_{\rm m}^{n+1} &= (1-\psi_0)h_{\rm m}^* + (1-\psi_0)\Delta t\left(h_{\rm g}^{n+1}\frac{\dot{\eta}_{\rm e}^n}{h_{\rm g}^n} - h_{\rm m}^{n+1}\frac{\dot{\eta}_{\rm d}^n}{h_{\rm m}^n}\right) - \Delta t(\hat{E}-\hat{D}),\\
(1-\psi_0)h_{\rm g}^{n+1} &= (1-\psi_0)h_{\rm g}^* - (1-\psi_0)\Delta t\left(h_{\rm g}^{n+1}\frac{\dot{\eta}_{\rm e}^n}{h_{\rm g}^n} - h_{\rm m}^{n+1}\frac{\dot{\eta}_{\rm d}^n}{h_{\rm m}^n}\right),\\
(hc)^{n+1} &= (hc)^* + \Delta t(\hat{E}-\hat{D}),
\end{aligned} \tag{3.21}$$

where for sake of simplicity the spatial index i was omitted. The linear system (3.21) is solved for $h_{\rm m}^{n+1}$, $h_{\rm g}^{n+1}$, and $(hc)^{n+1}$. Next, we update the height and discharges as

$$\begin{aligned}
h^{n+1} &= h^* + \frac{\Delta t}{1-\psi_0}(\hat{E}-\hat{D}),\\
(hu)^{n+1} &= (hu)^* + \frac{u^n}{2}\frac{\Delta t}{1-\psi_0}(\hat{E}-\hat{D}) - \Delta t C_{\rm f}^n|u^n|u^{n+1},\\
(hw)^{n+1} &= (hw)^* + \frac{w^n}{2}\frac{\Delta t}{1-\psi_0}(\hat{E}-\hat{D}).
\end{aligned} \tag{3.22}$$

Notice that the use of $\hat{E}$ and $\hat{D}$ instead of E and D, respectively, in the previous equations guarantees that $\partial_t(h+z_{\rm b}) + \partial_x(hu + q_{\rm b}/(1-\psi_0)) = 0$ holds also at discrete level. The following theorem ensures the positivity of $h_{\rm g}$, $z_{\rm b}$ and hc. Moreover, the positivity of $h_{\rm m}$ is ensured under an additional condition. We have verified the positivity of $h_{\rm m}$ in all simulations, even if this property has not been proven analytically.

Theorem 2.3 (Positivity of the variables)**.** *Assume that $h_{\rm m}^* \geq 0$, $h_{\rm g}^* \geq 0$, and $(hc)^* \geq 0$ are given, and that $h_{\rm m}^{n+1}$, $h_{\rm g}^{n+1}$, and $(hc)^{n+1}$, are to be determined from the linear system of equations* (3.21)*. Then the system has a unique solution with the following properties:*

i) $z_{\rm b}^{n+1} := h_{\rm m}^{n+1} + h_{\rm g}^{n+1} \geq 0$, $h_{\rm g}^{n+1} \geq 0$, *and* $(hc)^{n+1} \geq 0$.

ii) A sufficient (but not necessary) condition to ensure $h_{\rm m}^{n+1} \geq 0$ is

$$E^n \leq \dot{\eta}_e^n(1-\psi_0)\frac{z_{\rm b}^n}{h_{\rm g}^n}. \tag{3.23}$$

Proof. For sake of clarity, we introduce $x_0 := (1-\psi_0)h_{\mathrm{m}}^*$, $y_0 := (1-\psi_0)h_{\mathrm{g}}^*$, $w_0 := (hc)^*$, and

$$a = \Delta t \frac{\dot{\eta}_{\mathrm{e}}^n}{h_{\mathrm{g}}^n}, \quad b = \Delta t \frac{\dot{\eta}_{\mathrm{d}}^n}{h_{\mathrm{m}}^n}, \quad e = \frac{\Delta t}{1-\psi_0}\frac{E^n}{h_{\mathrm{m}}^n + h_{\mathrm{g}}^n}, \quad f = \Delta t \frac{D^n}{(hc)^n};$$

then the system (3.21) can be written as

$$\begin{bmatrix} 1+b+e & e-a & -f \\ -b & 1+a & 0 \\ -e & -e & 1+f \end{bmatrix} \begin{pmatrix} (1-\psi_0)h_{\mathrm{m}}^{n+1} \\ (1-\psi_0)h_{\mathrm{g}}^{n+1} \\ (hc)^{n+1} \end{pmatrix} = \begin{pmatrix} x_0 \\ y_0 \\ w_0 \end{pmatrix}.$$

The solution of this system is

$$\begin{aligned} (1-\psi_0)h_{\mathrm{m}}^{n+1} &= \frac{(1+a+f)x_0 + af(x_0+y_0+w_0) + (a-e)y_0 + fw_0}{(1+a+b)(1+e+f)}, \\ (1-\psi_0)h_{\mathrm{g}}^{n+1} &= \frac{(1+b+e+f)y_0 + bf(x_0+y_0+w_0) + bx_0}{(1+a+b)(1+e+f)}, \\ (hc)^{n+1} &= \frac{w_0 + e(x_0+y_0+w_0)}{1+e+f}. \end{aligned}$$

Since the coefficients a, b, e, and f are non-negative, and since we assume that $h_{\mathrm{m}}^* \geq 0$, $h_{\mathrm{g}}^* \geq 0$ and $(hc)^* \geq 0$, it follows that $x_0, y_0, w_0 \geq 0$, hence $h_{\mathrm{g}}^{n+1} \geq 0$ and $(hc)^{n+1} \geq 0$. Moreover,

$$z_{\mathrm{b}}^{n+1} = h_{\mathrm{m}}^{n+1} + h_{\mathrm{g}}^{n+1} = \frac{(x_0+y_0)(1+f) + w_0 f}{(1+e+f)(1-\psi_0)} \geq 0.$$

If, in addition, assumption (3.23) is in effect, then $a \geq e$, and as a consequence all terms defining h_{m}^{n+1} are nonnegative. □

2.3.7 Incorporation of non-hydrostatic pressure

The non-hydrostatic pressure is incorporated by a projection method that only affects the momentum conservation equations. Since other variables are not affected by this correction, we have

$$h^{n+1} = h^*, \quad (hc)^{n+1} = (hc)^*, \quad z_{\mathrm{b}}^{n+1} = z_{\mathrm{b}}^*, \quad h_{\mathrm{g}}^{n+1} = h_{\mathrm{g}}^n.$$

We write the semi-discrete momentum equations as

$$(hu)^{n+1} = (hu)^* - \Delta t\big(\partial_x(h^{n+1}q^{n+1}) + 2p_{\mathrm{nh}}^{n+1}\partial_x z_{\mathrm{b}}^{n+1}\big), \tag{3.24}$$

$$(hw)^{n+1} = (hw)^* + 2\Delta t p_{\mathrm{nh}}^{n+1}, \tag{3.25}$$

and inserting these expressions into the incompressibility condition (2.7b) we get the elliptic equation

$$(h^{n+1})^2\partial_{xx}p_{\text{nh}}^{n+1}+h^{n+1}\partial_x h^{n+1}\partial_x p_{\text{nh}}^{n+1}+\Big(h^{n+1}\partial_{xx}(h^{n+1}+2z_{\text{b}}^{n+1})-\big(\partial_x(h^{n+1}+2z_{\text{b}}^{n+1})\big)^2-4\Big)p_{\text{nh}}^{n+1}$$
$$=\frac{1}{\Delta t}\big(2(hw)^*-(hu)^*\partial_x(h^{n+1}+2z_{\text{b}}^{n+1})+h^{n+1}\partial_x(hu)^*\big). \qquad (3.26)$$

To numerically find the non-hydrostatic pressure values, we locate the corresponding variables at the cell interfaces $x_{i+1/2}$, and we define $p_{\text{nh},i+1/2}^{n+1} := p_{\text{nh}}(x_{i+1/2},t_{n+1})$. Then, Eq. (3.26) is discretized at the cell interfaces as it is done in [39], where all the details are given. Once the new values of the non-hydrostatic pressure (p_{nh}^{n+1}) are computed, the discharges are updated by using (3.24).

Concerning properties related with mass, momentum and energy conservation when applying this projection technique, we shall add some comments. From the modelling point of view, when computing the energy balance in the depth-averaged model, the non-hydrostatic pressure term appears multiplied by the depth-integrated free-divergence condition, which ensures energy conservation. This projection method, similar to the Chorin-Témam projection [25, 71], ensures the incompressibility of the flow at discrete level, which is necessary to obtain a discrete energy balance (see [56]).

We shall also remark that the model includes conservative and non-conservative terms involving the non-hydrostatic pressure in the momentum equations. The discretization of the conservative counterpart ($\partial_x(hp_{\text{nh}})$) is also conservative at discrete level. On the other hand, the mass conservation is guaranteed since it is not affected by the projection technique, and a conservative finite volume method is used.

2.4 Numerical tests

2.4.1 Preliminaries

Unless otherwise specified, the following parameters will be used for the upcoming tests: $d_{\text{s}} = 1.13\times 10^{-3}\,\text{m}$, $\psi_0 = 0.4$, $\theta_{\text{c}} = 0.047$, $\rho_{\text{f}} = 1000\,\text{kg/m}^3$, $\rho_{\text{s}} = 2680\,\text{kg/m}^3$, $k_{\text{e}} = 0.096$, $k_{\text{d}} = 0.02$, and the Manning roughness coefficient $n = 0.02$. This value is selected because it typically represents an excavated or dredged earth channel that is straight, uniform, and relatively clean (see [27]). Furthermore, we will use the Meyer-Peter and Müller solid transport discharge for the equilibrium model case, and erosion and deposition rates given by [43] (also in [13, 38]), namely

$$D = v_{\text{s}}c_{\text{b}} \quad \text{and} \quad E = v_{\text{s}}\psi_0 E_{\text{s}}, \qquad (4.1)$$

where v_{s} is the settling velocity and c_{b} is the fractional concentration of suspended sediment near the bed, defined as

$$c_{\text{b}} = 0.4c(d_{\text{s}}/D_{\text{sg}})^{1.64} + 1.64c, \qquad (4.2)$$

where D_{sg} is the geometric mean diameter of suspended sediment particles. In the case of a single sediment type, (4.2) reduces to $c_{\text{b}} = 2.04c$. Furthermore, the settling velocity is expressed as

$$v_{\mathrm{s}} = \sqrt{\left(\frac{13.95\nu}{d_{\mathrm{s}}}\right)^2 + 1.09(r_{\mathrm{s}}-1)gd_{\mathrm{s}}} - \frac{13.95\nu}{d_{\mathrm{s}}}, \tag{4.3}$$

where ν is the kinematic viscosity ($\nu = 10^{-6}$) of water and E_{s} is the sediment entrainment coefficient, which is defined as

$$E_{\mathrm{s}} := \frac{1.3\times 10^{-7}Z^5}{1+4.3\times 10^{-7}Z^5} \quad \text{with} \quad Z := \begin{cases} \dfrac{\sqrt{c_{\mathrm{D}}}|u|}{v_{\mathrm{s}}}\mathrm{Re}^{0.6} & \text{if } \mathrm{Re} > 2.36, \\ 0.586\dfrac{\sqrt{c_{\mathrm{D}}}|u|}{v_{\mathrm{s}}}\mathrm{Re}^{1.23} & \text{if } \mathrm{Re} \le 2.36. \end{cases} \tag{4.4}$$

where c_{D} is the drag coefficient empirically defined as $c_{\mathrm{D}} = 24/\mathrm{Re}$, and Re is the Reynolds number for the particles:

$$\mathrm{Re} := \frac{d_{\mathrm{s}}\sqrt{(r_{\mathrm{s}}-1)gd_{\mathrm{s}}}}{\nu}. \tag{4.5}$$

Other definitions of these terms could be used in principle (see [1, 18, 59, 68] among others).

Unless specified, hydrostatic pressure is assumed, and the stability restriction

$$\Delta t = \mathrm{CFL}\frac{\Delta x}{\lambda},$$

with CFL= 0.5 is used, where $\lambda = \max_i |\lambda_i|$ is the spectral radius of $\hat{\boldsymbol{A}}_{i+1/2}$ (see (3.4)) in absolute value.

The tests include several alternatives for the models in this paper: equilibrium and non-equilibrium case, with/without gravitational effects, hydrostatic/non-hydrostatic pressure, erosion-deposition effects; as well as various methods (well-balanced and non-well-balanced). First, in Test 2.1, we compare the results of the proposed method with exact solutions derived for the equilibrium model with gravitational effects (see [40]) and then, in Test 2.2, with a novel exact solution introduced here for the non-equilibrium case. Next, Test 2.3 is an academic test that shows how the PVM-2I scheme reduces the numerical diffusion in comparison with HLL and Rusanov methods. After that, in Tests 2.4 to 2.6, results of the equilibrium model are compared with experimental data for classical scenarios, namely overtopping flow (Test 2.4) and dam-break configurations (Tests 2.5 and 2.6).

2.4.2 Example 2.1: sediment transport in equilibrium including gravitational effects

We test the proposed numerical scheme for the model in equilibrium without sediment in suspension, for which an exact solution accounting for gravitational effects in simple configurations is available (see [40]). Concretely, it is proven that if $(\zeta(x), Q_0, z_{\mathrm{b}}(x))$ denote the values

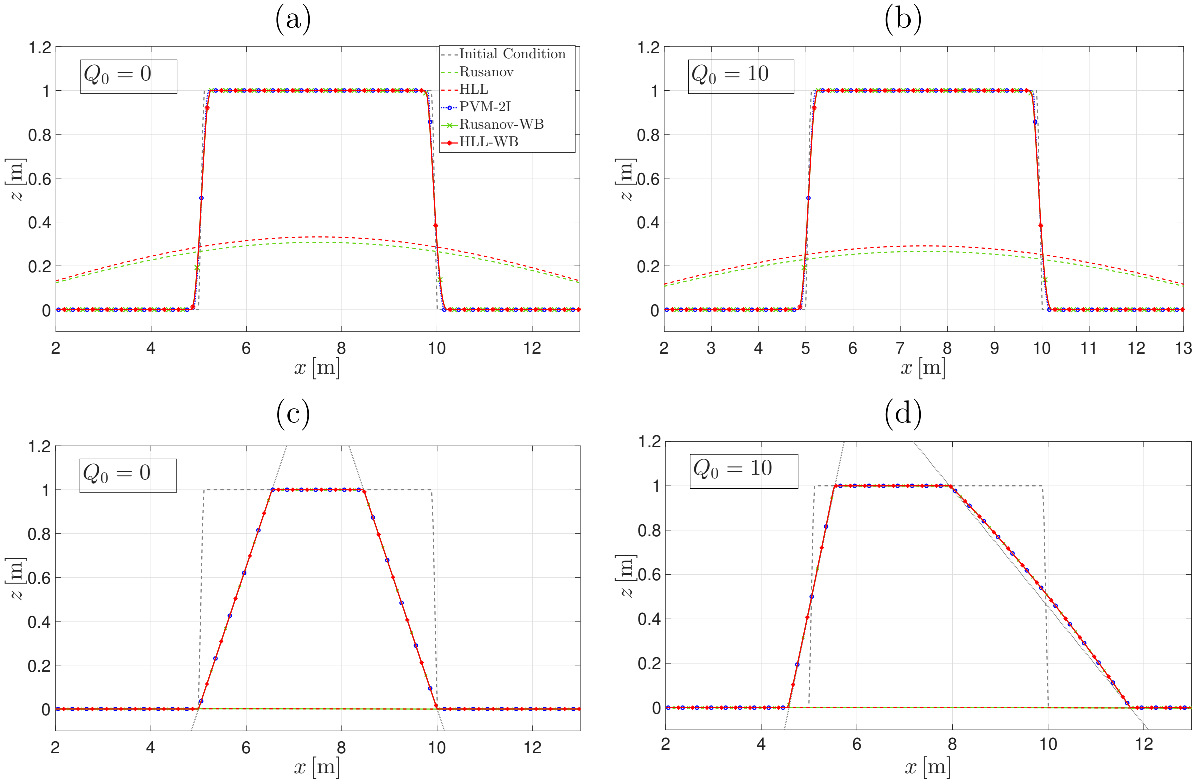

Figure 2.3: Test 2.1: approximate solutions $z_\mathrm{b}(x,t)$ for well-balanced and non-well-balanced methods (a, b) at simulated time $t = 100\,\mathrm{s}$ and (c, d) close to steady state obtained by using (a, c) $Q_0 = 0\,\mathrm{m}^2/\mathrm{s}$ and (b, d) $Q_0 = 10\,\mathrm{m}^2/\mathrm{s}$, for $\delta = 33°$.

of the free surface, discharge, and sediment layer satisfying that $q_\mathrm{b} = 0$, with $Q_0 = \text{const.}$, it is a steady solution of the equilibrium model if and only if

$$-\operatorname{sgn}(\tau_\text{eff})\beta\partial_x z_\mathrm{b} \leq \tan\delta\left(1 - \frac{\operatorname{sgn}(\tau_\text{eff})C_\mathrm{f}|Q_0|Q_0}{g d_\mathrm{s}\theta_\mathrm{c}(r_\mathrm{s}-1)h^2}\right), \quad \partial_x\zeta = \alpha\partial_x z_\mathrm{b}, \tag{4.6}$$

with $\alpha = -Q_0^2/(gh^3 - Q_0^2)$ and $\beta = 1 + \alpha/(r_\mathrm{s} - 1)$. As particular case, in the steady case ($Q_0 = 0$) the slope of the sediment matches the angle of repose of the material, and this steady slope varies with the constant discharge Q_0, so the slope remains stable without further erosion.

For this test, we consider the initial conditions

$$h(x,0) = 10\,\mathrm{m}, \quad hu(x,0) = Q_0\,\mathrm{m}^2/\mathrm{s}, \quad z_\mathrm{b}(x,0) = \begin{cases} 10\cdot(x-5)\,\mathrm{m} & \text{if } 5 < x \leq 5.1, \\ 1\,\mathrm{m} & \text{if } 5.1 < x \leq 9.9, \\ 10\cdot(10-x)\,\mathrm{m} & \text{if } 9.9 < x \leq 10, \\ 0\,\mathrm{m} & \text{otherwise,} \end{cases}$$

with a repose angle $\delta = 33°$ and where Q_0 is the constant flow discharge. Two configurations will be considered, the water-at-rest case ($Q_0 = 0\,\mathrm{m}^2/\mathrm{s}$) and a constant flow $Q_0 = 10\,\mathrm{m}^2/\mathrm{s}$. The spatial domain is $[0, 15]$ m with a grid spacing $\Delta x = 0.03\,\mathrm{m}$.

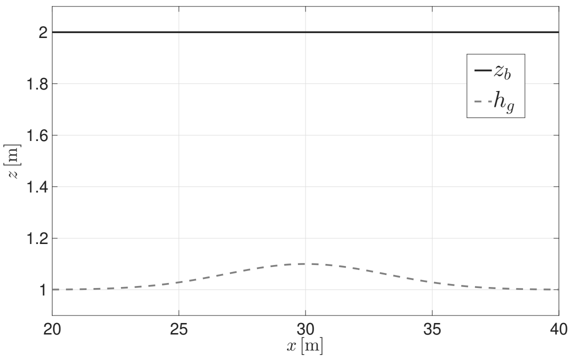

Figure 2.4: Test 2.2: initial condition for the erodible bed (z_b) and the fixed layer (h_g).

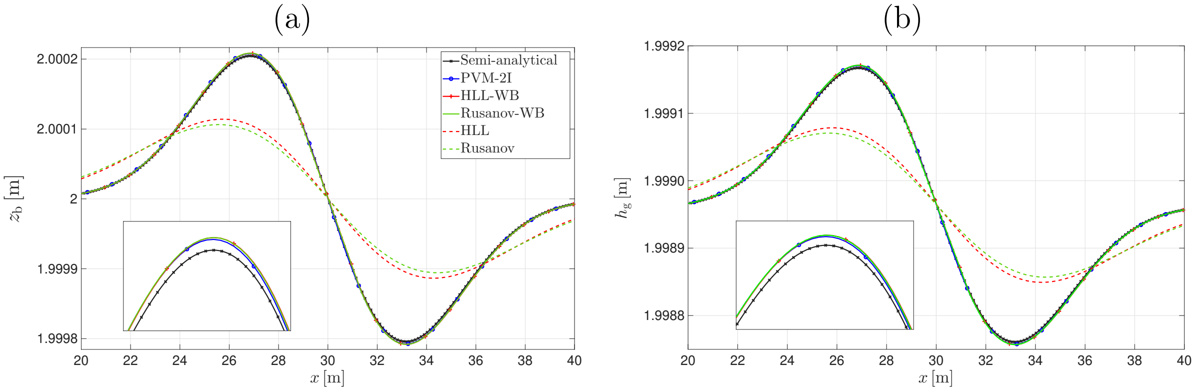

Figure 2.5: Test 2.2: comparisons of (a) the erodible bed z_b and (b) the fixed layer h_g for well-balanced and non-well-balanced methods at simulated time $t = 10\,\mathrm{s}$.

Figure 2.3 shows the numerical results. Figures 2.3(a) and (b) correspond to the results after 100 s of simulated time for different schemes, when the sediment has not reached its steady state yet. The well-balanced methods behave as expected, namely they slowly approximate the exact equilibrium solution, and thereby match the performance of PVM-2I, while the non-well-balanced Rusanov and HLL schemes degrade rapidly due to numerical viscosity. Figures 2.3(c) and (d) show the behaviour of the PVM-2I and the well-balanced Rusanov and HLL schemes close to steady state ($t = 200000\,\mathrm{s}$). In both cases, the numerical solution reproduces properly the exact one. The expected equilibrium profile is maintained successfully. On the contrary, non-well-balanced schemes are not able to reproduce these solutions due to numerical diffusion. In fact, notice that the lines corresponding to non-well-balanced Rusanov and HLL methods are nearly flat (close to $z = 0\,\mathrm{m}$) in the plots in figures 2.3(c) and (d).

2.4.3 Example 2.2: non-equilibrium model with exact solution

Here, we consider the non-equilibrium model with no gravitational effects and derive a novel exact solution in a simplified configuration, where both the flow depth $h(x, t)$ and the velocity $u(x,t)$ remain constant in space and time. First, we assume that there is no suspended sediment. Under these conditions, the Shields parameter $\theta(h,u)$ also remains constant, and therefore the bedload transport velocity v_b is spatially and temporally uniform. Consequently, the governing equation for the evolution of the mobile sediment layer thickness, h_m, simplifies to

$$\partial_t h_\mathrm{m} + a v_\mathrm{b} \partial_x h_\mathrm{m} = \dot{\eta}_\mathrm{e} - h_\mathrm{m} b \quad \text{with} \quad a := \frac{\sqrt{g d_\mathrm{s}(r_\mathrm{s}-1)}}{1-\psi_0} \quad \text{and} \quad b := \frac{\sqrt{g d_\mathrm{s}(r_\mathrm{s}-1)}k_\mathrm{d}}{d_\mathrm{s}}.$$

The previous equation is a transport equation with a source term. Its exact solution is given by

$$h_\mathrm{m}(x,t) = \frac{\dot{\eta}_\mathrm{e}}{b} + \left(h_{\mathrm{m},0}(x - a v_\mathrm{b} t) - \frac{\dot{\eta}_\mathrm{e}}{b} \right) \mathrm{e}^{-bt}, \tag{4.7}$$

where $h_{\mathrm{m},0}(x) = h_\mathrm{m}(x,0)$ is the initial condition. Thus, the term $h_{\mathrm{m},0}(x - a v_\mathrm{b} t)$ represents a wave propagating through the domain with velocity $a v_\mathrm{b}$. Roughly speaking, this wave propagates much more slowly than the rate at which its amplitude decays due to the exponential term. Furthermore, if $\theta \leq \theta_\mathrm{c}$, and hence $\dot{\eta}_\mathrm{e} = 0$, the wave remains stationary. The solution is exact under the assumption that $h(x,t)$, $u(x,t)$, $z_\mathrm{b}(x,t)$, and $h_{\mathrm{m},0}(x)$ remain constant. However, if $h_{\mathrm{m},0}(x)$ varies in space we get a semi-analytical solution. Actually, a non-uniform function $h_{\mathrm{m},0}(x)$ leads to a non-constant bed elevation $z_\mathrm{b}(x,t)$ given by the solution of

$$\partial_t z_\mathrm{b} = -a v_\mathrm{b} \partial_x h_\mathrm{m}. \tag{4.8}$$

Thus, variations in $h_{\mathrm{m},0}(x)$ induce deviations in $z_\mathrm{b}(x,t)$, and consequently, $h(x,t)$ and $u(x,t)$ are no longer strictly constant but small perturbations appear.

On the other hand, regardless of the initial condition $h_{\mathrm{m},0}(x)$, the system evolves towards an equilibrium state as $t \to \infty$, given by

$$h_\mathrm{m} = \frac{k_\mathrm{e}}{1-\psi_0} \frac{d_\mathrm{s}}{k_\mathrm{d}} (\theta - \theta_\mathrm{c})_+. \tag{4.9}$$

This implies that in the long time, the mobile sediment layer thickness stabilizes according to the equilibrium entrainment and deposition dynamics.

The solutions for the immobile sediment layer thickness h_g and bed elevation z_b are given by

$$h_\mathrm{g}(x,t) = h_{\mathrm{g},0}(x) + \frac{\dot{\eta}_\mathrm{e}}{b}(\mathrm{e}^{-bt} - 1) + b \int_0^t h_{\mathrm{m},0}(x - a v_\mathrm{b} \tau) \mathrm{e}^{-b\tau} \,\mathrm{d}\tau, \tag{4.10}$$

$$z_\mathrm{b}(x,t) = h_{\mathrm{g},0}(x) + h_{\mathrm{m},0}(x - a v_\mathrm{b} t)\mathrm{e}^{-bt} + b \int_0^t h_{\mathrm{m},0}(x - a v_\mathrm{b} \tau) \mathrm{e}^{-b\tau} \,\mathrm{d}\tau. \tag{4.11}$$

with $h_{\mathrm{g},0}(x) = h_\mathrm{g}(x,0)$. Assuming $a v_\mathrm{b} \ll b$, we approximate $h_{\mathrm{m},0}(x - a v_\mathrm{b} t) \approx h_{\mathrm{m},0}(x)$, which yields

$$h_\mathrm{g}(x,t) = h_{\mathrm{g},0}(x) + \left(h_{\mathrm{m},0}(x) - \frac{\dot{\eta}_\mathrm{e}}{b} \right)(1 - \mathrm{e}^{-bt}) + \mathcal{O}(a v_\mathrm{b}/b),$$

$$z_{\mathrm{b}}(x,t) = z_{\mathrm{b},0}(x) + \mathcal{O}(av_{\mathrm{b}}/b),$$

where $z_{\mathrm{b},0}(x) \coloneqq h_{\mathrm{g},0}(x) + h_{\mathrm{m},0}(x)$. This result suggests that z_{b} remains almost constant over time. By integrating by parts, we can further refine the solution. By using

$$b\int_0^t h_{\mathrm{m},0}(x - av_{\mathrm{b}}\tau)\mathrm{e}^{-b\tau}\,\mathrm{d}\tau = -h_{\mathrm{m},0}(x - av_{\mathrm{b}}\tau)\mathrm{e}^{-b\tau}\Big|_0^t - av_{\mathrm{b}}\int_0^t h'_{m,0}\mathrm{e}^{-b\tau}\,\mathrm{d}\tau,$$

where $h'_{\mathrm{m},0} \coloneqq \mathrm{d}h_{\mathrm{m},0}/\mathrm{d}z$ with $z = x - av_{\mathrm{b}}t$, and again assuming $av_{\mathrm{b}} \ll b$, we obtain the first-order correction

$$\begin{aligned}
h_{\mathrm{g}}(x,t) &= h_{\mathrm{g},0}(x) + \left(h_{\mathrm{m},0}(x) - \frac{\dot{\eta}_{\mathrm{e}}}{b} - \frac{av_{\mathrm{b}}}{b}h'_{\mathrm{m},0}(x)\right)(1 - \mathrm{e}^{-bt}) + \mathcal{O}((av_{\mathrm{b}}/b)^2),\\
z_{\mathrm{b}}(x,t) &= z_{\mathrm{b},0}(x) - \frac{av_{\mathrm{b}}}{b}h'_{\mathrm{m},0}(1 - \mathrm{e}^{-bt}) + \mathcal{O}((av_{\mathrm{b}}/b)^2).
\end{aligned}$$

These corrections might be systematically improved by iterating the integration-by-parts process.

In the case of sediment in suspension, which is not considered in this test, the solution generalizes as

$$h_{\mathrm{m}}(x,t) = \frac{d}{b} + \left(h_{\mathrm{m},0}(x - av_{\mathrm{b}}t) - \frac{d}{b}\right)\mathrm{e}^{-bt} \tag{4.12}$$

with

$$a \coloneqq \frac{\sqrt{gd_{\mathrm{s}}(r_{\mathrm{s}} - 1)}}{1 - \psi_0}, \quad b \coloneqq \frac{\sqrt{gd_{\mathrm{s}}(r_{\mathrm{s}} - 1)}k_{\mathrm{d}}}{d_{\mathrm{s}}}, \quad \text{and} \quad d \coloneqq \dot{\eta}_{\mathrm{e}} - \frac{E - D}{1 - \psi_0}.$$

We test the numerical scheme for the case without suspended sediment and with initial conditions

$$h(x,0) = 8\,\mathrm{m}, \quad hu(x,0) = 10\,\mathrm{m}^2/\mathrm{s}, \quad z_{\mathrm{b}}(x,0) = 2\,\mathrm{m}, \quad h_{\mathrm{g}}(x,0) = 1 + \frac{1}{10}\mathrm{e}^{-\frac{(x-30)^2}{20}}\,\mathrm{m}$$

We consider the domain $[0,60]\,\mathrm{m}$ with $\Delta x = 0.1\,\mathrm{m}$. This is a fast test, so $t = 10\,\mathrm{s}$ is sufficient time to study the behaviour of the solution and the schemes. The initial condition for z_{b} and h_{g} is depicted in Figure 2.4, and Figure 2.5 shows the comparison between semi-analytical and numerical solutions at $t = 10\,\mathrm{s}$. We see that the solutions of PVM-2I scheme and the well-balanced versions of HLL and Rusanov methods are in close agreement, demonstrating the accuracy of the numerical schemes. On the contrary, non-well-balanced methods exhibit non-physical erosion and fail to reach a steady state. The solution continues to erode on time, eventually flattening the bottom completely.

2.4.4 Example 2.3: “academic” dune transport

We highlight the accuracy of the PVM-2I scheme and the importance of using well-balanced methods by a simple academic test such as the transport of a simple dune. Moreover, under

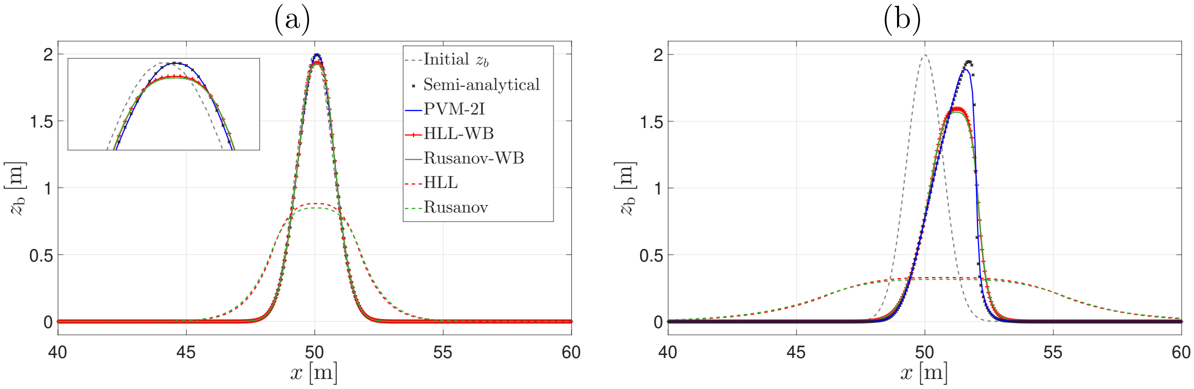

Figure 2.6: Test 2.3: solutions of the erodible bed (z_b) for well-balanced and non-well-balanced methods at simulated times (a) $t = 100\,\mathrm{s}$ and (b) $t = 2000\,\mathrm{s}$.

the assumption $h \gg z_\mathrm{b}$, one may assume the equilibrium regime for the system and

$$h = A - z_\mathrm{b}, \quad \text{and} \quad hu = \text{const.}, \tag{4.13}$$

where $A \in \mathbb{R}$ is a constant such that $A > z_\mathrm{b}$. These expressions can be replaced in the equations for z_b and h_g, which are subsequently solved numerically. So, we get an approximate semi-analytical solution. It is important to remark that the modified system exhibits eigenvalues that differ from the original ones.

Here we consider the initial conditions

$$h(x,0) = 10\, - z_\mathrm{b}(x,0)\ \mathrm{m}, \quad hu(x,0) = 10\,\mathrm{m}^2/\mathrm{s}, \quad z_\mathrm{b}(x,0) = 2\mathrm{e}^{-(x-50)^2}\ \mathrm{m},$$

and the Manning coefficient is taken here as $n = 0.05$ to increase the transport rate and exhibit the differences between the various schemes. The simulation domain spans $[0, 100]\,\mathrm{m}$ with spatial resolution $\Delta x = 0.02\,\mathrm{m}$.

Figure 2.6 shows the dune evolution at simulated times $t = 100\,\mathrm{s}$ and $t = 2000\,\mathrm{s}$ along with the approximate semi-analytical solution. On the one hand, the numerical solution of the PVM-2I scheme is the closest to the semi-analytical reference solution. This property highlights its accuracy to reproduce the sediment evolution compared to the well-balanced Rusanov and HLL schemes, where we recall that these schemes are identical for the equations of fluid variables. We observe that the non-well-balanced schemes do not reproduce these solutions as a consequence of numerical diffusion. This behaviour lends further support to the proposed well-balanced correction and serves as a strong validation of the proposed PVM-2I scheme for such problems. On the other hand, the schemes Rusanov-WB and HLL-WB, although they are more diffusive than PVM-2I, acceptably approximate the dune evolution. The main advantage of the Rusanov-WB and HLL-WB schemes is that they are conceptually simpler and accurate methods, and therefore both are potential candidates for the construction of high-order methods when combined with high-order techniques such as reconstruction of states (see [20]).

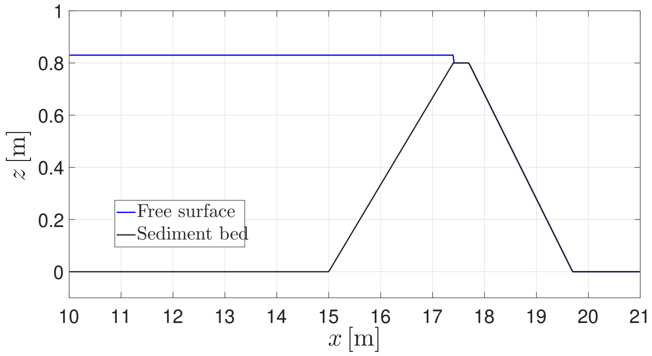

Figure 2.7: Test 2.4: initial condition for the free surface ($z_{\text{b}} + h$) and sediment bed (z_{b}) in the experiment of [72].

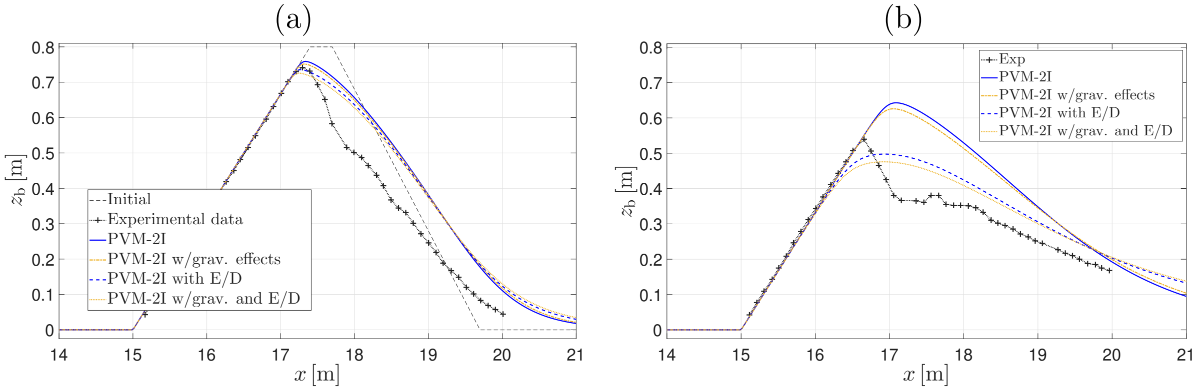

Figure 2.8: Test 2.4: comparison of experimental data of bed evolution (black with symbols lines) ([72]) at (a) $t = 30\,\text{s}$ and (b) $t = 60\,\text{s}$ with results of the equilibrium model with PVM-2I method with and without erosion/deposition (E/D) terms (dashed and continuous lines, respectively), with and without gravitational effects (brown and blue lines, respectively).

2.4.5 Example 2.4: overtopping flow erosion

We now compare our numerical results with experimental data in [72] for an overtopping flow erosion process. The experimental setup consists of a rectangular channel of length 30 m and width 0.3 m wide including a trapezoidal sediment dam. A constant incoming flow (1.23 liters per second) is imposed upstream, and the flow starts to erode the sediment bed. Erosion/deposition effects are not considered here so that we may directly compare the effects of numerical dissipation over erosion. It is worth mentioning that some references apply the sediment transport but not erosion/deposition while others consider just erosion/deposition effects; cf., e.g., [2, 51].

As domain we take $[0, 25]\,\text{m}$ with $\Delta x = 0.01\,\text{m}$, and the initial conditions (see Figure 2.7) are

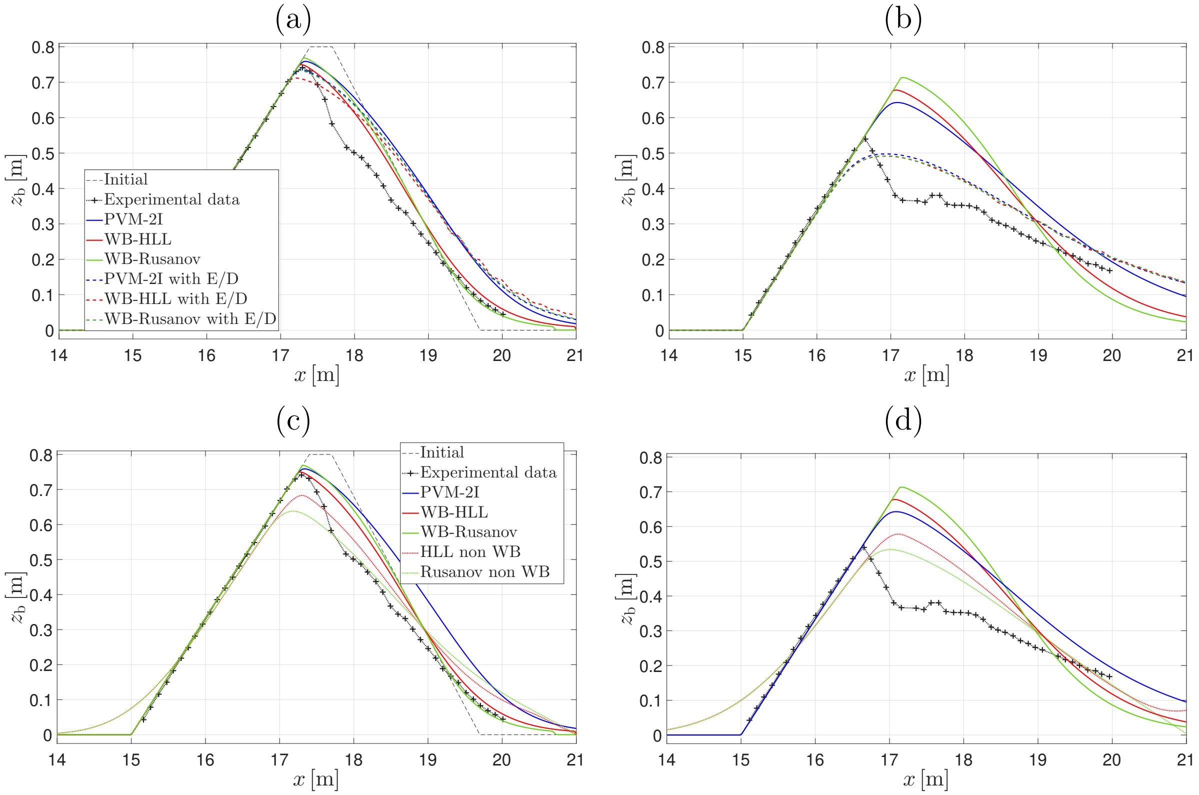

Figure 2.9: Test 2.4: Comparison of bed evolution experimental data (black with symbols lines) ([72]) at (a, c) $t = 30\,\mathrm{s}$ and (b, d) $t = 60\,\mathrm{s}$ with results of the equilibrium model with PVM-2I, Rusanov, and HLL methods (blue, green, and red lines, respectively). Plots (a, b): comparison of the results with and without erosion/deposition (E/D) terms (dashed and continuous lines); plots (c, d): comparison of the results of well-balanced and non-well-balanced numerical methods (dashed and continuous lines, respectively).

given by

$$h(x,0) = \begin{cases} 0.83\,\mathrm{m} & \text{if } x \leq 17.4, \\ 0\,\mathrm{m} & \text{if } x > 17.4 \end{cases}, \quad hu(x,0) = 1.23 \times 10^{-3}\,\mathrm{m}^2/\mathrm{s},$$

$$z_\mathrm{b}(x,0) = \begin{cases} (x-15)/3\ \mathrm{m} & \text{if } 15 < x \leq 17.4, \\ 0.8\,\mathrm{m} & \text{if } 17.4 < x \leq 17.7, \\ 0.8 + (x-17.7)/2.5\ \mathrm{m} & \text{if } 17.7 < x < 19.7, \\ 0\,\mathrm{m} & \text{otherwise.} \end{cases}$$

In this case, we use as porosity $\psi_0 = 0.35$. Concerning the Manning roughness coefficient, in [72], it was determined by trial and error to be $n = 0.018$ during calibration of their model against experimental dam-break data. For our model, we find that a slightly lower value of $n = 0.015$ provides a better agreement with the measured water surface profiles and flow

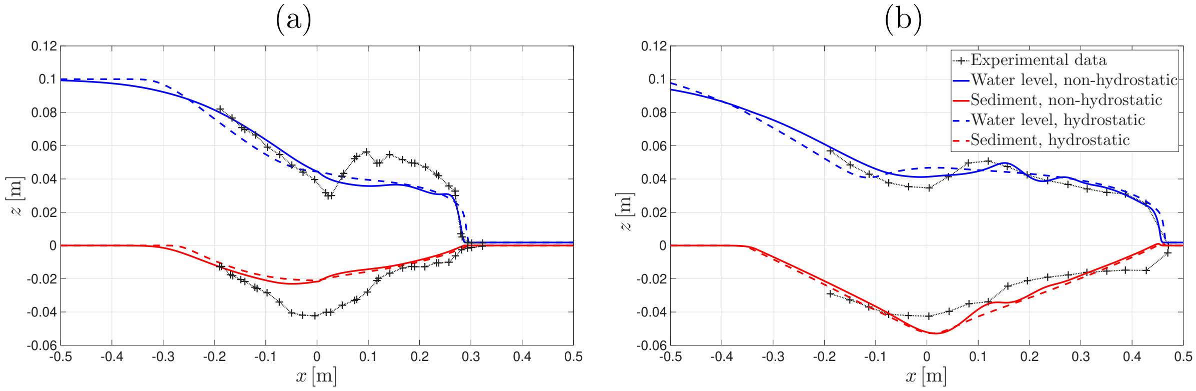

Figure 2.10: Test 2.5: comparison between experimental data [19] and numerical results for models with hydrostatic and non-hydrostatic pressure at simulated times (a) $t = 3t_0$ and (b) $t = 5t_0$, where $t_0 = \sqrt{h_0/g}$ and h_0 is the initial water level before the dam break.

velocities. Moreover, following the Manning-Strickler relation, $n = d_{90}^{1/6}/26$ (see [53]), we obtain $n = 0.015$ since $d_{90} = 3.8 \times 10^{-3}$ m for this test. We compare here the results of the equilibrium model.

For this test, gravitational effects do not have a significant influence on the results, as it is shown in Figure 2.8. This outcome is partly due to the choice of the test slope smaller than the repose angle of 25°, which reduces the influence of gravitational forces on the overall behaviour of the system.

In Figure 2.9(b) the influence of erosion and deposition (E/D) terms is depicted. We observe that the results are close to the experimental data when erosion/deposition terms are activated. Figure 2.9(c) shows a comparison between the standard Rusanov and HLL solvers and their well-balanced versions as well as PVM-2I scheme for the model without erosion/deposition terms. As it is shown, the standard Rusanov and HLL methods produce a faster erosion than the well-balanced versions. This indicates the presence of non-physical erosion in some regions. Although this additional erosion might locally resemble the experimental data at $t = 60\,\mathrm{s}$, it is incorrect and cannot be controlled.

2.4.6 Examples 2.5 and 2.6: dam-break problems

In these tests, we reproduce some dam-break experiments reported in [19] and [64]. Dam-break test cases, such as the ones performed here, involve rapid erosion, and conventional sediment transport formulations usually do not properly capture its dynamics. For this reason, we omit the sediment transport (advection) term from the equations ($q_\mathrm{b} = 0$) in these tests, which allows us to isolate and analyse the contribution of local bed changes driven solely by erosion and deposition.

Test 2.5 is based on the experiments conducted in [19] that correspond to the initial condition

$$h(x,0)=\begin{cases}0.1\,\mathrm{m} & \text{if } x\le 0,\\ 0\,\mathrm{m} & \text{otherwise}\end{cases},\quad z_{\mathrm{b}}(x,0)=0\,\mathrm{m},\quad hu(x,0)=0\,\mathrm{m}^2/\mathrm{s},\quad c(x,0)=0. \tag{4.14}$$

The test configuration is a dam break over a low density sediment bottom. The parameters are the fluid density $\rho = 1000\,\mathrm{kg/m}^3$, the sediment density $\rho_{\mathrm{s}} = 1048\,\mathrm{kg/m}^3$, and the particle diameter $d_{\mathrm{s}} = 6.1\times 10^{-3}\,\mathrm{m}$. Gravitational effects are not included in this test, as their influence on the results was found to be negligible. We focus on the influence of non-hydrostatic effects on the results. The computational domain $[-1,1]\,\mathrm{m}$ is discretized using a uniform grid spacing $\Delta x = 0.001\,\mathrm{m}$.

Figure 2.10 shows the comparison between simulations with and without non-hydrostatic pressure and experimental measurements. As it is observed, the inclusion of non-hydrostatic pressure improves slightly the ability of the model to capture the physical behaviour of the flow, in particular the water level. Notice that the effect of non-hydrostatic pressures becomes more significant over time; initially, the impact is minimal, but it becomes more pronounced at later stages.

Test 2.6 is related to a similar experiment setup presented in [64]. In this experiment, the sediment properties are $d_{\mathrm{s}} = 3.9\times 10^{-3}\,\mathrm{m}$, $\rho_{\mathrm{s}} = 1580\,\mathrm{kg/m}^3$, and porosity $\psi_0 = 0.47$. The roughness coefficient is specified as $n = 0.0165$. The simulation was carried out for a total time of $T_{\mathrm{f}} = 1.5\,\mathrm{s}$. The computational domain for this experiment is defined as $[-3,3]\,\mathrm{m}$, which is discretized with $\Delta x = 0.001\,\mathrm{m}$. The initial conditions are given by

$$h(x,0)=\begin{cases}0.35\,\mathrm{m} & \text{if } x\le 0,\\ 0\,\mathrm{m} & \text{otherwise}\end{cases},\quad hu(x,0)=0\,\mathrm{m}^2/\mathrm{s},\quad c(x,0)=0,\quad z_{\mathrm{b}}(x,0)=0\,\mathrm{m}. \tag{4.15}$$

Figure 2.11 shows only minor differences between the model with and without non-hydrostatic pressure at both time steps. While bottom erosion appears nearly identical in both cases, the non-hydrostatic model captures the water level slightly more accurately on the left side.

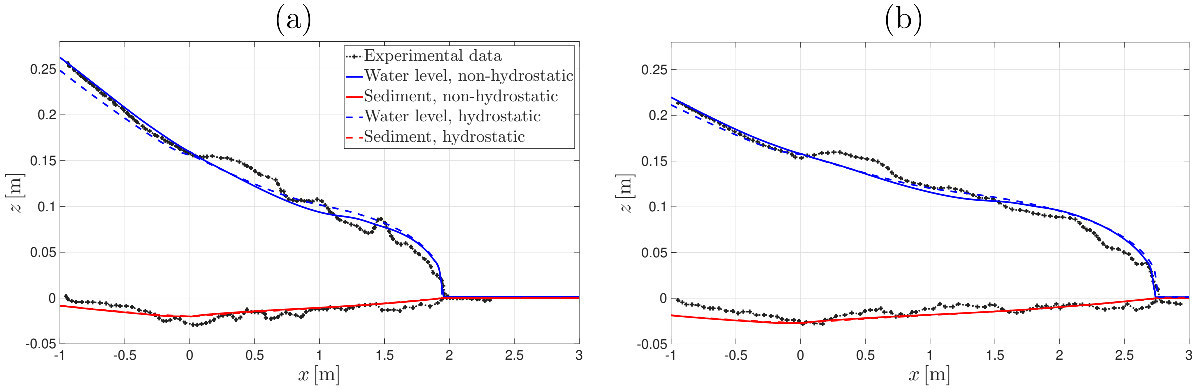

Figure 2.11: Test 2.6: comparison between experimental data ([64]) and numerical results for models with hydrostatic and non-hydrostatic pressure at simulated times (a) $t = 1\,\mathrm{s}$ and (b) and $t = 1.5\,\mathrm{s}$.

CHAPTER 3

A model of tsunami-forest interaction in two horizontal space dimensions

3.1 Introduction

The propagation of tsunamis over coastal regions covered by vegetation is a complex phenomenon involving strong interactions between the incoming wave, the fluid motion within the vegetated layer, and the underlying bathymetry. The accurate representation of these processes is crucial for understanding natural coastal protection mechanisms and for improving predictive models used in risk assessment and mitigation strategies.

Depth-averaged models based on the classical Saint–Venant equations are widely employed for tsunami simulations due to their simplicity and computational efficiency. However, their hydrostatic assumption limits their ability to capture vertical accelerations, dispersive effects, and interactions with complex obstacles such as vegetation. To overcome these limitations, various non-hydrostatic and multilayer extensions of the shallow-water equations have been proposed in recent decades (see, for example, [9, 34]). These formulations account for vertical structure and pressure deviations from the hydrostatic profile, providing a more accurate description of free-surface dynamics.

In [14], a one-dimensional multilayer non-hydrostatic model was developed to study the attenuation of tsunami waves by coastal forests. That work introduced a finite volume–projection method capable of handling non-hydrostatic pressures, wet–dry interfaces, and vegetation-induced drag, inertia, and porosity effects in a consistent manner. Despite its robustness and physical accuracy, the model was limited to one spatial dimension, thus neglecting lateral variations and directional effects in the flow field.

The present work extends that approach to two horizontal dimensions, leading to a two-dimensional multilayer non-hydrostatic shallow-water model for tsunami–forest interaction. The new formulation describes the depth-averaged motion of each layer over the (x, y) plane, incorporating non-hydrostatic pressure corrections, anisotropic vegetation effects, and complex bathymetry. This extension enables the simulation of realistic tsunami propagation patterns, including wave diffraction, channeling between vegetated patches, and spatially varying attenuation across the coastal zone.

The governing equations are discretized using a finite volume method coupled with a projection step for the non-hydrostatic pressure. The scheme maintains well-balancedness, ensures positivity of the water depth, and accurately treats dry–wet interfaces. Vegetation effects are modeled through drag and porosity tensors that vary spatially, allowing the representation of heterogeneous forest distributions. Numerical experiments demonstrate the model's capability to reproduce laboratory and field-scale observations, highlighting its potential as a predictive tool for coastal protection analysis.

This chapter is organized as follows. Section 3.2 introduces the governing equations of the two-dimensional multilayer non-hydrostatic system. Section 3.3 describes the numerical method, including the finite volume discretization and the pressure projection step. Section 3.4 presents numerical experiments assessing the performance of the proposed scheme.

3.2 Governing equations

We consider an incompressible, homogeneous fluid with a free surface elevation $\eta(x, y, t)$ over a bottom topography $z_b(x, y)$. The total water depth is defined as $h(x, y, t) = \eta(x, y, t) - z_b(x, y)$. The flow domain is vertically discretized into N layers of variable thickness $h_\alpha(x, y, t)$, satisfying

$$h = \sum_{\alpha=1}^{N} h_\alpha.$$

We denote by $\alpha + 1/2$ the interface between layers α and $\alpha + 1$ as it is shown in Figure 1.3. The vertical position of this interface is then given by

$$z_{\alpha+1/2} = z_b + \sum_{\beta=1}^{\alpha} h_\beta.$$

Each layer is characterized by a depth-averaged horizontal velocity $\boldsymbol{u}_\alpha = (u_\alpha, v_\alpha)^{\mathrm{T}}$, a representative vertical velocity w_α, and a non-hydrostatic pressure correction q_α that accounts for deviations from hydrostatic equilibrium.

The governing equations for layer α read

$$\partial_t h_\alpha + \nabla \cdot (h_\alpha \boldsymbol{u}_\alpha) = \Gamma_{\alpha+1/2} - \Gamma_{\alpha-1/2}, \tag{2.1}$$

$$\partial_t (h_\alpha \boldsymbol{u}_\alpha) + \nabla \cdot (h_\alpha \boldsymbol{u}_\alpha \otimes \boldsymbol{u}_\alpha) + g h_\alpha \nabla h = -g h_\alpha \nabla z_{\mathrm{b}} - \tau - \boldsymbol{F}_\alpha^{\mathrm{nh}} - \boldsymbol{S}_\alpha^{\mathrm{veg}}, \tag{2.2}$$

where $\nabla = (\partial_x, \partial_y)^{\mathrm{T}}$ is the horizontal gradient operator, $\mathbf{I}$ is the identity matrix, and $\Gamma_{\alpha\pm1/2}$ represent mass exchanges between adjacent layers due to vertical velocity.

In the momentum balance (2.2), the term $\boldsymbol{\tau}$ denotes the drag force induced by bottom friction, $\boldsymbol{F}_\alpha^{\mathrm{nh}}$ accounts for the non-hydrostatic pressure correction, and $\boldsymbol{S}_\alpha^{\mathrm{veg}}$ represents the vegetation-induced forces, including drag, inertia, and porosity effects. Together, these contributions describe the horizontal dynamics of each layer within the multilayer structure.

The non-hydrostatic correction $\boldsymbol{F}_\alpha^{\mathrm{nh}}$ is given by

$$\boldsymbol{F}_\alpha^{\mathrm{nh}} = \nabla z_{\alpha+1/2}\, q_{\alpha+1/2} - \nabla z_{\alpha-1/2}\, q_{\alpha-1/2} - \nabla\big(h_\alpha q_\alpha\big),$$

where q_α is the non-hydrostatic pressure in the middle of the layer.

The vegetation source term $\mathbf{S}_\alpha^{\mathrm{veg}}$ accounts for the resistance offered by stems, trunks, or roots distributed over the computational domain. It can be expressed as

$$\boldsymbol{S}_\alpha^{\mathrm{veg}} = \boldsymbol{f}_{\mathrm{D},\alpha} + \boldsymbol{f}_{\mathrm{M},\alpha} \tag{2.3}$$

with

$$\boldsymbol{f}_{\mathrm{D},\alpha} = C_{\mathrm{D}}\, \rho\, \theta_\alpha\, |\boldsymbol{u}_\alpha|\, \boldsymbol{u}_\alpha \quad \text{and} \quad \boldsymbol{f}_{\mathrm{M},\alpha} = C_{\mathrm{I}}\, \rho\, \theta_\alpha\, \partial_t \boldsymbol{u}_\alpha,$$

where C_{D} and C_{I} are the drag and inertia coefficients, ρ is the fluid density, and θ_α is a porosity.

At the free surface ($\alpha = N$) and at the bottom ($\alpha = 1$), the following boundary conditions are imposed:

$$\Gamma_{N+1/2} = \Gamma_{1/2} = 0,$$

ensuring mass conservation across the boundaries.

Summing (2.1) over all layers yields the total depth-integrated continuity equation:

$$\frac{\partial h}{\partial t} + \nabla \cdot (h\boldsymbol{u}) = 0,$$

where $\boldsymbol{u}$ is defined as

$$\boldsymbol{u} := \sum_{1}^{\alpha} \frac{h_\alpha \boldsymbol{u}_\alpha}{h}$$

This relation, together with (2.2), forms the basis of the proposed multilayer non-hydrostatic model for two-dimensional free-surface flows.

3.2.1 Two-dimensional multilayer LDNH_0 model

We extend the 1D multilayer model [14] to two horizontal dimensions $\mathbf{x} = (x, y)$.

The 2D multilayer LDNH$_0$ system reads, for each layer α,

$$\partial_t h + \frac{1}{\bar{\theta}}\nabla\cdot(h\boldsymbol{u}) = 0, \tag{2.4a}$$

$$\begin{aligned}\partial_t\big(h_\alpha\boldsymbol{u}_\alpha\big) + \frac{\nabla\cdot\big(h_\alpha\boldsymbol{u}_\alpha\otimes\boldsymbol{u}_\alpha\big)}{\theta_\alpha} + \theta_\alpha\nabla\big(h_\alpha q_\alpha\big) - \theta_\alpha\nabla z_{\alpha+1/2}\, q_{\alpha+1/2} + \theta_\alpha\nabla z_{\alpha-1/2}\, q_{\alpha-1/2}\\ = -g h_\alpha\theta_\alpha\nabla\eta + \frac{\widetilde{\boldsymbol{u}}_{\alpha+1/2}\,\Gamma_{\alpha+1/2}}{\theta_\alpha} - \frac{\widetilde{\boldsymbol{u}}_{\alpha-1/2}\,\Gamma_{\alpha-1/2}}{\theta_\alpha} - \boldsymbol{f}_{\mathrm{D},\alpha} - \boldsymbol{f}_{\mathrm{M},\alpha} + \frac{\mathbf{K}_{\alpha-1/2}}{\theta_\alpha} - \frac{\mathbf{K}_{\alpha+1/2}}{\theta_\alpha},\end{aligned} \tag{2.4b}$$

$$\partial_t\big(h_\alpha w_\alpha\big) + \frac{\nabla\cdot\big(h_\alpha w_\alpha\boldsymbol{u}_\alpha\big)}{\theta_\alpha} + q_{\alpha+1/2} - q_{\alpha-1/2} = \frac{\widetilde{w}_{\alpha+1/2}\,\Gamma_{\alpha+1/2}}{\theta_\alpha} - \frac{\widetilde{w}_{\alpha-1/2}\,\Gamma_{\alpha-1/2}}{\theta_\alpha}, \tag{2.4c}$$

together with the (layer-wise) incompressibility generalizing (2.9d):

$$\nabla\cdot\boldsymbol{u}_\alpha \;+\; 2\,\frac{w_\alpha - \boldsymbol{u}_\alpha\cdot\nabla z_b}{h_\alpha} \;=\; 0, \qquad \alpha = 1,\ldots,N. \tag{2.5}$$

Notation and interface quantities. The term $\Gamma_{\alpha+1/2}(\mathbf{x},t)$ represents the mass exchange from layer α to layer $\alpha+1$, taken as positive in the upward direction. It is defined as

$$\Gamma_{\alpha+1/2} = \sum_{\beta=1}^{N}\gamma_{\alpha,\beta}\nabla\cdot(h_\beta\boldsymbol{u}_\beta), \quad \text{where} \quad \gamma_{\alpha,\beta} := \begin{cases} 1-\displaystyle\sum_{k=1}^{\alpha}\frac{\theta_k}{N\bar{\theta}}, & \text{for } \alpha\geq\beta,\\ -\displaystyle\sum_{k=1}^{\alpha}\frac{\theta_k}{N\bar{\theta}}, & \text{for } \alpha<\beta.\end{cases}$$

The interface velocities $\widetilde{\boldsymbol{u}}_{\alpha\pm1/2}$ and $\widetilde{w}_{\alpha\pm1/2}$ correspond to averages at the interfaces and are given by

$$\widetilde{\boldsymbol{u}}_{\alpha+1/2} = \frac{\boldsymbol{u}_\alpha + \boldsymbol{u}_{\alpha+1}}{2}, \qquad \widetilde{w}_{\alpha+1/2} = \frac{w_\alpha + w_{\alpha+1}}{2}.$$

Finally, the quantities $\mathbf{K}_{\alpha\pm1/2}$ denote the viscous or momentum transfer terms between adjacent layers. These terms are vector quantities in two dimensions and generalize the scalar interlayer transfer terms $K_{\alpha\pm1/2}$ used in the one-dimensional formulation.

The bottom friction force $\boldsymbol{\tau}_\alpha$ acts only on the lowest layer ($\alpha = 1$), representing the shear stress between the fluid and the ground. It is defined as

$$\boldsymbol{\tau}_\alpha := k_{1,\alpha}\,\|h_\alpha\boldsymbol{u}_\alpha\|\,h_\alpha\boldsymbol{u}_\alpha = \begin{cases}\dfrac{g\,n^2\,\|\boldsymbol{u}_1\|\,\boldsymbol{u}_1}{\theta_1\,h_1^{1/3}}, & \text{for } \alpha = 1,\\ \mathbf{0}, & \text{for } \alpha = 2,\ldots,N,\end{cases} \tag{2.6}$$

where n is the Manning coefficient and θ_α denotes the layer porosity.

The upper layers are not directly affected by this bottom friction. However, the shear stress generated at the ground is transmitted upward through the internal viscosity of the fluid. This process is modeled by introducing interlayer viscous coupling terms $\mathbf{K}_{\alpha\pm1/2}$, defined as

$$\mathbf{K}_{\alpha+1/2} := -\eta_0\,\frac{\boldsymbol{u}_{\alpha+1} - \boldsymbol{u}_\alpha}{h_{\alpha+1} + h_\alpha}, \tag{2.7}$$

where η_0 is the dynamic viscosity coefficient. The boundary conditions at the interfaces are

$$\mathbf{K}_{N+1/2} = \mathbf{0}, \qquad \mathbf{K}_{1/2} = -\boldsymbol{\tau}_1.$$

These viscous terms represent the vertical transfer of horizontal momentum between neighboring layers. In the general case, η_0 could depend on depth, turbulence, or sediment concentration (see, e.g., [31]), but here it is assumed constant for simplicity.

3.2.2 Forest forces in the multi-layer system

Vegetation effects are introduced layer-wise by means of layer-specific geometric and vegetation averages. As in the one-dimensional formulation (Section 1.4.5), let $d(\zeta)$ denote the tree diameter at height ζ measured from the bed z_b, and let $c_\mathrm{tr}(\zeta)$, $c_\mathrm{le}(\zeta)$ be the trunk- and leaf-shape factors. For each layer α we define the layer-averaged diameter and vegetation coefficient by

$$\bar{d}_\alpha \;=\; \frac{1}{h_\alpha}\int_{z_{\alpha-1/2}-z_\mathrm{b}}^{z_{\alpha+1/2}-z_\mathrm{b}} d(\zeta)\,\mathrm{d}\zeta, \qquad (\overline{c_\mathrm{tr}c_\mathrm{le}})_\alpha \;=\; \frac{1}{h_\alpha}\int_{z_{\alpha-1/2}-z_\mathrm{b}}^{z_{\alpha+1/2}-z_\mathrm{b}} c_\mathrm{tr}(\zeta)\,c_\mathrm{le}(\zeta)\,\mathrm{d}\zeta. \tag{2.8}$$

The effective frontal area and transverse area of a single tree in layer α are then

$$A_{\mathrm{v},\alpha} \;=\; h_\alpha\,\bar{d}_\alpha, \qquad A_{\mathrm{t},\alpha} \;=\; \frac{\pi\bar{d}_\alpha^2}{4}.$$

Following the experimental parametrization used in the one-dimensional study, we introduce a base (Reynolds-dependent) drag coefficient $C_D(\mathrm{Re})$ according to [60]:

$$C_D(\mathrm{Re}) = \begin{cases} 1.2, & \mathrm{Re} \le 2\times 10^5, \\ 1.2 - 0.5\left(\dfrac{\mathrm{Re}}{3\times 10^5} - \dfrac{2}{3}\right), & 2\times 10^5 < \mathrm{Re} \le 5\times 10^5, \\ 0.7, & \mathrm{Re} > 5\times 10^5, \end{cases} \tag{2.9}$$

where the layer Reynolds number is computed with the layer velocity magnitude:

$$\mathrm{Re}_\alpha \;=\; \frac{\|\boldsymbol{u}_\alpha\|\,\bar{d}_\alpha}{\nu}, \qquad \nu = 1.19\times 10^{-6}\,\mathrm{m}^2/\mathrm{s}, \tag{2.10}$$

where ν is the kinematic viscosity of water. The layer-specific drag coefficient used in the drag force is the base coefficient modulated by the trunk/leaf factor, i.e.

$$C_{\mathrm{D},\alpha} \;=\; C_\mathrm{D}(\mathrm{Re}_\alpha)\;(\overline{c_\mathrm{tr}c_\mathrm{le}})_\alpha. \tag{2.11}$$

Next, we define the layer-wise effective tree density and porosity. Let n denote the number of trees per unit length in the streamwise direction (as in the 1D setup) and A_F the forest cross-sectional area used to non-dimensionalize densities. Then the effective tree density for layer α is taken as

$$n_{t,\alpha} \;=\; \frac{\bar{d}_\alpha\, m\, (\overline{c_{\mathrm{tr}} c_{\mathrm{le}}})_\alpha}{A_F}, \tag{2.12}$$

with m the trees density. Then, the layer porosity is defined by

$$\theta_\alpha \;=\; 1 - \frac{n_{t,\alpha}\, \pi \bar{d}_\alpha^2}{4}. \tag{2.13}$$

With these definitions the vectorial drag force per unit horizontal area acting on layer α reads

$$\boldsymbol{f}_{\mathrm{D},\alpha} \;=\; \frac{n_{t,\alpha}}{\theta_\alpha^2}\, \frac{1}{2}\, \rho\, C_{D,\alpha}\, A_{\mathrm{v},\alpha}\, \|\boldsymbol{u}_\alpha\|\, \boldsymbol{u}_\alpha \;=\; \frac{1}{2}\, \rho\, \frac{n_{t,\alpha}}{\theta_\alpha^2}\, C_D(\mathrm{Re}_\alpha)\, (\overline{c_{\mathrm{tr}} c_{\mathrm{le}}})_\alpha\, \bar{d}_\alpha\, \|\boldsymbol{u}_\alpha\|\, \boldsymbol{u}_\alpha. \tag{2.14}$$

Similarly, assuming radial symmetry of trunks, the inertia force per unit horizontal area is given by

$$\boldsymbol{f}_{\mathrm{M},\alpha} \;=\; C_{M,\alpha}\, \frac{n_{t,\alpha}}{\theta_\alpha}\, h_\alpha\, A_{\mathrm{t},\alpha}\, \partial_t \boldsymbol{u}_\alpha \;=\; C_{\mathrm{M},\alpha}\, \frac{n_{t,\alpha}}{\theta_\alpha}\, h_\alpha\, \frac{\pi \bar{d}_\alpha^2}{4}\, \partial_t \boldsymbol{u}_\alpha, \tag{2.15}$$

where we adopt the calibration $C_{\mathrm{M},\alpha} = 2$ from [70].

3.3 Numerical implementation for the multi-layer tsunami model

To advance the multilayer model from t^ν to $t^{\nu+1} = t^\nu + \Delta t$, we adopt a *fractional-step algorithm* that separates the computation into three substeps: (i) a hydrostatic prediction, (ii) a friction and inertia correction, and (iii) a non-hydrostatic projection. These substeps correspond to intermediate times ν, $\nu + 1/3$, $\nu + 2/3$, $\nu + 1$. For simplicity, at each stage the preceding state is denoted by an asterisk $(*)$.

Each stage preserves key physical constraints: positivity of the water depth, well-balancedness for the lake-at-rest state, and stability across wet/dry interfaces.

Compact formulation

For each layer $\alpha = 1, \ldots, N$, we denote the conservative variables as

$$\boldsymbol{W_\alpha} = (h_\alpha,\, h_\alpha \boldsymbol{u}_\alpha,\, h_\alpha w_\alpha)^{\mathrm{T}}, \qquad \boldsymbol{W} = (\boldsymbol{W}_1, \ldots, \boldsymbol{W}_N)^{\mathrm{T}}.$$

The governing multilayer system can then be written in compact form as

$$\partial_t \boldsymbol{W} + \nabla \cdot \boldsymbol{F}(\boldsymbol{W}) = -\,\boldsymbol{B}(\boldsymbol{W})\, \nabla \boldsymbol{W} + \boldsymbol{S}(\boldsymbol{W}), \tag{3.1}$$

where $\boldsymbol{F}(\boldsymbol{W})$ collects the advective fluxes, $\boldsymbol{B}(\boldsymbol{W})$ contains the non-conservative hydrostatic and interfacial transfer terms, and $\boldsymbol{S}(\boldsymbol{W})$ includes bed slope and frictional forces.

The *layer fluxes* are defined as

$$\boldsymbol{F}_\alpha(\boldsymbol{W}_\alpha) = \begin{pmatrix} h_\alpha \boldsymbol{u}_\alpha \\ h_\alpha \boldsymbol{u}_\alpha \otimes \boldsymbol{u}_\alpha + \frac{1}{2} g h_\alpha^2 \mathbf{1}_{2\times 2} \\ h_\alpha w_\alpha \boldsymbol{u}_\alpha \end{pmatrix},$$

with the interfacial coupling terms contained in $\boldsymbol{B}(\boldsymbol{W})$. Vertical transfers $\Gamma_{\alpha\pm 1/2}$ enforce mass and momentum continuity between layers.

Incorporation of inertia effects

In tsunami propagation and run-up, high Froude number flows make the inertia forces non-negligible. Following the approach in [14], these effects can be incorporated for each layer α by multiplying the system (3.1) by the *inertia matrix*

$$\boldsymbol{\mathcal{M}}_\alpha = \begin{bmatrix} 1 & \mathbf{0}_{1\times 2} & 0 \\ -\boldsymbol{u}_\alpha k_{3,\alpha} & (1+k_{3,\alpha})\boldsymbol{I}_{2\times 2} & 0 \\ 0 & \mathbf{0}_{1\times 2} & 1 \end{bmatrix}, \qquad k_{3,\alpha} = C_{\mathrm{M}} \frac{n_{\mathrm{t},\alpha} \pi \bar{d}_\alpha^2}{4},$$

where $\boldsymbol{I}_{2\times 2}$ and $\mathbf{0}_{1\times 2}$ represent the 2×2 identity matrix and the 1×2 zero matrix, respectively, so that $\boldsymbol{\mathcal{M}}_\alpha$ is in fact a 4×4 block matrix that represents the added-inertia effect due to turbulent interactions within layer α.

For the finite volume implementation, it is convenient to pre-multiply the flux terms by the inverse of this matrix,

$$\boldsymbol{\mathcal{C}}_\alpha = \boldsymbol{\mathcal{M}}_\alpha^{-1} = \begin{bmatrix} 1 & \mathbf{0}_{1\times 2} & 0 \\ \dfrac{\boldsymbol{u}_\alpha k_{3,\alpha}}{1+k_{3,\alpha}} & \dfrac{1}{1+k_{3,\alpha}} \boldsymbol{I}_{2\times 2} & 0 \\ 0 & \mathbf{0}_{1\times 2} & 1 \end{bmatrix},$$

so that the inertia contributions are handled consistently in the flux computation. In other words, the original system for each layer is multiplied by $\boldsymbol{\mathcal{M}}_\alpha$ to include the inertia effects, and the finite volume discretization applies $\boldsymbol{\mathcal{C}}_\alpha$ to isolate the time derivatives and maintain a consistent conservative formulation.

Hydrostatic predictor: path-conservative finite volume scheme

At this stage, we advance the multilayer system under the hydrostatic assumption, setting all non-hydrostatic pressures to zero ($q = 0$). The corresponding hyperbolic part of the equations is discretized by means of a *path-conservative finite volume scheme.* This stage computes an intermediate state W_i^* that will later be corrected by the non-hydrostatic projection step.

The computational domain is partitioned into non-overlapping control volumes V_i with polygonal boundaries. For simplicity, we consider a Cartesian mesh, so that each cell V_i has area $|V_i| = \Delta x\,\Delta y$. Let $\mathcal{K}_i$ denote the set of indices of all cells V_k that share a common edge E_{ik} with V_i. The length of this edge is denoted by $|E_{ik}|$, and $\boldsymbol{\eta}_{ik} = (\eta_{x,ik}, \eta_{y,ik})^{\mathrm{T}}$ is the outward unit normal vector to E_{ik}, pointing from cell V_i toward cell V_k. The distance between the cell centers of V_i and V_k is written as d_{ik}.

The semi-discrete update of the finite volume method reads

$$\boldsymbol{W}_i^* = \boldsymbol{W}_i^\nu - \frac{\Delta t}{|V_i|} \sum_{k\in\mathcal{K}_i} |E_{ik}|\, \mathcal{F}_{ik}(\boldsymbol{W}_i^\nu, \boldsymbol{W}_k^\nu, \boldsymbol{\eta}_{ik}) + \Delta t\, \boldsymbol{S}_i^{(f)}, \tag{3.2}$$

where $\boldsymbol{S}_i^{(f)}$ contains the hydrostatic source terms including the bed slope and vegetation contributions evaluated within cell V_i.

For each face E_{ik}, the numerical flux $\mathcal{F}_{ik}(\boldsymbol{W}_i, \boldsymbol{W}_k, \boldsymbol{\eta}_{ik})$ approximates the flux of the hyperbolic system in the direction of the interface normal $\boldsymbol{\eta}_{ik}$. The directionally projected flux is defined as

$$\boldsymbol{F}(\boldsymbol{W}, \boldsymbol{\eta}) = F_x(\boldsymbol{W})\,\eta_x + F_y(\boldsymbol{W})\,\eta_y,$$

where F_x and F_y are the physical flux functions in the x and y directions, respectively.

To compute $\mathcal{F}_{ik}$, we employ a path-conservative HLL-type Riemann solver that also accounts for the non-conservative products $B_x(W)\partial_x W$ and $B_y(W)\partial_y W$ present in the multilayer formulation. For the face between cells i and k, the flux reads

$$\begin{aligned}\mathcal{F}_{ik} &= \tfrac{1}{2}\boldsymbol{C}_{ik}\big(\boldsymbol{F}(\boldsymbol{W}_i, \boldsymbol{\eta}_{ik}) + \boldsymbol{F}(\boldsymbol{W}_k, \boldsymbol{\eta}_{ik})\big)\\ &\quad - \tfrac{1}{2}\boldsymbol{C}_{ik}\Big[\alpha_{0,ik}\,(\boldsymbol{W}_k - \boldsymbol{W}_i) + \alpha_{1,ik}\big(\boldsymbol{F}(\boldsymbol{W}_k, \boldsymbol{\eta}_{ik}) - \boldsymbol{F}(\boldsymbol{W}_i, \boldsymbol{\eta}_{ik}) + \mathcal{B}(\boldsymbol{W}_k, W_i, \boldsymbol{\eta}_{ik})\,(\boldsymbol{W}_k - \boldsymbol{W}_i)\big)\Big],\end{aligned} \tag{3.3}$$

where the coefficients $\alpha_{0,ik}$ and $\alpha_{1,ik}$ are computed from the estimated minimum and maximum signal velocities $S_{L,ik}$ and $S_{R,ik}$ along the normal direction $\boldsymbol{\eta}_{ik}$:

$$\alpha_{0,ik} = \frac{S_{R,ik}|S_{L,ik}| - S_{L,ik}|S_{R,ik}|}{S_{R,ik} - S_{L,ik}}, \qquad \alpha_{1,ik} = \frac{|S_{R,ik}| - |S_{L,ik}|}{S_{R,ik} - S_{L,ik}}.$$

The operator $\mathcal{B}(W_k, W_i, \boldsymbol{\eta}_{ik})$ represents the path integral of the non-conservative matrix along a straight segment joining $\boldsymbol{W}_i$ and $\boldsymbol{W}_k$ in the state space. This term guarantees the correct treatment of non-conservative products, which is essential for preserving the well-balanced property of the scheme.

The signal velocities $S_{L,ik}$ and $S_{R,ik}$ are estimated as in the standard HLL solver, using the layer-averaged velocities and the gravity-wave speed:

$$S_{L,ik} = \min_\alpha\big(u_i\eta_{x,ik} + v_i\eta_{y,ik} - \sqrt{g\,h_{\alpha,i}}\big), \qquad S_{R,ik} = \max_\alpha\big(u_k\eta_{x,ik} + v_k\eta_{y,ik} + \sqrt{g\,h_{\alpha,k}}\big).$$

This hydrostatic predictor stage produces the intermediate state $\boldsymbol{W}_i^*$, which is consistent with the hyperbolic dynamics of the multilayer model, maintains well-balancing for the still-water equilibrium, and preserves the positivity of the layer depths h_α. The correction due to non-hydrostatic pressure effects is subsequently applied during the projection step. The CFL condition ensuring stability is

$$\max_{i,k,l} \frac{|\lambda_{ik,l}|}{d_{ik}} \Delta t \leq 1,$$

where $\lambda_{ik,l}$ are the eigenvalues of $A(W_i, \boldsymbol{\eta}_{ik})$, the system matrix projected along the direction $\boldsymbol{\eta}_{ik}$ and evaluated at the W_i, and d_{ik} is the distance between cell centers.

Hydrostatic reconstruction at an interface

Consider an interface shared by a control volume i and one of its neighbouring cells k in a structured rectangular mesh. Without loss of generality, the index k refers to the neighbour located to the *north* or *east* of cell i. The free-surface elevations in the two cells are defined as

$$H_i := h_i + z_{b,i}, \qquad H_k := h_k + z_{b,k},$$

and the interface reference bed elevation is

$$z_{ik}^* := \max\{z_{b,i},\, z_{b,k}\}.$$

The *hydrostatic reconstruction* of the water depths across the interface between i and k volumes is then given by

$$h_{ik}^- = \max\{H_i - z_{ik}^*,\, 0\}, \qquad h_{ik}^+ = \max\{H_k - z_{ik}^*,\, 0\}. \tag{3.4}$$

For interfaces with neighbours to the west or south of cell i, the same expressions apply interchanges the roles of the "minus" and "plus" states.

Next we reconstruct velocities and concentration consistently with the reconstructed depths. Let consider $\mathbf{u}_{\alpha,i} = (u_{\alpha,i}, v_{\alpha,i})$ be the horizontal velocity of layer α in cell i. We will use the same velocity components from the cell (i.e. hydrostatic reconstruction preserves the cell velocity), but the reconstructed momentum for each layer is scaled by the reconstructed depth:

$$\big(h\mathbf{u}_\alpha\big)_{ik}^- = h_{,ik}^- \,\mathbf{u}_{\alpha,i}, \qquad \big(h\mathbf{u}_\alpha\big)_{ik}^+ = h_{ik}^+ \,\mathbf{u}_{\alpha,k}, \tag{3.5}$$

the same treatment is applied for hw_α. Then, the collect the reconstructed quantities into the interfacial states $W_{ik}^{\pm}$ is

$$W_{ik}^- := \Big(h_{ik}^-,\ \{h_{ik}^- \mathbf{u}_{\alpha,i},\ h_{ik}^- w_{\alpha,i}\}_{\alpha=1}^N \Big)^{\mathrm{T}},$$

$$W_{ik}^+ := \Big(h_{ik}^+,\ \{h_{\alpha,ik}^+ \mathbf{u}_{\alpha,k},\ h_{\alpha,ik}^+ w_{\alpha,k}\}_{\alpha=1}^N \Big)^{\mathrm{T}},$$

Using the hydrostatic reconstruction we enforce positivity and the well-balancing of the system, particularly in presence of dry fronts.

Semi-implicit friction and inertia correction

After the predictor, we apply a *local implicit correction* that incorporates the nonlinear drag and inertia effects. The hyperbolic step provides the intermediate state $\boldsymbol{W}^*$, and the corrected variables are obtained by solving

$$\frac{\boldsymbol{W}_\alpha^{\nu+1/3} - \boldsymbol{W}_\alpha^*}{\Delta t} = \boldsymbol{\mathcal{C}}_\alpha \boldsymbol{S}_\alpha^{(f)}(\boldsymbol{W}^{\nu+1/3}, \boldsymbol{W}^*),$$

where $\boldsymbol{S}_\alpha^{(f)}$ contains the quadratic drag and bed friction terms:

$$\boldsymbol{S}_\alpha^{(f)} = \begin{pmatrix} 0 \\ -k_{2,\alpha}(h_\alpha \boldsymbol{u}_\alpha)\|h_\alpha \boldsymbol{u}_\alpha\| \\ 0 \end{pmatrix}, \qquad k_{2,\alpha} = \frac{C_{D,\alpha} d_\alpha n_{t,\alpha}}{2\theta_\alpha h_\alpha}.$$

To enhance stability, the drag term is evaluated in a *semi-implicit form*:

$$h_\alpha \boldsymbol{u}_\alpha |h_\alpha \boldsymbol{u}_\alpha| \approx (h_\alpha \boldsymbol{u}_\alpha)^{n+1} \|h_\alpha \boldsymbol{u}_\alpha\|^*.$$

This yields the layer update:

$$\boldsymbol{W}_{\alpha,i}^{\nu+1/3} = \boldsymbol{N}_{\alpha,i} \boldsymbol{W}_{\alpha,i}^*,$$

where

$$\boldsymbol{N}_{\alpha,i} = \operatorname{diag}\left(1,\ \frac{1+k_{3,\alpha}}{1+k_{3,\alpha}+k_{2,\alpha}\|h_\alpha \boldsymbol{u}_\alpha\|\Delta t}\mathbf{1},\ 1\right), \quad \text{with} \quad \mathbf{1} = (1,1)^{\mathrm{T}}.$$

3.3.1 Adding viscosity and bottom friction

At this stage, we have obtained all layer variables at time level $t^{\nu+1}$, denoted by the intermediate state $(\cdot)^*$, before accounting for viscous and bottom friction effects. Since these forces only modify the horizontal velocity field, the update is performed for $\boldsymbol{u}_\alpha$ while keeping h_α fixed. The correction step for each layer reads

$$h_\alpha \boldsymbol{u}_\alpha^{\nu+2/3} = h_\alpha \boldsymbol{u}_\alpha^* + \frac{\Delta t}{\theta_\alpha}\mathbf{K}_{\alpha-1/2}^{\nu+2/3} - \frac{\Delta t}{\theta_\alpha}\mathbf{K}_{\alpha+1/2}^{\nu+2/3}, \tag{3.6}$$

where the interlayer viscous terms $\mathbf{K}_{\alpha\pm1/2}$ are defined in (2.7) and the bottom friction condition imposes $\mathbf{K}_{1/2} = -\boldsymbol{\tau}_1$ and $\mathbf{K}_{N+1/2} = \mathbf{0}$.

Substituting the definitions of $\mathbf{K}_{\alpha\pm1/2}$ and $\boldsymbol{\tau}_1$, we obtain the following implicit relations for the corrected velocities:

$$h_1 \boldsymbol{u}_1^{\nu+2/3} = h_1 \boldsymbol{u}_1^* - \Delta t\, k_1\, |h_1 \boldsymbol{u}_1^*|\, h_1 \boldsymbol{u}_1^{\nu+2/3} + \frac{\Delta t\, \eta_0}{2\theta_1 h_1}\,(\boldsymbol{u}_2^{\nu+1} - \boldsymbol{u}_1^{\nu+2/3}),$$

$$h_\alpha \boldsymbol{u}_\alpha^{\nu+2/3} = h_\alpha \boldsymbol{u}_\alpha^* - \frac{\Delta t\, \eta_0}{2\theta_\alpha h_\alpha}(\boldsymbol{u}_\alpha^{\nu+2/3} - \boldsymbol{u}_{\alpha-1}^{\nu+2/3}) + \frac{\Delta t\, \eta_0}{2\theta_\alpha h_\alpha}(\boldsymbol{u}_{\alpha+1}^{\nu+2/3} - \boldsymbol{u}_\alpha^{\nu+2/3}), \quad \alpha = 2, \ldots, N-1,$$

$$h_N \boldsymbol{u}_N^{\nu+2/3} = h_N \boldsymbol{u}_N^* - \frac{\Delta t\, \eta_0}{2\theta_N h_N}(\boldsymbol{u}_N^{\nu+2/3} - \boldsymbol{u}_{N-1}^{\nu+2/3}).$$

This system can be rewritten in compact matrix form as a tridiagonal problem for the unknown velocities $\boldsymbol{u}_1^{\nu+2/3}, \dots, \boldsymbol{u}_N^{\nu+2/3}$:

$$\begin{aligned}
&\left(1 + \frac{\eta_0 \Delta t}{2\theta_1 h_1^2} + \Delta t\, k_1 |h_1 \boldsymbol{u}_1^*|\right) h_1 \boldsymbol{u}_1^{\nu+2/3} - \frac{\eta_0 \Delta t}{2\theta_1 h_1^2}\, h_1 \boldsymbol{u}_2^{\nu+2/3} = h_1 \boldsymbol{u}_1^*, \\
&\left(1 + \frac{\eta_0 \Delta t}{\theta_\alpha h_\alpha^2}\right) h_\alpha \boldsymbol{u}_\alpha^{\nu+2/3} - \frac{\eta_0 \Delta t}{2\theta_\alpha h_\alpha^2} h_\alpha \big(\boldsymbol{u}_{\alpha-1}^{\nu+2/3} + \boldsymbol{u}_{\alpha+1}^{\nu+2/3}\big) = h_\alpha \boldsymbol{u}_\alpha^*, \quad \alpha = 2, \dots, N-1, \\
&\left(1 + \frac{\eta_0 \Delta t}{2\theta_N h_N^2}\right) h_N \boldsymbol{u}_N^{\nu+2/3} - \frac{\eta_0 \Delta t}{2\theta_N h_N^2}\, h_N \boldsymbol{u}_{N-1}^{\nu+2/3} = h_N \boldsymbol{u}_N^*.
\end{aligned}$$

The resulting tridiagonal linear system is symmetric and diagonally dominant, and it is solved efficiently at each time step by a Thomas algorithm. Since each horizontal velocity component (u_α, v_α) evolves independently in this step, the same tridiagonal system is solved twice, once for each velocity component.

Non-hydrostatic projection

As in the one-dimensional formulation [14], the non-hydrostatic variables q_α (and the interface pressures $q_{\alpha\pm1/2}$) are not advanced through hyperbolic transport equations. Instead, they are obtained by enforcing the incompressibility or kinematic constraint (2.5) at the new time step. This procedure leads to an elliptic (Poisson-like) problem for the pressure corrections which is solved during the projection step. The projection approach introduced in [14] extends naturally to two dimensions, with the elliptic operator incorporating spatially variable coefficients that depend on the layer thickness h_α, the porosity θ_α, and the geometric effects associated with the bottom topography ∇z_{b}.

The intermediate solution $\boldsymbol{W}^*$ is corrected by projecting the non-hydrostatic pressure field. For each layer α, the intermediate velocities $\boldsymbol{u}_\alpha^*$ and w_α^* are updated according to the pressure gradients obtained from the solution of the elliptic system. It is worth noting that, since the mass conservation equation for h_α does not depend on the non-hydrostatic pressure, the layer thickness remains unchanged during this projection step, that is,

$$h_\alpha^{\nu+1} = h_\alpha^*.$$

The correction is thus applied exclusively to the velocity components, which ensures that the final solution satisfies the discrete incompressibility constraint at time level $n+1$.

$$h_\alpha^{\nu+1} \boldsymbol{u}_\alpha^{\nu+1} = h_\alpha^* \boldsymbol{u}_\alpha^* - f_\alpha^* \Delta t \left[\frac{1}{2}\nabla\left(h_\alpha^{\nu+1}\, q_{\alpha-1/2}^{\nu+1} + h_\alpha^{\nu+1}\, q_{\alpha+1/2}^{\nu+1}\right) + q_{\alpha-1/2}^{\nu+1} \nabla z_{\alpha-1/2}^{\nu+1} - q_{\alpha+1/2}^{\nu+1} \nabla z_{\alpha+1/2}^{\nu+1}\right], \tag{3.7}$$

with

$$f_\alpha = \frac{\theta_\alpha}{1 + k_{3,\alpha} + k_{2,\alpha}\|\boldsymbol{u}_\alpha\|\Delta t},$$

and $q_{\alpha\pm1/2}$ denotes the non-hydrostatic pressure at the interface between layers α and $\alpha \pm 1/2$. For the vertical velocity we have

$$h_\alpha^{\nu+1} w_\alpha^{\nu+1} = h_\alpha^* w_\alpha^* - \Delta t\, q_{\alpha+1/2}^{\nu+1} + \Delta t\, q_{\alpha-1/2}^{\nu+1}. \tag{3.8}$$

On the other hand, we enforce the N incompressibility conditions $E_\alpha = 0$ for $\alpha = 1, \ldots, N$, with

$$E_\alpha = h_\alpha \nabla \cdot \boldsymbol{u}_\alpha + 2w_{\alpha+1/2}^- - 2w_\alpha, \tag{3.9}$$

where

$$w_{\alpha+1/2}^- = \partial_t z_b + \boldsymbol{u}_\alpha \cdot \nabla z_{\alpha+1/2} - \sum_{\beta=1}^{\alpha} \nabla \cdot (h_\beta \boldsymbol{u}_\beta).$$

Equivalently, we impose

$$E_1 = 0, \qquad E_2 - E_1 = 0,\ \ldots,\ E_N - E_{N-1} = 0.$$

Case $\alpha = 1$. For the bottom layer we obtain

$$-\, h_1 \nabla \cdot (h_1 \boldsymbol{u}_1) + 2(\nabla z_1) \cdot h_1 \boldsymbol{u}_1 - 2h_1 w_1 = -2h_1\, \partial_t z_b. \tag{3.10}$$

Case $\alpha = 2, \ldots, N$. For higher layers we write

$$(h_\alpha \nabla \cdot \boldsymbol{u}_\alpha - h_{\alpha-1} \nabla \cdot \boldsymbol{u}_{\alpha-1}) + 2\,(w_{\alpha+1/2}^- - w_{\alpha-1/2}^-) - 2\,(w_\alpha - w_{\alpha-1}) = 0.$$

Substituting the definition of $w_{\alpha-1/2}^-$ gives

$$\begin{aligned}(h_\alpha \nabla \cdot \boldsymbol{u}_\alpha - h_{\alpha-1} \nabla \cdot \boldsymbol{u}_{\alpha-1}) + 2\Big(\boldsymbol{u}_\alpha \cdot \nabla z_{\alpha+1/2} - \boldsymbol{u}_{\alpha-1} \cdot \nabla z_{\alpha-1/2} - \nabla(h_\alpha \boldsymbol{u}_\alpha)\Big) \\ - 2(w_\alpha - w_{\alpha-1}) = 0.\end{aligned} \tag{3.11}$$

Equal layer thickness. If we assume uniform thickness $h_\alpha = h/N$ for all α, multiplying through by $h_\alpha = h_{\alpha-1}$ yields

$$-\, h_\alpha \nabla\cdot(h_\alpha \boldsymbol{u}_\alpha) - h_\alpha \nabla\cdot(h_\alpha \boldsymbol{u}_{\alpha-1}) + 2h_\alpha \boldsymbol{u}_\alpha\cdot\nabla z_\alpha - 2h_\alpha \boldsymbol{u}_{\alpha-1}\cdot\nabla z_{\alpha-1} - 2h_\alpha w_\alpha + 2h_\alpha w_{\alpha-1} = 0. \tag{3.12}$$

Replacing (3.7) and (3.8) in the incompressibility conditions (3.10)–(3.12) we get a linear system of equations for the unknown interface pressures $q_{\alpha+1/2}, q_{\alpha-1/2}$ and $q_{\alpha-3/2}$. For simplicity, in what follows we denote $h_\alpha^{n+1} = h_\alpha^*$ and $z_\alpha^{n+1} = z_\alpha^*$ simply as h_α and z_α, respectively.

$$
\begin{aligned}
& h_\alpha \nabla \cdot \left\{ f_\alpha^* \Delta t \left[\frac{1}{2} \nabla (h_\alpha \, q_{\alpha-1/2}^{\nu+1}) + \frac{1}{2} \nabla (h_\alpha \, q_{\alpha+1/2}^{\nu+1}) + q_{\alpha-1/2}^{\nu+1} \nabla z_{\alpha-1/2} - q_{\alpha+1/2}^{\nu+1} \nabla z_{\alpha+1/2} \right] \right\} \\
+ \;& h_\alpha \nabla \cdot \left\{ f_{\alpha-1}^* \Delta t \left[\frac{1}{2} \nabla (h_\alpha \, q_{\alpha-3/2}^{\nu+1}) + \frac{1}{2} \nabla (h_\alpha \, q_{\alpha-1/2}^{\nu+1}) + q_{\alpha-3/2}^{\nu+1} \nabla z_{\alpha-3/2} - q_{\alpha-1/2}^{\nu+1} \nabla z_{\alpha-1/2} \right] \right\} \\
- \;& 2 f_\alpha^* \Delta t \left[\frac{1}{2} \nabla (h_\alpha \, q_{\alpha-1/2}^{\nu+1}) + \frac{1}{2} \nabla (h_\alpha \, q_{\alpha+1/2}^{\nu+1}) + q_{\alpha-1/2}^{\nu+1} \nabla z_{\alpha-1/2} - q_{\alpha+1/2}^{\nu+1} \nabla z_{\alpha+1/2} \right] \cdot \nabla z_\alpha \\
+ \;& 2 f_{\alpha-1}^* \Delta t \left[\frac{1}{2} \nabla (h_\alpha \, q_{\alpha-3/2}^{\nu+1}) + \frac{1}{2} \nabla (h_\alpha \, q_{\alpha-1/2}^{\nu+1}) + q_{\alpha-3/2}^{\nu+1} \nabla z_{\alpha-3/2} - q_{\alpha-1/2}^{\nu+1} \nabla z_{\alpha-1/2} \right] \cdot \nabla z_{\alpha-1} \\
- \;& 2 \Delta t \left(q_{\alpha+1/2}^{\nu+1} - 2 q_{\alpha-1/2}^{\nu+1} + q_{\alpha-3/2}^{\nu+1} \right) \\
= \;& h_\alpha \nabla \cdot (h_\alpha \boldsymbol{u}_\alpha^*) + h_\alpha \nabla \cdot (h_\alpha \boldsymbol{u}_{\alpha-1}^*) - 2 h_\alpha \boldsymbol{u}_\alpha^* \cdot \nabla z_\alpha + 2 h_\alpha \boldsymbol{u}_{\alpha-1}^* \cdot \nabla z_{\alpha-1} + 2 (h_\alpha w_\alpha^* - h_\alpha w_{\alpha-1}^*)
\end{aligned}
$$

In matrix form, this system resembles a discrete Poisson problem that links all layers through the vertical fluxes.

$$
\begin{aligned}
P^* = & M_{p,p} \, q_{\alpha-\frac{1}{2}, i+\frac{1}{2}, j+\frac{1}{2}} + M_{p,p_E} \, q_{\alpha-\frac{1}{2}, i+\frac{3}{2}, j+\frac{1}{2}} + M_{p,p_W} \, q_{\alpha-\frac{1}{2}, i-\frac{1}{2}, j+\frac{1}{2}} \\
& + M_{p,p_N} \, q_{\alpha-\frac{1}{2}, i+\frac{1}{2}, j+\frac{3}{2}} + M_{p,p_S} \, q_{\alpha-\frac{1}{2}, i+\frac{1}{2}, j-\frac{1}{2}} .
\end{aligned} \tag{3.13}
$$

Here, the coefficients $M_{p,p}$, M_{p,p_E}, M_{p,p_W}, M_{p,p_N}, and M_{p,p_S} correspond to the central, east, west, north, and south neighboring cells, respectively, following the standard finite-volume notation. The subscripts E, W, N, and S indicate the adjacent control volumes in the positive x-direction (East), negative x-direction (West), positive y-direction (North), and negative y-direction (South). Thus, the discrete operator represents a five-point stencil coupling the pressure unknown Q at the cell center with its four immediate neighbors.

All coefficients are evaluated at the face location $(i+\frac{1}{2}, j+\frac{1}{2})$ unless otherwise noted. Denote by $f_{\alpha, i+\frac{1}{2}, j+\frac{1}{2}}$ the interpolation of f_α to the face $(i+\frac{1}{2}, j+\frac{1}{2})$, and similarly for $h_{i+\frac{1}{2}, j+\frac{1}{2}}$. Also we introduce the auxiliary function $\boldsymbol{\phi}$

$$
\boldsymbol{\phi}_\alpha = 2N \nabla \left(z_{\alpha-\frac{1}{2}} + \frac{h_\alpha}{2} \right) = \left(\phi_\alpha^{(x)}, \phi_\alpha^{(y)} \right).
$$

We use the notation $|\boldsymbol{\phi}_\alpha|^2 = (\phi_\alpha^{(x)})^2 + (\phi_\alpha^{(y)})^2$.

Diagonal coefficients

$$\begin{aligned}
M_{p,p} = \Big(&8N^2 + f_{\alpha,i+\frac{1}{2},j+\frac{1}{2}}\,|\boldsymbol{\phi}_{\alpha,i+\frac{1}{2},j+\frac{1}{2}}|^2 + f_{\alpha-1,i+\frac{1}{2},j+\frac{1}{2}}\,|\boldsymbol{\phi}_{\alpha-1,i+\frac{1}{2},j+\frac{1}{2}}|^2\Big)\\
&- h_{i+\frac{1}{2},j+\frac{1}{2}}\,\partial_x\big(f_{\alpha,i+\frac{1}{2},j+\frac{1}{2}}\,\phi^{(x)}_{\alpha,i+\frac{1}{2},j+\frac{1}{2}}\big) + h_{i+\frac{1}{2},j+\frac{1}{2}}\,\partial_x\big(f_{\alpha-1,i+\frac{1}{2},j+\frac{1}{2}}\,\phi^{(x)}_{\alpha-1,i+\frac{1}{2},j+\frac{1}{2}}\big)\\
&- h_{i+\frac{1}{2},j+\frac{1}{2}}\,\partial_y\big(f_{\alpha,i+\frac{1}{2},j+\frac{1}{2}}\,\phi^{(y)}_{\alpha,i+\frac{1}{2},j+\frac{1}{2}}\big) + h_{i+\frac{1}{2},j+\frac{1}{2}}\,\partial_y\big(f_{\alpha-1,i+\frac{1}{2},j+\frac{1}{2}}\,\phi^{(y)}_{\alpha-1,i+\frac{1}{2},j+\frac{1}{2}}\big)\\
&+ \frac{2}{\Delta x^2}\,h^2_{i+\frac{1}{2},j+\frac{1}{2}}\big(f_{\alpha,i+\frac{1}{2},j+\frac{1}{2}} + f_{\alpha-1,i+\frac{1}{2},j+\frac{1}{2}}\big)\\
&+ \frac{2}{\Delta y^2}\,h^2_{i+\frac{1}{2},j+\frac{1}{2}}\big(f_{\alpha,i+\frac{1}{2},j+\frac{1}{2}} + f_{\alpha-1,i+\frac{1}{2},j+\frac{1}{2}}\big).
\end{aligned}\tag{3.14}$$

East / West (x–direction) coefficients

$$\begin{aligned}
M_{p,p_E} &= -\frac{1}{2\Delta x}\,\Big[h_{i+\frac{1}{2},j+\frac{1}{2}}\,\partial_x\big(f_{\alpha,i+\frac{1}{2},j+\frac{1}{2}}\,h_{i+\frac{1}{2},j+\frac{1}{2}}\big) + h_{i+\frac{1}{2},j+\frac{1}{2}}\,\partial_x\big(f_{\alpha-1,i+\frac{1}{2},j+\frac{1}{2}}\,h_{i+\frac{1}{2},j+\frac{1}{2}}\big)\Big]\\
&\quad - \frac{1}{\Delta x^2}\,h^2_{i+\frac{1}{2},j+\frac{1}{2}}\big(f_{\alpha,i+\frac{1}{2},j+\frac{1}{2}} + f_{\alpha-1,i+\frac{1}{2},j+\frac{1}{2}}\big),\\
M_{p,p_W} &= +\frac{1}{2\Delta x}\,\Big[h_{i+\frac{1}{2},j+\frac{1}{2}}\,\partial_x\big(f_{\alpha,i+\frac{1}{2},j+\frac{1}{2}}\,h_{i+\frac{1}{2},j+\frac{1}{2}}\big) + h_{i+\frac{1}{2},j+\frac{1}{2}}\,\partial_x\big(f_{\alpha-1,i+\frac{1}{2},j+\frac{1}{2}}\,h_{i+\frac{1}{2},j+\frac{1}{2}}\big)\Big]\\
&\quad - \frac{1}{\Delta x^2}\,h^2_{i+\frac{1}{2},j+\frac{1}{2}}\big(f_{\alpha,i+\frac{1}{2},j+\frac{1}{2}} + f_{\alpha-1,i+\frac{1}{2},j+\frac{1}{2}}\big).
\end{aligned}\tag{3.15}$$

North / South (y–direction) coefficients

$$\begin{aligned}
M_{p,p_N} &= -\frac{1}{2\Delta y}\,\Big[h_{i+\frac{1}{2},j+\frac{1}{2}}\,\partial_y\big(f_{\alpha,i+\frac{1}{2},j+\frac{1}{2}}\,h_{i+\frac{1}{2},j+\frac{1}{2}}\big) + h_{i+\frac{1}{2},j+\frac{1}{2}}\,\partial_y\big(f_{\alpha-1,i+\frac{1}{2},j+\frac{1}{2}}\,h_{i+\frac{1}{2},j+\frac{1}{2}}\big)\Big]\\
&\quad - \frac{1}{\Delta y^2}\,h^2_{i+\frac{1}{2},j+\frac{1}{2}}\big(f_{\alpha,i+\frac{1}{2},j+\frac{1}{2}} + f_{\alpha-1,i+\frac{1}{2},j+\frac{1}{2}}\big),\\
M_{p,p_S} &= +\frac{1}{2\Delta y}\,\Big[h_{i+\frac{1}{2},j+\frac{1}{2}}\,\partial_y\big(f_{\alpha,i+\frac{1}{2},j+\frac{1}{2}}\,h_{i+\frac{1}{2},j+\frac{1}{2}}\big) + h_{i+\frac{1}{2},j+\frac{1}{2}}\,\partial_y\big(f_{\alpha-1,i+\frac{1}{2},j+\frac{1}{2}}\,h_{i+\frac{1}{2},j+\frac{1}{2}}\big)\Big]\\
&\quad - \frac{1}{\Delta y^2}\,h^2_{i+\frac{1}{2},j+\frac{1}{2}}\big(f_{\alpha,i+\frac{1}{2},j+\frac{1}{2}} + f_{\alpha-1,i+\frac{1}{2},j+\frac{1}{2}}\big).
\end{aligned}\tag{3.16}$$

Finally, $M_{p,q} = 0$ for all other columns, so each row has at most five nonzero entries: center, east, west, north and south. All spatial derivatives ∂_x, ∂_y above are evaluated at the face $(i+\frac{1}{2}, j+\frac{1}{2})$. In practice use central differences, e.g.

$$\partial_x \Phi_{i+\frac{1}{2},j+\frac{1}{2}} \approx \frac{\Phi_{i+1,j+\frac{1}{2}} - \Phi_{i,j+\frac{1}{2}}}{\Delta x},$$

where Φ denotes the interpolated quantity.

The structure of the system matrix is identical to that presented in our previous work [14], with the main difference that the present formulation is in two dimensions: the scalar velocity u is replaced by the vector $\boldsymbol{u}$, the derivative ∂_x is replaced by the gradient operator ∇, and the corresponding scalar products are generalized accordingly. To obtain the solution, we employ an iterative algorithm (e.g., a Gauss–Seidel relaxation) until the residual of the incompressibility constraints falls below a prescribed tolerance (10^{-6}).

Once the pressure field is computed, we return to (3.7)–(3.8) and correct the velocities accordingly, evaluating $q_{\alpha+1/2}, q_{\alpha-1/2}$ and $q_{\alpha-3/2}$ with the obtained values.

Summary of algorithm per time step

At each time step:

1. **Hydrostatic predictor:** explicit finite volume update using HLL fluxes and hydrostatic reconstruction.
2. **Semi-implicit correction:** apply inertia (via $\boldsymbol{\mathcal{M}}_\alpha$) and drag stabilization.
3. **Viscosity and bottom friction correction:** Update horizontal velocities by solving a tridiagonal system from viscous coupling between layers.
4. **Non-hydrostatic projection:** solve pressure Poisson-like system and correct velocities.
5. **Update variables and check CFL.**

3.4 Numerical experiments: tsunami–forest interaction

3.4.1 Experimental reference and setup

The numerical tests presented here are based on the laboratory experiments of Iimura and Tanaka [46], which investigate tsunami–vegetation interactions at a 1:100 scale. This configuration was previously used in one-dimensional multilayer simulations [14] to validate the LDNH$_0$ model against measured water levels and drag forces. Here, we extend the approach to two horizontal dimensions to analyze lateral effects on tsunami attenuation and flow variability induced by vegetation. The experimental setup consists of a 15 m long and 0.4 m wide flume with a sloping bottom representing a beach (Figure 1.4). A wave-making plate at $x = 0$ m generates a solitary wave of amplitude $\eta_0 = 3.14$ cm over still water depth $h_0 = 0.4$ m. Vegetation is represented by arrays of vertical cylinders ($d = 5$ mm) arranged between $x = 10.36$ m and $x = 11.36$ m, forming forest patches of varying densities (Figure 1.5). Nine gauge stations

(G_1–G_9) record free-surface elevations and cylinder forces. Among the 15 experimental cases reported by [46], five representative vegetation arrangements (Cases 1, 3, 5, 8, 13) were selected; in this study, we first focus on Case 3, a uniform forest configuration, as a baseline for assessing two-dimensional flow effects.

3.4.2 Vegetation parameters and wave generation

Vegetation parameters are derived from the forest geometry. The vegetation thickness is computed as

$$d_n = \frac{2}{\sqrt{3}D_{\mathrm{f}}^2} W_{\mathrm{f}} d \times 10^5 + \frac{2}{\sqrt{3}D_{\mathrm{b}}^2} W_{\mathrm{b}} d \times 10^5, \tag{4.1}$$

where D_{f} and D_{b} denote tree spacing in the front and back sections of the forest, and W_{f} and W_{b} their respective lengths. The tree density, in trees per square meter, is

$$n_{\mathrm{t}} = \frac{d_n}{W \times 0.4\ \mathrm{m}}, \qquad W = W_{\mathrm{f}} + W_{\mathrm{b}}. \tag{4.2}$$

The solitary wave generated by the piston follows the Rayleigh profile [66]:

$$\eta(x,0) = \eta_0 \operatorname{sech}^2(\beta x), \qquad \beta = \sqrt{\frac{3\eta_0}{4h_0^2(h_0+\eta_0)}}, \qquad u(x,0) = c\,\frac{\eta(x,0)}{h(x,0)}, \quad c = \sqrt{g(h_0+\eta_0)}. \tag{4.3}$$

3.4.3 Computational domain and boundary conditions

The full flume (15 m×0.4 m) is discretized with a uniform Cartesian mesh $\Delta x = \Delta y = 0.02$ m. The inlet imposes the solitary wave of (4.3), the outlet uses a transmissive condition to prevent reflections, and lateral walls are treated as slip boundaries.

3.4.4 Example 3.1 Calibration results

As a first validation, we reproduce Case 3, of Iimura et al. [46] experiment, described in Section 1.5.2, corresponding to a uniform forest. Figure 3.1 compares the simulated free-surface elevation at the downstream edge of the vegetation with the experimental data. The simulation accurately reproduces the wave amplitude, shape, and arrival time, demonstrating that the model correctly captures the interaction between the solitary wave and the vegetation array. This single calibration test confirms that the numerical framework resolves the key hydrodynamic processes, including wave attenuation, flow redistribution. Having established this baseline, the model will be used in subsequent simulations to systematically investigate how different forest configurations influence tsunami propagation and flow dynamics.

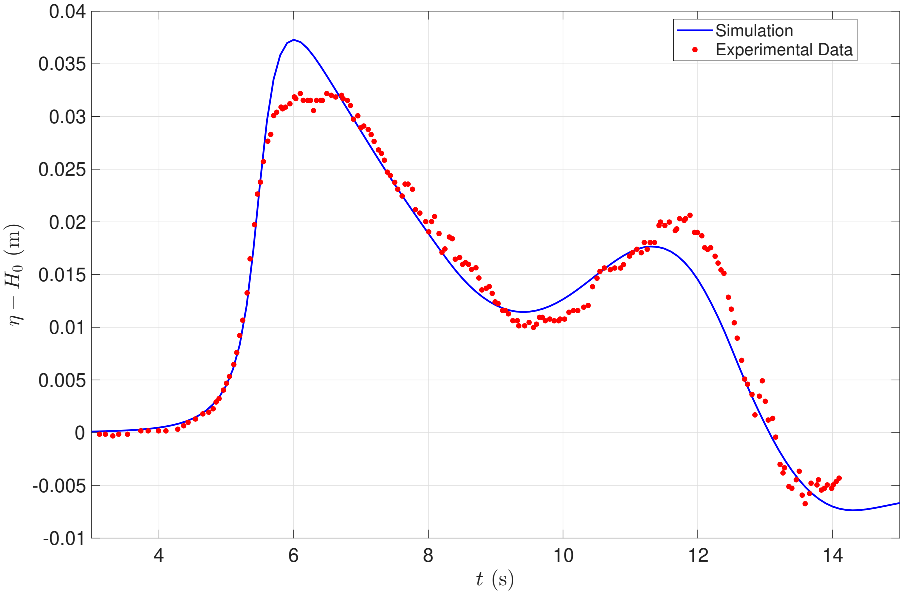

Figure 3.1: Temporal evolution of η in Case 3 of [46] at the downstream end of the vegetation ($x = 11.36$ m), with $H_0 = 0.44$ m representing the water level at rest. The number of layers is set to 10.

3.4.5 Example 3.2 Partial forest configuration: central patch

To investigate the influence of lateral forest distribution, we consider a variation of Case 3 in which the vegetation is confined to the central portion of the flume. In this configuration, the forest occupies only the region $y \in [-0.05, 0.05]$ m in the transverse direction, which spans the full channel width of $[-0.2, 0.2]$ m. Also we will consider 10 layers case in order to also study the verticality of the test.

This setup allows us to investigate how the partial lateral coverage of the forest modifies tsunami propagation, wave attenuation, and flow redistribution. By comparing this configuration with the full-width forest of Case 3, we can isolate the influence of lateral variability and assess how concentrated vegetation patches affect both the amplitude and the spatial structure of the water surface, including potential lateral flow around the vegetation.

As shown in Figure 3.2, the incoming wave reaches the upstream edge of the forest ($x = 11$ m) at approximately $t = 6$ s, where the vegetation partially blocks its propagation. Along the flume sides, outside the vegetated region, the wave advances freely, illustrating how lateral confinement of the forest redistributes the flow. When the backflow develops after reflection from downstream, the vegetation again exerts a damping effect, reducing both the velocity and surface elevation of the returning wave.

Figure 3.3 presents the corresponding horizontal velocity field $\boldsymbol{u} = (u, v)^{\mathrm{T}}$ at two characteristic stages. At $t = 6$ s, as the wave front impacts the forest, the vegetation generates a strong resistance that decelerates the flow within the canopy and increases velocity upstream of it.

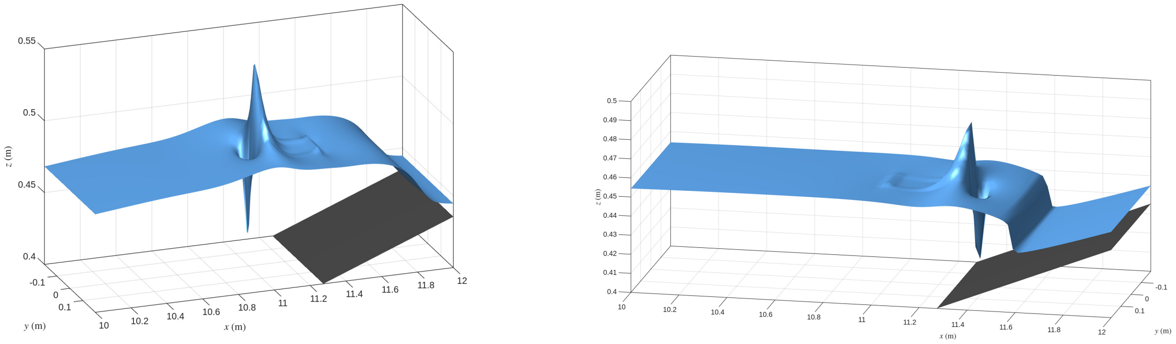

Figure 3.2: Snapshots of η in Case 3 of [46] at the downstream end of the vegetation ($x = 11.36$ m), with $H_0 = 0.44$ m and the forest confined to $y \in [-0.05, 0.05]$. Left: Wave reaching the front of the forest ($t = 6$ s). Right: Back flow of the forest ($t = 11$ s).

This partial blockage diverts part of the flow laterally, producing marked transverse velocity components near the forest edges.

At $t = 11$ s, when the wave moves seaward, the interaction reverses: the forest again induces momentum accumulation at its downstream boundary and local high-velocity zones around it. This pattern of deceleration inside the vegetation and acceleration near its borders demonstrates how the forest simultaneously dissipates energy and redistributes the flow during both the advancing and receding phases of the wave.

The snapshots also reveal several complementary features of the flow–vegetation interaction. A pronounced velocity gradient forms between vegetated and non-vegetated areas, evidencing lateral flow redistribution. Partial reflection at the forest edge produces a localized rise in free-surface elevation immediately upstream, while the velocity within and behind the forest remains significantly lower than in unobstructed zones. Overall, these results highlight the dual hydrodynamic role of the forest as both a dissipative and deflective structure that shapes the spatial pattern of wave propagation.

As shown in Figure 3.4, at $t = 19$ s, the flow exhibits a distinct recirculation pattern near the beach. This phenomenon arises when water climbing the slop goes backward and interacts with the portion of the wave that is still propagating through the forest. The interaction generates backward flow and local vortices that are only resolved in a multilayer model; a single-layer approach fails to capture this complex vertical structure. The velocity vectors indicate a clear separation between backward-moving water near the slope and the advancing flow, forming a closed-loop circulation.

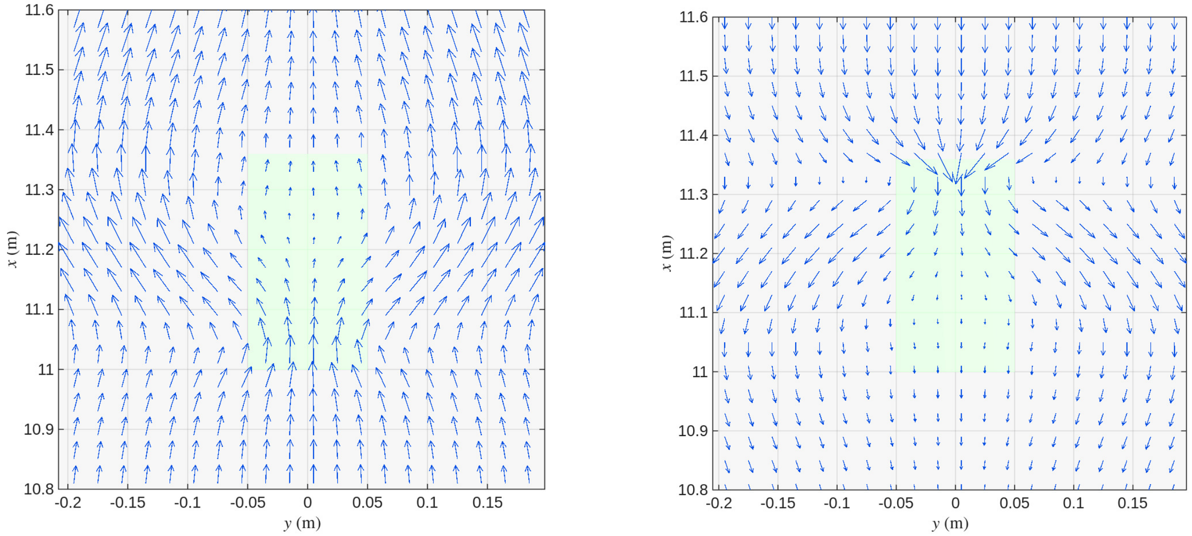

Figure 3.3: Snapshots of the mean horizontal velocity field $\boldsymbol{u} = (u, v)^{\mathrm{T}}$ in Case 3 of [46] at the downstream end of the vegetation ($x = 11.36$ m), with $H_0 = 0.44$ m and the forest confined to $y \in [-0.05, 0.05]$. Left: Wave reaching the front of the forest ($t = 6$ s). Right: Wave reaching the back of the forest ($t = 11$ s).

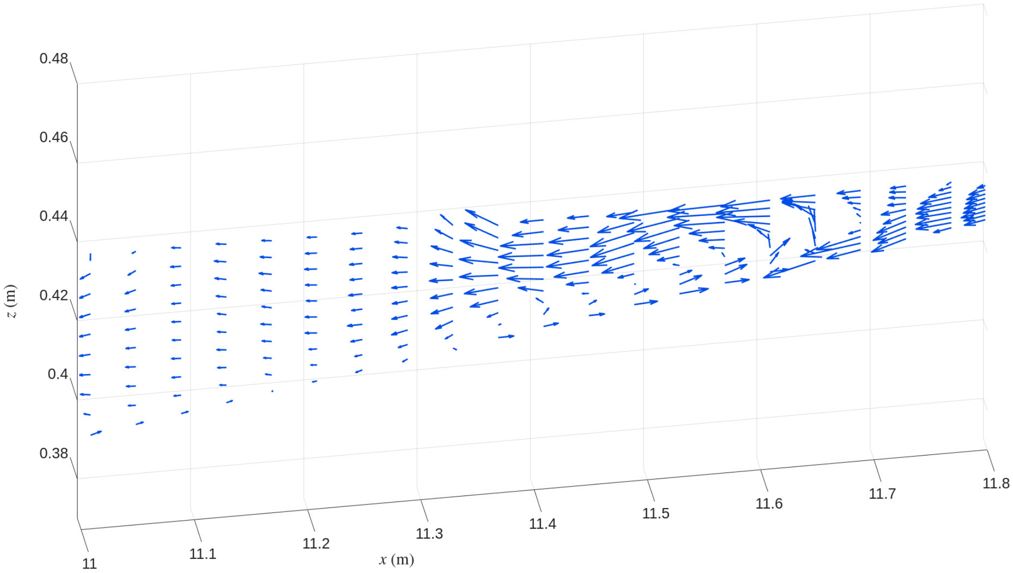

Figure 3.4: Velocity vector field $(u, w)^{\mathrm{T}}$ in the vertical xz plane at $y = 0$ in the middle of the forest, at $t = 19$ s. The plot highlights the development of a recirculation zone near the beach. This phenomenon is only captured by a multilayer model, while a single-layer model cannot resolve it.

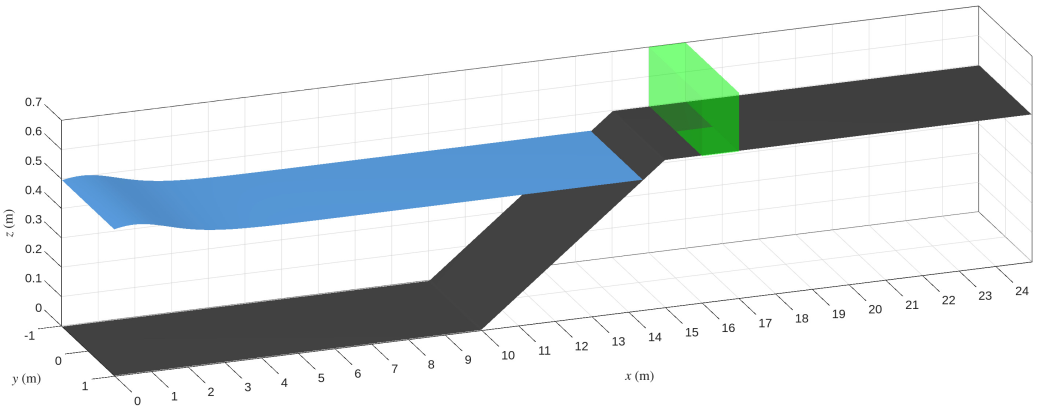

Figure 3.5: Initial condition of the channel, showing the bathymetry, the water level and the vegetation configuration for the full-width patch spans the entire y-range.

3.4.6 Example 3.3: Influence of a uniform vegetation patch

We consider a rectangular channel with spatial dimensions $x \in [-5, 25]$ m, $\quad y \in [-1, 1]$ m, and an initial solitary wave described by (4.3), with amplitude $\eta_0 = 0.0628$ m and still water level $h_0 = 0.44$ m and the number of layers is set to 10. The channel bathymetry is defined as a piecewise function:

$$z_b(x) = \begin{cases} 0, & x \leq 10 \text{ m}, \\ 0.1\,(x - 10), & 10 < x \leq 15 \text{ m}, \\ 0.5, & x > 15 \text{ m}. \end{cases} \tag{4.4}$$

The initial condition, along with the bathymetry and vegetation regions, is illustrated in Figure 3.5.

For the vegetation area, we consider two uniform configurations, both placed in the region $x \in [16, 17]$ m: the small vegetation area covers $y \in [-0.25, 0.25]$, while the larger configuration extends across the full width, $y \in [-1, 1]$. The stem diameter and density are identical for both configurations, with $d = 0.005$ m and $\rho = 1604$ stems/m^2, respectively.

Figure 3.6 presents the maximum water level at each point along the channel for simulations with and without vegetation. The presence of the forest significantly limits wave propagation into the vegetated region, whereas in the absence of vegetation the wave reaches further downstream. The water level increases locally at the forest front ($x = 16$ m), indicating flow accumulation caused by obstruction.

In the small patch configuration, we observe that the water flows around the vegetation, similar to what was seen in Example 3.2. This creates a protective region, or wake, behind the vegetation, which also reduces the extent to which the water propagates further downstream.

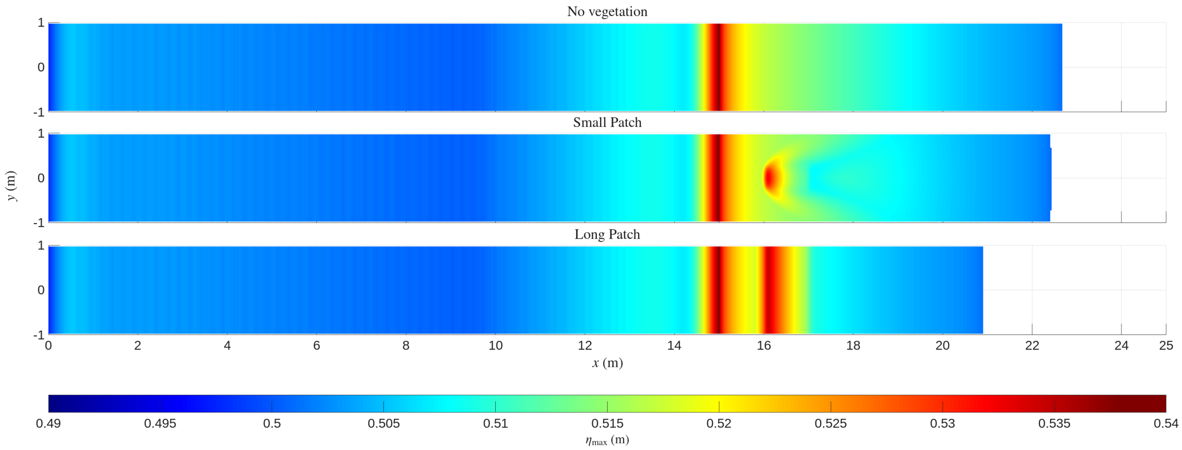

Figure 3.6: Maximum water level comparison. Top: simulation without vegetation. Middle: simulations whit a small vegetation patch. Bottom: simulation with a long vegetation patch. The forest reduces wave penetration and increases water level at the leading and trailing edges of the vegetated region.

This behavior illustrates both energy dissipation and flow deflection due to the forest. The stems extract momentum from the incoming wave, reducing downstream propagation. These effects highlight the protective role of the vegetation in mitigating tsunami impact, in agreement with previous studies (e.g., Case 3 in [46]) where vegetation modifies wave amplitude and spatial structure.

CHAPTER 4

Conclusions and Future Work

4.1 Conclusions

This doctoral thesis contributes to the advancement of mathematical and numerical modeling for shallow-water-type systems applied to geophysical flows. Although the different studies address distinct environmental processes, they share a common purpose: to improve the physical realism and numerical reliability of depth-averaged models through the incorporation of non-hydrostatic effects, multi-layer formulations, and well-balanced finite volume schemes. This approach aims to provide a more accurate representation of real-world phenomena.

The first part of the thesis focuses on the development of a one-dimensional multi-layer non-hydrostatic model to simulate tsunami propagation through coastal vegetation. The model combines finite volume and projection methods to reproduce experimental observations accurately and to provide a robust framework for studying the mitigation effects of coastal forests. Through a multi-layer formulation based on LDNH_0, the model overcomes the limitations of traditional approaches that rely on averaged vegetation properties. The inclusion of vertical variability in the drag, inertia, and porosity terms allows the model to represent the influence of vegetation structure along the water column and to improve the accuracy of wave attenuation and energy dissipation. The representation of non-hydrostatic pressure through an elliptic projection enhances the stability and smoothness of the velocity field, which enables the model to capture sharp gradients and transient flow features with physical consistency.

Chapter 3 extends the multi-layer non-hydrostatic model developed in the first part to two horizontal dimensions to provide a more comprehensive analysis of tsunami–forest interactions in realistic configurations. The 2D framework reveals complex hydrodynamic behaviors such as vertical recirculation, return flows near the beach, and lateral flow redistribution within and around the vegetated region, that highlights the essential role of vertical resolution in reproducing three-dimensional-like flow features. The numerical experiments show that, while a single-layer model can reproduce bulk propagation, only a multi-layer formulation captures the internal flow structure, energy transfer between layers, and feedback mechanisms that govern the damping efficiency of coastal forests. The multi-layer model therefore serves as a valuable tool to analyze the protective function of vegetation belts and for improving coastal management strategies based on realistic flow–vegetation dynamics.

The second major focus of this thesis appears in Chapter 2, where a sediment transport model is formulated based on a simplified non-hydrostatic, non-equilibrium Saint-Venant–Exner system. The model includes suspended sediment concentration, bedload transport, erosion and deposition processes, gravitational effects within the bed, and non-hydrostatic pressure. A key contribution of this chapter is the design of new well-balanced finite volume schemes that preserve steady sediment beds and minimize numerical diffusion. The proposed approach is validated against analytical and experimental data and demonstrates the capability to reproduce overtopping erosion, dam-break flows, and sediment motion under strong fluid–sediment coupling. The inclusion of non-hydrostatic pressure improves the prediction of free-surface profiles and sediment exchange rates, this confirms the relevance of vertical momentum corrections in morphodynamic simulations.

Altogether, the three studies presented in this thesis demonstrate the versatility and coherence of the proposed finite volume framework for modeling complex free-surface flows. The multi-layer non-hydrostatic formulation proves to be an efficient intermediate approach between classical depth-averaged and fully three-dimensional models, providing accurate and physically consistent results at a moderate computational cost. The sediment transport extension complements this framework by enabling the simulation of coupled hydro-morphodynamic processes while maintaining well-balancedness and numerical robustness.

The outcomes of this research contribute to a deeper understanding of tsunami–vegetation and sediment–flow interactions and emphasize the importance of vertical resolution, non-hydrostatic effects, and well-balanced numerical strategies. Beyond their mathematical implications, the models developed in this thesis serve as practical tools to assess the protective role of coastal forests and to encourage the use of native vegetation as a sustainable alternative to artificial coastal defenses such as breakwaters or seawalls. This work demonstrates how nature-based protection can improve coastal resilience, preserve local ecosystems, and maintain biodiversity. The contributions presented here lay the groundwork for future studies that seek to enhance predictive capacity and promote environmentally responsible coastal engineering practices.

4.2 Future Work

Building on the methodologies presented in this thesis, several directions for future research are identified. One avenue involves the development of a unified hydro-morphodynamic framework that couples the multilayer non-hydrostatic model with the morphodynamic Saint-Venant–Exner system to investigate tsunami-induced sediment transport and erosion in vegetated coastal zones. Numerical improvements, including the implementation of adaptive mesh refinement (AMR), implicit–explicit time integration, and high-order reconstruction techniques, also represent promising prospects. Finally, these methodologies can be applied to simulate tsunami run-up, riverbed evolution, and delta morphodynamics, thereby contributing to more accurate risk assessment and sustainable coastal management.

Conclusiones y trabajo futuro

Esta tesis doctoral contribuye al avance del modelado matemático y numérico de sistemas tipo aguas someras aplicados a flujos geofísicos. Aunque los distintos estudios abordan procesos ambientales diferentes, todos comparten un objetivo común: mejorar el realismo físico y la fiabilidad numérica de los modelos promediados en profundidad mediante la incorporación de efectos no hidrostáticos, formulaciones multicapa y esquemas de volúmenes finitos bien balanceados. Este enfoque apiunta a lograr una representación más precisa de los fenómenos del mundo real.

La primera parte de la tesis se centra en el desarrollo de un modelo no hidrostático unidimensional y multicapa para simular la propagación de tsunamis a través de vegetación costera. El modelo combina métodos de volúmenes finitos y de proyección para reproducir con precisión observaciones experimentales y proporcionar un marco robusto para el estudio de los efectos de mitigación de los bosques costeros. Mediante una formulación multicapa basada en LDNH_0, el modelo supera las limitaciones de los enfoques tradicionales que se basan en propiedades de vegetación promediadas. La inclusión de variabilidad vertical en los términos de arrastre, inercia y porosidad permite representar la influencia de la estructura de la vegetación a lo largo de la columna de agua y mejorar la precisión en la atenuación de las olas y la disipación de energía. La representación de la presión no hidrostática mediante una proyección elíptica mejora la estabilidad y la suavidad del campo de velocidades, lo que permite capturar gradientes pronunciados y características transitorias del flujo con consistencia física.

El Capítulo 3 amplía el modelo no hidrostático multicapa desarrollado en la primera parte a dos dimensiones horizontales, con el fin de ofrecer un análisis más completo de las interacciones tsunami–bosque en configuraciones realistas. El marco bidimensional revela comportamientos hidrodinámicos complejos, tales como recirculaciones verticales, flujos de retorno cercanos a la costa y redistribución lateral del flujo dentro y alrededor de la región vegetada, lo que pone de relieve el papel esencial de la resolución vertical para reproducir características de flujo similares a las tridimensionales. Los experimentos numéricos muestran que, mientras un modelo monocapa puede reproducir la propagación global, solo una formulación multicapa es capaz de capturar la estructura interna del flujo, la transferencia de energía entre capas y los mecanismos de retroalimentación que gobiernan la eficiencia de amortiguamiento de los bosques costeros. Por tanto, el modelo multicapa constituye una herramienta valiosa para analizar la función protectora de las franjas de vegetación y para mejorar las estrategias de gestión costera basadas en dinámicas realistas de interacción flujo–vegetación.

El segundo eje principal de esta investigación se presenta en el Capítulo 2, donde se formula un modelo de transporte de sedimentos basado en un sistema simplificado de Saint-Venant–Exner no hidrostático y no en equilibrio. El modelo incluye la concentración de sedimentos en suspensión, el transporte por arrastre, los procesos de erosión y deposición, los efectos gravitacionales dentro del lecho y la presión no hidrostática. Una contribución clave de este capítulo es el diseño de nuevos esquemas de volúmenes finitos bien balanceados que preservan lechos sedimentarios en equilibrio y minimizan la difusión numérica. El enfoque propuesto se valida frente a datos analíticos y experimentales, demostrando su capacidad para reproducir erosión por sobrepasamiento, flujos de rotura de presa y movimiento de sedimentos bajo un fuerte acoplamiento fluido–sedimento. La inclusión de la presión no hidrostática mejora la predicción de los perfiles de la superficie libre y las tasas de intercambio de sedimentos, lo que confirma la relevancia de las correcciones de momento vertical en las simulaciones morfodinámicas.

En conjunto, los tres estudios presentados en esta tesis demuestran la versatilidad y coherencia del marco de volúmenes finitos propuesto para el modelado de flujos con superficie libre complejos. La formulación no hidrostática multicapa se revela como un enfoque intermedio eficiente entre los modelos clásicos promediados en profundidad y los modelos tridimensionales completos, ofreciendo resultados precisos y físicamente consistentes a un costo computacional moderado. La extensión al transporte de sedimentos complementa este marco al permitir la simulación de procesos hidromorfodinámicos acoplados, manteniendo al mismo tiempo el equilibrio numérico y la robustez.

Los resultados de esta investigación contribuyen a una comprensión más profunda de las interacciones entre tsunamis, vegetación y flujo sedimentario, y destacan la importancia de la resolución vertical, los efectos no hidrostáticos y las estrategias numéricas bien compensadas. Más allá de sus implicaciones matemáticas, los modelos desarrollados en esta tesis constituyen herramientas prácticas para evaluar el papel protector de los bosques costeros y fomentar el uso de vegetación nativa como una alternativa sostenible a las defensas costeras artificiales, tales como diques o rompeolas. Este trabajo demuestra que las soluciones basadas en la naturaleza pueden aumentar la resiliencia costera, preservar los ecosistemas locales y mantener la biodiversidad. Las contribuciones presentadas sientan las bases para futuros estudios orientados a mejorar la capacidad predictiva y promover prácticas de ingeniería costera ambientalmente responsables.

4.3 Trabajos futuros

A partir de las metodologías presentadas en esta tesis, se identifican diversas líneas de investigación futura. Una de ellas consiste en el desarrollo de un marco hidromorfodinámico unificado que acople el modelo no hidrostático multicapa con el sistema morfodinámico de Saint-Venant–Exner, con el objetivo de estudiar el transporte y la erosión de sedimentos inducidos por tsunamis en zonas costeras con vegetación. Las mejoras numéricas, como la implementación de mallas adaptativas (AMR), la integración temporal implícito–explícita y las técnicas de reconstrucción de alto orden, también representan perspectivas prometedoras. Finalmente, estas metodologías pueden aplicarse a la simulación del run-up de tsunamis, la evolución de cauces fluviales y la morfodinámica de deltas, contribuyendo así a una evaluación de riesgos más precisa y a una gestión costera sostenible.

APPENDIX A

LDNH$_0$ Soliton

We assume a flat bottom (z = const.) and assume that the variables do not depend on x and t independently but rather on $\xi = x - ct$, with a constant c to be determined. Inserting this approach into (2.9) we get

$$u = c + \frac{\gamma}{h},$$

where γ is a constant that can be determined by considering a region where the wave has already passed and is now at rest. In such a region the speed u is zero, hence γ must be given by $\gamma = -ch_0$, where h_0 is the still water height. On the other hand, taking into account that

$$\partial_t(hu) = -c^2\partial_\xi h \quad \text{and} \quad \partial_x(hu^2) = c^2\partial_\xi h - \frac{\gamma^2}{h^2}\partial_\xi h = c^2\partial_\xi h + \gamma^2\partial_\xi\left(\frac{1}{h}\right),$$

we obtain

$$\partial_t(hu) + \partial_x(hu^2) = \gamma^2\partial_\xi\left(\frac{1}{h}\right),$$

hence integrating the linear momentum equation (2.9b) we obtain

$$p(z) = \frac{A}{h(\xi)} - \frac{\gamma^2}{h^2(\xi)} - \frac{gh(\xi)}{2},$$

where A is a constant of integration that can be evaluated in the same way as γ. The result is $A = gh_0\left(3h_0 + 2\eta_0\right)/2$, with η_0 the amplitude of the wave. Finally, using the constraint (2.9d) we may evaluate w:

$$w = -\frac{h}{2}\partial_x u.$$

Furthermore, assume that $h(\xi) = h_0 + \eta_0 \mathrm{sech}^2(\beta\xi)$ with a constant β to be determined. Then $h(\xi)$ satisfies

$$h' = -2\beta(h - h_0)\sqrt{1 - \frac{h - h_0}{\eta_0}}.$$

Inserting all these expressions into (2.9c) we end up with the equation

$$-\frac{2A}{h(\xi)}-\frac{2h_0^3\gamma^2\beta^2}{\eta_0 h^2(\xi)}-\frac{2h_0^2\gamma^2\beta^2}{h^2(\xi)}+\frac{3h_0^2\gamma^2\beta^2}{\eta_0 h(\xi)}+\frac{2h_0\gamma^2\beta^2}{h(\xi)}-\frac{\gamma^2\beta^2 h(\xi)}{\eta_0}+\frac{2\gamma^2}{h^2(\xi)}+gh(\xi)=0.$$

This is a cubic equation can be seen as a cubic polynomial for h where the only thing left is the value of β , solving this equation we find that

$$\beta=\sqrt{\frac{\eta_0}{h_0^2\left(h_0+\eta_0\right)}}\quad \text{and} \quad c=\sqrt{g(h_0+\eta_0)}.$$

Writing again (x,t) instead of ξ we obtain the soliton solution

$$\begin{aligned}
h(x,t) &= h_0+\eta_0 \operatorname{sech}^2\left(\beta(x-ct)\right), \\
u(x,t) &= c\left(1-\frac{h_0}{h}\right), \\
w(x,t) &= \frac{c\beta h_0 \tanh(\beta(x-ct))\left(h-h_0\right)}{h}, \\
p(x,t) &= \frac{gh_0\left(3h_0+2\eta_0\right)}{2h}-\frac{(h_0c)^2}{h^2}-\frac{gh}{2},
\end{aligned} \tag{A.1}$$

see Figure A.1. In particular, here we showed a simple way to find this soliton because we knew the functional form of $h(\xi)$ and it is easy to verify that this is solution of (2.9), but in order to find $h(\xi)$ we did use the sech method, and more complex models will require full use of it.

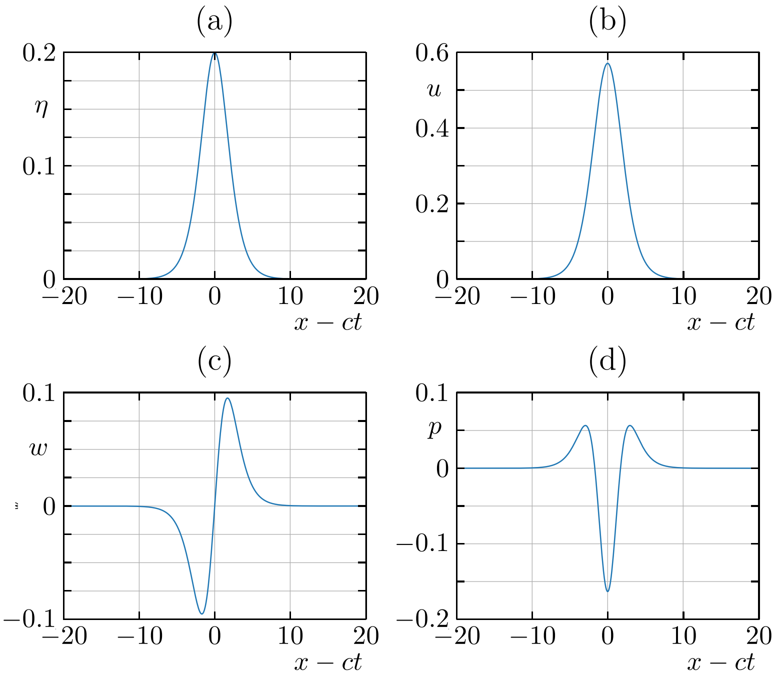

Figure A.1: Graphs of LDNH$_0$ soliton solution with $h_0 = 1$ and $\eta_0 = 0.2$.

References

[1] J. Akiyama and Y. Fukushima. Entrainment of noncohesive bed sediment into suspension. Technical Report External Memo. No. 175, Minneapolis, USA, 1985.

[2] A. Al-Ghosoun, M. Seaid, and A. S. Osman. A novel approach for modelling stress fields induced by shallow water flows on movable beds. *Applied Mathematical Modelling*, 142: 115960, 2025.

[3] K. Ashida and M. Michiue. Study on hydraulic resistance and bed-load transport rate in alluvial streams. *Proceedings of the Japan Society of Civil Engineers*, 1972(206):59–69, 1972.

[4] E. Audusse. A multilayer saint-venant model: derivation and numerical validation. *Discrete and Continuous Dynamical Systems B*, 5(2):189–214, 2005.

[5] E. Audusse and M. Bristeau. Finite-volume solvers for a multilayer saint-venant system. *International Journal of Applied Mathematics and Computer Science*, 17(3):311–320, 2007.

[6] E. Audusse, F. Bouchut, M. Bristeau, R. Klein, and B. Perthame. A fast and stable well-balanced scheme with hydrostatic reconstruction for shallow water flows. *SIAM Journal on Scientific Computing*, 25(6):2050–2065, 2004.

[7] E. Audusse, M.-O. Bristeau, and A. Decoene. Numerical simulations of 3d free surface flows by a multilayer saint-venant model. *Int. J. Numer. Methods Fluids*, 56:331–350, 2008.

[8] E. Audusse, M.-O. Bristeau, B. Perthame, and J. Sainte-Marie. A multilayer saint-venant system with mass exchanges for shallow water flows. derivation and numerical validation. *ESAIM: Mathematical Modelling and Numerical Analysis*, 45(1):169–200, 2010.

[9] E. Audusse, M.-O. Bristeau, M. Pelanti, and J. Sainte-Marie. Approximation of the hydrostatic navier–stokes system for density stratified flows by a multilayer model: kinetic interpretation and numerical solution. *J. Comput. Phys.*, 230:3453–3478, 2011.

[10] R. A. Bagnold. The flow of cohesionless grains in fluids. *Philos. Trans. Roy. Soc. London Ser. A*, 249:235–297, 1956.

[11] Y. Bai and K. F. Cheung. Depth-integrated free-surface flow with a two-layer nonhydrostatic formulation. *International Journal for Numerical Methods in Fluids*, 69(2): 411–429, 2011.

[12] F. Bouchut. *Nonlinear Stability of Finite Volume Methods for Hyperbolic Conservation Laws*. Birkhäuser Basel, 2004.

[13] S. F. Bradford and N. D. Katopodes. Hydrodynamics of turbid underflows. i: Formulation and numerical analysis. *Journal of Hydraulic Engineering*, 125(10):1006–1015, 1999.

[14] Raimund Bürger, Enrique D. Fernández-Nieto, and Jorge Moya. A multilayer shallow water model for tsunamis and coastal forest interaction. *ESAIM: Mathematical Modelling and Numerical Analysis*, 59(2):1113–1144, 2025.

[15] R. Bürger, E. D. Fernández-Nieto, and V. Osores. A dynamic multilayer shallow water model for polydisperse sedimentation. *ESAIM: Mathematical Modelling and Numerical Analysis*, 53(4):1391–1432, 2019.

[16] R. Bürger, E. D. Fernández-Nieto, and V. Osores. A multilayer shallow water approach for polydisperse sedimentation with sediment compressibility and mixture viscosity. *Journal of Scientific Computing*, 85(2), 2020.

[17] Raimund Bürger, Enrique D. Fernández-Nieto, Jose Garres-Díaz, and Jorge Moya. Well-balanced physics-based finite volume schemes for saint-venant–exner-type models of sediment transport. *Advances in Water Resources*, 206:105178, 2025. ISSN 0309-1708. doi: https://doi.org/10.1016/j.advwatres.2025.105178. URL `https://www.sciencedirect.com/science/article/pii/S0309170825002921`.

[18] Z. Cao, G. Pender, S. Wallis, and P. Carling. Computational dam-break hydraulics over erodible sediment bed. *Journal of Hydraulic Engineering*, 130(7):689–703, 2004.

[19] H. Capart and D. L. Young. Formation of a jump by the dam-break wave over a granular bed. *Journal of Fluid Mechanics*, 372:165–187, 1998.

[20] M. Castro, J. M. Gallardo, and C. Parés. High order finite volume schemes based on reconstruction of states for solving hyperbolic systems with nonconservative products. Applications to shallow-water systems. *Mathematics of Computation*, 75(255):1103–1135, 2006.

[21] M. J. Castro, A. M. Ferreiro Ferreiro, J. A. García-Rodríguez, J. M. González-Vida, J. Macías, C. Parés, and M. E. Vázquez-Cendón. The numerical treatment of wet/dry fronts in shallow flows: application to one-layer and two-layer systems. *Math. Comput. Modelling*, 42:419–439, 2005.

[22] M. J. Castro, T. Morales de Luna, and C. Parés. Well-balanced schemes and path-conservative numerical methods. In R. Abgrall and C.-W. Shu, editors, *Handbook of Numerical Analysis*, volume 18 of *Handbook of Numerical Methods for Hyperbolic Problems Applied and Modern Issues*, pages 131–175. Elsevier, 2017.

[23] F. Charru, H. Mouilleron, and O. Eiff. Erosion and deposition of particles on a bed sheared by a viscous flow. *J. Fluid Mech.*, 519:55–80, 2004.

[24] A. J. Chorin. The numerical solution of the navier-stokes equations for an incompressible fluid. *Bull. Am. Math. Soc.*, 73:928–931, 1967.

[25] A. J. Chorin. Numerical solution of the navier-stokes equations. *Math. Comput.*, 22: 745–762, 1968.

[26] A. J. Chorin and J. E. Marsden. *A Mathematical Introduction to Fluid Mechanics*. Springer, 3rd edition, 1993.

[27] V. T. Chow. *Open-Channel Hydraulics*. McGraw-Hill, New York, 1959.

[28] M. J. Castro Díaz and E. D. Fernández-Nieto. A class of computationally fast first order finite volume solvers: Pvm methods. *SIAM J. Sci. Comput.*, 34(4):A2173–A2196, 2012.

[29] C. Escalante and T. Morales de Luna. A general non-hydrostatic hyperbolic formulation for boussinesq dispersive shallow flows and its numerical approximation. *Journal of Scientific Computing*, 83(3), 2020.

[30] F. M. Exner. *Zur Physik der Dünen*. Hölder, Wien, Austria, 1920.

[31] E. Fernández-Nieto, J. Garres-Díaz, A. Mangeney, and G. Narbona-Reina. A multilayer shallow model for dry granular flows with the $\mu(i)$-rheology: Application to granular collapse on erodible beds. *J. Fluid Mech.*, 798:643–681, 2016.

[32] E. Guerrero Fernández, M. J. Castro Díaz, Y. Wei, and C. Moore. Modeling sediment movement in the shallow-water framework: A morpho-hydrodynamic approach with numerical simulations and experimental validation. *Ocean Modelling*, 192:102445, 2024.

[33] E. D. Fernández-Nieto, E. H. Koné, T. Morales de Luna, and R. Bürger. A multilayer shallow water system for polydisperse sedimentation. *Journal of Computational Physics*, 238:281–314, 2013.

[34] E. D. Fernández-Nieto, E. H. Koné, and T. Chacón Rebollo. A multilayer method for the hydrostatic navier-stokes equations: A particular weak solution. *Journal of Scientific Computing*, 60(2):408–437, 2013.

[35] E. D. Fernández-Nieto, T. Morales de Luna, G. Narbona-Reina, and J. D. Zabsonré. Formal deduction of the saint-venant–exner model including arbitrarily sloping sediment beds and associated energy. *ESAIM: Mathematical Modelling and Numerical Analysis*, 51 (1):115–145, 2017.

[36] E. D. Fernández-Nieto, M. Parisot, Y. Penel, and J. Sainte-Marie. A hierarchy of dispersive layer-averaged approximations of euler equations for free surface flows. *Communications in Mathematical Sciences*, 16(5):1169–1202, 2018.

[37] A. C. Fowler, Natalia Kopteva, and Charles Oakley. The formation of river channels. *SIAM J. Appl. Math.*, 67(4):1016–1040, 2007.

[38] M. Garcia and G. Parker. Experiments on the entrainment of sediment into suspension by a dense bottom current. *Journal of Geophysical Research: Oceans*, 98(C3):4793–4807, 1993.

[39] J. Garres-Díaz, E. D. Fernández-Nieto, A. Mangeney, and T. Morales de Luna. A weakly non-hydrostatic shallow model for dry granular flows. *Journal of Scientific Computing*, 86 (2), 2021.

[40] J. Garres-Díaz, E. D. Fernández-Nieto, and G. Narbona-Reina. A semi-implicit approach for sediment transport models with gravitational effects. *Applied Mathematics and Computation*, 421:126938, 2022.

[41] J. Garres-Díaz, C. Escalante, T. Morales de Luna, and M.J. Castro Díaz. A general vertical decomposition of euler equations: Multilayer-moment models. *Applied Numerical Mathematics*, 183:236–262, 2023. ISSN 0168-9274. doi: https://doi.org/10.1016/j.apnum.2022.09.004. URL https://www.sciencedirect.com/science/article/pii/S0168927422002288.

[42] Bobby Minola Ginting, Adel A. Mahmoud, and Tatsuhiko Uchida. New drag force model for dam-break flows through vegetation under non-hydrostatic conditions and its comparison with high-resolution, fully-resolved model. *Applied Mathematical Modelling*, 150: 116458, 2026. ISSN 0307-904X. doi: https://doi.org/10.1016/j.apm.2025.116458. URL https://www.sciencedirect.com/science/article/pii/S0307904X25005323.

[43] J. C. González-Aguirre, M. J. Castro, and T. Morales de Luna. A robust model for rapidly varying flows over movable bottom with suspended and bedload transport: Modelling and numerical approach. *Advances in Water Resources*, 140:103575, 2020.

[44] K. Guizien and E. Barthélemy. Accuracy of solitary wave generation by a piston wave maker. *J. Hydraul. Res.*, 40:321–332, 2002.

[45] A. Harten, P. D. Lax, and B. van Leer. On upstream differencing and godunov-type schemes for hyperbolic conservation laws. *SIAM Rev.*, 25(1):35–61, 1983.

[46] K. Iimura and N. Tanaka. Numerical simulation estimating effects of tree density distribution in coastal forest on tsunami mitigation. *Ocean Engrg.*, 54:223–232, 2012.

[47] A. Kurganov and G. Petrova. A second-order well-balanced positivity preserving central-upwind scheme for the saint-venant system. *Commun. Math. Sci.*, 5:133–160, 2007.

[48] R. J. LeVeque. *Finite volume methods for hyperbolic problems.* Cambridge Texts in Applied Mathematics. Cambridge University Press, 2002.

[49] X. Liu, A. Mohammadian, A. Kurganov, and J. A. Infante Sedano. Well-balanced central-upwind scheme for a fully coupled shallow water system modeling flows over erodible bed. *Journal of Computational Physics*, 300:202–218, 2015.

[50] R. Fernandez Luque and R. Van Beek. Erosion and transport of bed-load sediment. *J. Hydraul. Res.*, 14(2):127–144, 1976.

[51] S. Martínez-Aranda, J. Fernández-Pato, and P. García-Navarro. Non-equilibrium bedload transport model applied to erosive overtopping dambreach. *Water*, 15(17):3094, 2023.

[52] G. Dal Maso, P. G. Lefloch, and F. Murat. Definition and weak stability of nonconservative products. *Journal de mathématiques pures et appliquées*, 74(6):483–548, 1995.

[53] E. Meyer-Peter and R. Müller. Formulas for bed-load transport. *Rep. 2nd Meet. Int. Assoc. Hydraul. Struct. Res., Stockholm*, pages 39–64, 1948.

[54] P. Nielsen. *Coastal Bottom Boundary Layers and Sediment Transport.* World Scientific Pub Co Inc, 1992.

[55] C. Parés and M. J. Castro. On the well-balance property of roe's method for nonconservative hyperbolic systems. applications to shallow-water systems. *M2AN Math. Model. Numer. Anal.*, 38:821–852, 2004.

[56] M. Parisot. Entropy-satisfying scheme for a hierarchy of dispersive reduced models of free surface flow. *International Journal for Numerical Methods in Fluids*, 91(10):509–531, 2019.

[57] C. Parés. Numerical methods for nonconservative hyperbolic systems: a theoretical framework. *SIAM J. Numer. Anal.*, 44:300–321, 2006.

[58] Jan S. Ribberink. Mathematical modelling of one-dimensional morphological changes in rivers with non-uniform sediment. Number Report 87-2. Communic. on Hydr. and Geotech. Engrg., 1987.

[59] J. F. Richardson and W. N. Zaki. Sedimentation and fluidisation: Part i. *Chemical Engineering Research and Design*, 75:S82–S100, 1997.

[60] R. Rodríguez, P. Encina, M. Espinosa, and N. Tanaka. Field study on planted forest structures and their role in protecting communities against tsunamis: experiences along the coast of the biobío region, chile. *Landscape Ecol. Eng.*, 12:1–12, 2016.

[61] P. L. Roe. Approximate riemann solvers, parameter vectors, and difference schemes. *J. Comput. Phys.*, 43:357–372, 1981.

[62] J. Sainte-Marie. Vertically averaged models for the free surface non-hydrostatic euler system: derivation and kinetic interpretation. *Math. Models Methods Appl. Sci.*, 21:459–490, 2011.

[63] N. Shuto. The effectiveness and limit of tsunami control forests. *Coastal Engrg. Japan*, 30: 143–153, 1987.

[64] B. Spinewine and Y. Zech. Small-scale laboratory dam-break waves on movable beds. *Journal of Hydraulic Research*, 45(sup1):73–86, 2007.

[65] P. K. Stansby and J. G. Zhou. Shallow-water flow solver with non-hydrostatic pressure: 2d vertical plane problems. *International Journal for Numerical Methods in Fluids*, 28(3): 541–563, 1998.

[66] Lord Rayleigh (J. W. Strutt). On waves. *Phil. Mag. (5)*, 1:257–279, 1876.

[67] C. Escalante Sánchez, E. D. Fernández-Nieto, T. Morales de Luna, Y. Penel, and J. Sainte-Marie. Numerical simulations of a dispersive model approximating free-surface euler equations. *Journal of Scientific Computing*, 89(3), 2021.

[68] G. Tan, H. Fang, S. Dey, and W. Wu. Rui-jin zhang's research on sediment transport. *Journal of Hydraulic Engineering*, 144(6), 2018.

[69] N. Tanaka. Effectiveness and limitations of vegetation bioshield in coast for tsunami disaster mitigation. In N.-A. Mörner, editor, *The Tsunami Threat — Research and Technology*, chapter 9, pages 161–178. InTech, Rijeka, 2011.

[70] N. Tanaka, Y. Sasaki, M. I. M. Mowjood, K. B. S. N. Jinadasa, and S. Homchuen. Coastal vegetation structures and their functions in tsunami protection: Experience of the recent indian ocean tsunami. *Landscape Ecol. Eng.*, 3:33–45, 2007.

[71] R. Témam. Sur l'approximation de la solution des équations de Navier-Stokes par la méthode des pas fractionnaires (I). *Arch. Rational Mech. Anal.*, 32(2):135–153, 1969.

[72] T. Tingsanchali and C. Chinnarasri. Numerical modelling of dam failure due to flow overtopping. *Hydrological Sciences Journal*, 46(1):113–130, 2001.

[73] I. Toumi. A weak formulation of roe's approximate riemann solver. *J. Comput. Phys.*, 102 (2):360–373, 1992.

[74] G. Wei, J. T. Kirby, S. T. Grilli, and R. Subramanya. A fully nonlinear boussinesq model for surface waves. part 1. highly nonlinear unsteady waves. *Journal of Fluid Mechanics*, 294(-1):71, 1995.

[75] C. H. Wu, C.-C. Young, Q. Chen, and P. J. Lynett. Efficient nonhydrostatic modeling of surface waves from deep to shallow water. *Journal of Waterway, Port, Coastal, and Ocean Engineering*, 136(2):104–118, 2010.

[76] Y. Yamazaki, Z. Kowalik, and K. F. Cheung. Depth-integrated, non-hydrostatic model for wave breaking and run-up. *Numerical Methods in Fluids*, 61:473–497, 2008.

[77] H. Yanagisawa, S. Koshimura, K. Goto, T. Miyagi, F. Imamura, A. Ruangrassamee, and C. Tanavud. The reduction effects of mangrove forest on a tsunami based on field surveys at pakarang cape, thailand and numerical analysis. *Estuar. Coast. Shelf Sci.*, 81:27–37, 2009.